Determination of the intermolecular interactions in solutions from the motion of single molecules

Thesis by

Xuzhu Zhang

prepared under the supervision of

prof. dr hab. Robert Hołyst

within the framework of International PhD Studies at the
Institute of Physical Chemistry of the Polish Academy of Sciences
Department of Soft Condensed Matter and Fluids
Kasprzaka 44/52, 01-224 Warsaw

Warsaw, November 2017

Acknowledgements

First and foremost, I would like to express my deep gratitude to the following people who play extremely essential roles during my doctoral study:

My parents and wife, who gave me numerous support and help during my study, making me who I am today;

Prof. Robert Hołyst, who brought me into the real realm of scientific research, enlightening me with his rich scientific experience and deep wisdom;

Dr Sen Hou and **dr Lili Sun**, who helped me a lot not only in the work but also in my daily life in Poland.

I gracefully acknowledge all my co-authors who involved in this work described as follows: **prof. Andrzej Poniewierski, dr Krzysztof Sozański, dr Tomasz Kalwarczyk, dr Stefan Wieczorek, dr Aldona Jelińska, dr Anna Zagożdżon, Agnieszka Wiśniewska**.
Your contributions to my research are as much as mine.

I would also like to appreciate the other colleagues from the **Soft Matter Group** for your sincere support and great help.

Last but not least, I would like to thank all the colleagues from the Institute of Physical Chemistry Polish Academy of Sciences for making my life in Poland pleasant and joyful.

This work was supported by the National Science Centre within the two Maestro Grants 2011/02/A/ST3/00143 and 2016/22/A/ST4/00017

NATIONAL SCIENCE CENTRE POLAND

Part of this work was inspired by ERA CHAIR grant No 666295 from European Union's Horizon 2020 research and innovation programme.

The equipments used in this thesis were funded by the NanoFun laboratories POIG.02.02.00-00-025/09.

nanofun

List of publications

Publications directly related to the Thesis

1. X. Zhang, A. Poniewierski, S. Hou, K. Sozański, A. Wiśniewska, S.A. Wieczorek, T. Kalwarczyk, L. Sun, R. Hołyst, *Tracking structural transitions of bovine serum albumin in surfactant solutions by fluorescence correlation spectroscopy and fluorescence lifetime analysis*, **Soft Matter**: 2015, 11, 2512-2518.

2. X. Zhang, A. Poniewierski, A. Jelińska, A. Zagożdżon, A. Wiśniewska, S. Hou, R. Hołyst, *Determination of equilibrium and rate constants for complex formation by fluorescence correlation spectroscopy supplemented by dynamic light scattering and Taylor dispersion analysis*, **Soft Matter**: 2016, 12, 8186-8194.

3. R. Hołyst, A. Poniewierski, X. Zhang, *Analytical form of the autocorrelation function for the fluorescence correlation spectroscopy*, **Soft Matter**: 2017, 13, 1267-1275.

4. K. Sozański, E. Sisamakis, X. Zhang, R. Hołyst, *Quantitative fluorescence correlation spectroscopy in three-dimensional systems under stimulated emission depletion conditions*, **Optica**: 2017, 4, 982-988.

5. X. Zhang, E. Sisamakis, K. Sozański, R. Hołyst, *Nanoscopic approach to quantification of equilibrium and Rate constants of complex formation at single-molecule level*, **Journal of Physical Chemistry Letters** : 2017, 8, 5785-5791.

Other publications

6. S. Hou, M. Tabaka,; L.Sun, P.Trochimczyk, T. S. Kaminski, T. Kalwarczyk, X. Zhang, R. Hołyst, *A flexible fluorescence correlation spectroscopy based*

method for quantification of the DNA double labeling efficiency with precision control, **Laser Physics Letters**: 2014, 11, 085602.

7. S. Hou, P. Trochimczyk, L. Sun, A. Wiśniewska, T. Kalwarczyk, X. Zhang, B. Wielgus-Kutrowska, A. Bzowska, R. Hołyst, *How can macromolecular crowding inhibit biological reactions? The enhanced formation of DNA nanoparticles*, **Scientific Reports**: 2016, 6, 22033.

8. L. Sun, M. Tabaka, S. Hou, K. Burdzy, A. Aksimentiev, C. Maffeo, X. Zhang, R. Hołyst, *The Hinge Region Strengthens the Nonspecific Interaction between Lac-Repressor and DNA: A Computer Simulation Study*, **PloS One**: 2016, 11.

9. X. Zhang, F. Du, J. Huang, W. Lu, S. Liu, J. Jia, *Fabrication of biodegradable micelles with reduction-triggered release of 6-mercaptopurine profile based on disulfide-linked graft copolymer conjugate*, **Colloids and Surfaces B: Biointerfaces**: 2012, 100, 155-162.

10. Y. Xue, X. Tang, J. Huang, X. Zhang, J. Yu, Y. Zhang, S. Gui, *Anti-tumor efficacy of polymer-platinum(II) complex micelles fabricated from folate conjugated PEG-graft-alpha, beta-poly [(N-amino acidyl)-aspartamide] and cis-dichlorodiammine platinum(II) in tumor-bearing mice*, **Colloids and Surfaces B: Biointerfaces**: 2011, 85, 280-288

Patents

11. J. Yu, X. Zhang, Q. Guo, Q. Wu, P. Luo, J. Huang, *Fabrication of biodegradable micelles with reduction-triggered release of 6-mercaptopurine profile based on disulfide-linked graft copolymer conjugate*, **201110200449.9**

12. J. Yu, Q. Wu, X. Zhang, J. Zeng, F. Du, J. Huang, *Poly (ethylene glycol) shell-sheddable nanomicelle prodrug of camptothecin with enhanced cellular uptake*, **201210003860.1**

Thesis

Intermolecular interactions in solution appear in all types of biochemical reactions and can be quantified by equilibrium and rate constants of the reactions. Due to the presence of intermolecular interactions, the free motion of each molecule taking part in the reaction is influenced to some extent depending on these constants. Within this thesis, I proposed a convenient and reliable method for the qualitative and quantitative determination of intermolecular interactions in solutions from the motion of single molecule.

Fluorescence correlation spectroscopy (FCS), one type of single-molecule technique, was employed as the main method in this thesis. FCS monitors the motion of fluorescent probes in various solutions where different types of intermolecular interaction take place. By analysing the motion of probes using proper theoretical models for FCS, I quantitatively determined the intermolecular interactions in complexes formed by the probes with other substances in terms of equilibrium and rate constants.

The validity and reliability of my method has been proved by several examples of intermolecular interactions in this thesis, such as protein-surfactant interaction (chapter 2), dye-micelle interaction (chapter 3) and drug-DNA interaction (chap-

ter 4). The thesis paves a promising application of FCS toward the quantitative determination of intermolecular interactions in chemical and biological systems.

Contents

List of symbols and abbreviations

D	diffusion coefficient
D_0	self-diffusion coefficient
D_c	cooperative diffusion coefficient
D_+	effective diffusion coefficient
J	diffusion flux
T	absolute temperature
R_h	hydrodynamic radius
Q	quantum yields
C	concentration
N_A	Avogadro constant
n	index of refraction
p	fraction of molecules in the triplet state
q	wave vector
k_+	association rate constant
k_-	disssociation rate constant
k_dc	diffusion-controlled association rate constant
k_NR	rate constant of nonradiative process
k_R	rate constant of radiative process
k_B	Boltzmann's constant
η	dynamic viscosity
θ	scattering angle
V_eff	volume of Gaussian detection spheroid (in FCS)
L	waist radius of focal volume in x-y plane (in FCS)

H	long radius of focal volume along the beam direction (in FCS)
u	average velocity of the flow in capillary
σ	dispersion coefficien
τ	lag time
τ_{fl}	excited state lifetime
τ_{t}	triplet state lifetime
t	time
l	capillary length
R_{c}	radius of the capillary (in TDA)
ρ	density of the carrier phase (in TDA)
γ	viscosity of the carrier phase (in TDA)
K	equilibrium constant
r_{c}	radius of curvature of the coiled capillary (in TDA)
N_{ag}	mean aggregation number
R	chemical relaxation rate
ΔG	free-energy difference
P_{STED}	STED power
P_{SAT}	saturation power of a fluorophore
β	fraction of complexes
N	average number of molecules in FV
κ	structure parameter of fcoal volume (in FCS)
λ	laser wavelength
Rh110	rhodanime 110
LambertW	LambertW function (in TDA)
$G(\tau)$, ACF	autocorrelation function
BSA	bovine serum albumin
$C_{12}E_5$	pentaethylene glycol monododecyl ether
$C_{12}E_8$	octaethylene glycol monododecyl ether
CMC	critical micelle concentration
CTAC	cetyltrimethylammonium chloride
DNA	deoxyribonucleic acid

DOX	doxorubicin
FCS	fluorescence correlation spectroscopy
FV	focal volume
MSD	mean square displacement
SDS	sodium dodecyl sulfate
SSE	Stokes-Sutherland-Einstein equation
STED	stimulated emission depletion
TCSPC	time-correlated single photon counting
TDA	taylor dispersion analysis
NA	numerical aperture

Abstract

Intermolecular interactions occur when molecules are approaching or contacting each other. The types and strengths of the interaction depend on the chemical and physical properties of individual molecules. Before the advent of single-molecule techniques in 90s, experiments aiming at the study of the intermolecular interactions were usually performed on an ensemble of molecules in bulk. As a result, behaviours of individual molecule in the processes of interaction could not be fully distinguished, and only average characteristics were measured.

In this thesis I aim to quantitatively determine the intermolecular interactions from the motion of fluorescent probes in aqueous solutions at single-molecule level, which were not available from the ensemble experiments in the past. Single-molecule technique fluorescence correlation spectroscopy (FCS) and stimulated emission depletion-FCS (STED-FCS), as well as other auxiliary methods such as dynamic lighting scattering (DLS), Taylor dispersion analysis (TDA), etc., were employed in this work. The diffusion coefficients of probes, equilibrium and rate constants for the complex-formation were determined from the analysis of experimental data using proper theoretical models.

The thesis is composed of five chapters. Chapter 1 gives a comprehensive introduction of the studies, provides related background knowledges of the experimental techniques utilized in this thesis: FCS, STED-FCS, DLS, TDA, etc. Chapter 2 elucidates the influences of various surfactants on the structure of globular protein (bovine serum albumin, BSA) due to the intermolecular interactions. Chapter 3 probes the diffusion-reaction dynamics of complex-formation in a model

system of dye-micelle, where I retrieve the equilibrium and rates constants. Chapter 4 presents the quantitative determination of the interaction between anticancer drugs (Doxorubicin) and DNA *in vitro* based on the methods derived from the former chapters. In the end, Chapter 5 gives a brief overview of all the studies and final conclusions.

Chapter 1

Introduction

1.1 Types of Intermolecular Interactions

Interaction usually occurs when two or more objects are approaching each other. In chemistry intermolecular interaction, also known as noncovalent interactions or molecular interactions, refers to the mutual effects between two or even more molecules. The concept was first proposed by J. D. van der Waals (1873) in explaining the properties of real gases and liquids [1]. In contrast to the intramolecular interactions (e.g., covalent bond), (inter)molecular interactions are usually much weaker in terms of bond energy (see Fig. 1.1). However they play critical roles in determining the physicochemical properties of matters, for example, maintaining the three-dimensional structures of lipids, proteins, DNA, etc.

Generally intermolecular interactions are catalogued into two main groups:

- Specific interaction—involving in the formation of well-defined complexes with exact stoichiometry, for example, macromolecule-ligand complexes (e.g., protein-drug and protein-DNA complexes) [2].

- Non-specific interaction—affecting the formation of complexes without stoichiometry or creating loosely-bound aggregates. It usually consists of four major subcategories [3, 4]:

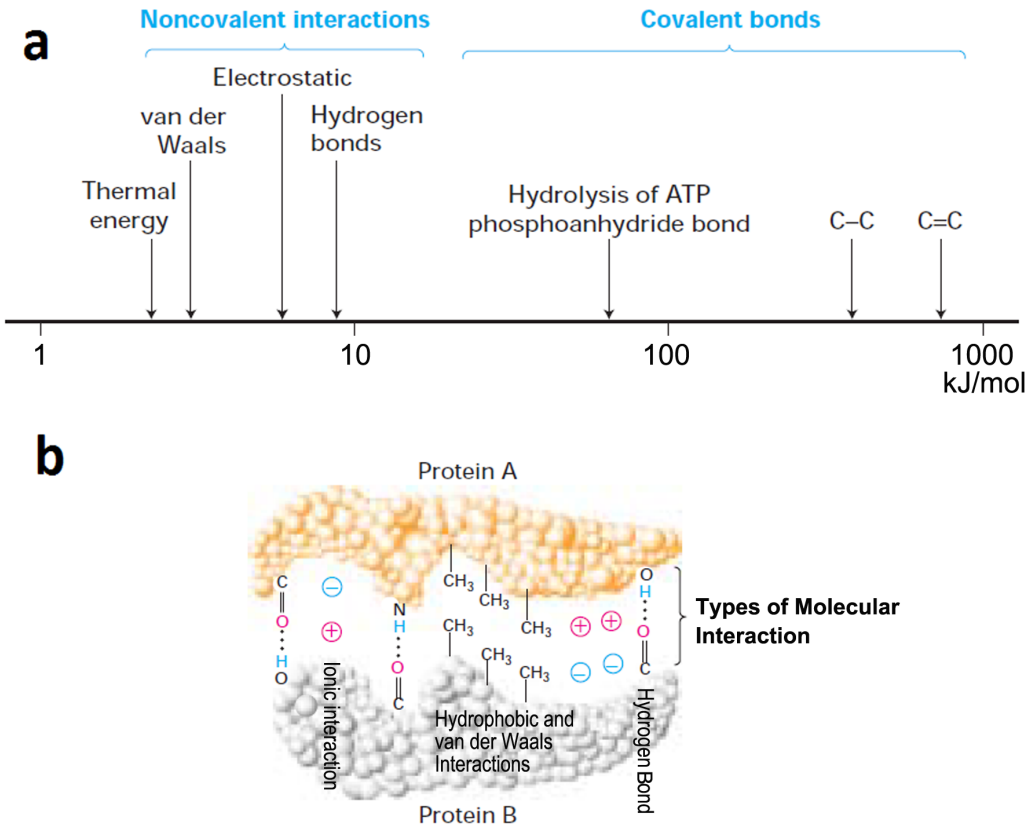

Figure 1.1: (a) Comparison of the energies required to break covalent bonds and noncovalent interactions. Apparently covalent bonds are one to two orders of magnitudes stronger than the noncovalent interactions; (b) Exemplified covalent bonds and noncovalent interactions in two proteins. In addition to the covalent bonds that connect the atoms of amino acids together, noncovalent interactions stabilize the structure of protein.

1. Ionic interaction;
2. Van der Waals forces (Keesom force, Debye force, and London dispersion force);
3. Hydrogen bonding;
4. Hydrophobic effect.

Ionic Interaction

Ionic interaction, governed by the Coulomb's law, results from the attractive and repulsive forces among ions or molecules possessing permanent charges once they

are close enough in space. Unlike covalent bonds, the electrostatic interaction does not have fixed or specific geometric orientations since the electrostatic field around an ion is isotropic.

The relative strength of the interaction between two ions, A^+ and B^- for example, partially depends on the concentration of other ions in the solution (Debye screening). The higher the concentrations of other ions (e.g., Na^+ and Cl^-), the more opportunities for A^+ and B^- have to interact ionically with these other ions, and thus the lower the energy required to break the interaction between them. Therefore, increasing the concentration of salt in the solution weakens the electrostatic interactions among the two ions due to the Debye screening.

Van der Waals Interaction

In contrast to ionic interaction which exists between the particles with permanent charges, van der Waals interaction occurs between molecular dipoles, either transiently induced or permanent electric ones (Fig. 1.2) [5]. Generally van der Waals interaction includes:

- Dipole–dipole interaction, alternatively called the Keesom force, is the electrostatic interaction between permanent dipoles in the molecules which contain electronegative atoms such as oxygen, nitrogen, sulfur, and fluorine;

- Dipole–induced dipole interaction, also called Debye force, denotes the interaction between a permanent dipole and another non-polar molecule with an induced dipole;

- Induced dipole–induced dipole interaction, known as London dispersion force, exits in all molecules even those without permanent dipoles. It originates from the temporary fluctuations of electron density of molecules or atoms when the two dipoles are almost simultaneously induced. It is the weakest one among all noncovalent interactions.

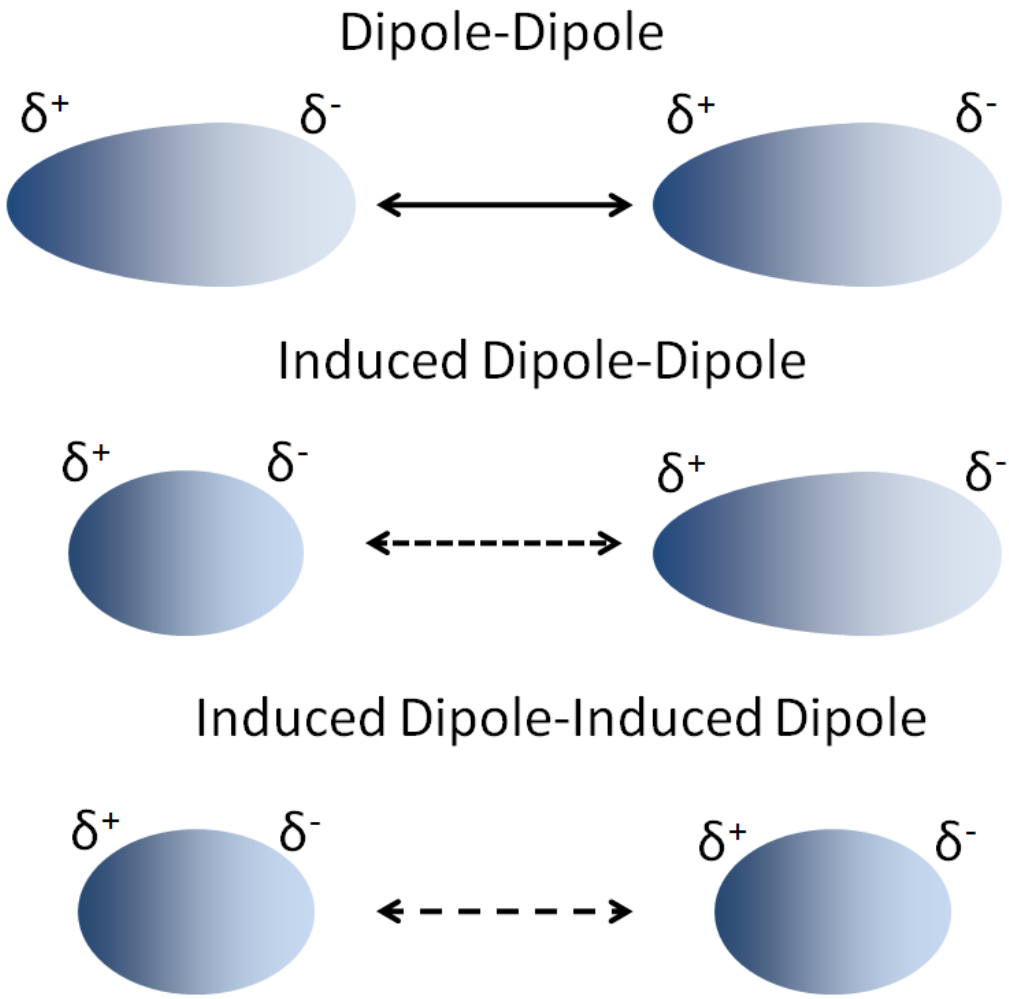

Figure 1.2: Schematic illustration of van der Waals inteaction.

The strength of van der Waals interaction decreases rapidly as the distance between atoms increases. However, if atoms get too close, they begin to repel each other because of the negative-charged electrons. When the attraction between two atoms exactly balances the repulsion from their electron clouds, the atoms are in van der Waals contact.

Hydrogen Bonding

Hydrogen bond is a special dipole-dipole interaction between a partially positive-charged hydrogen atom in a molecular dipole and another highly electronegative atom (e.g. oxygen, nitrogen, sulphur, or fluorine). When a hydrogen atom (H)

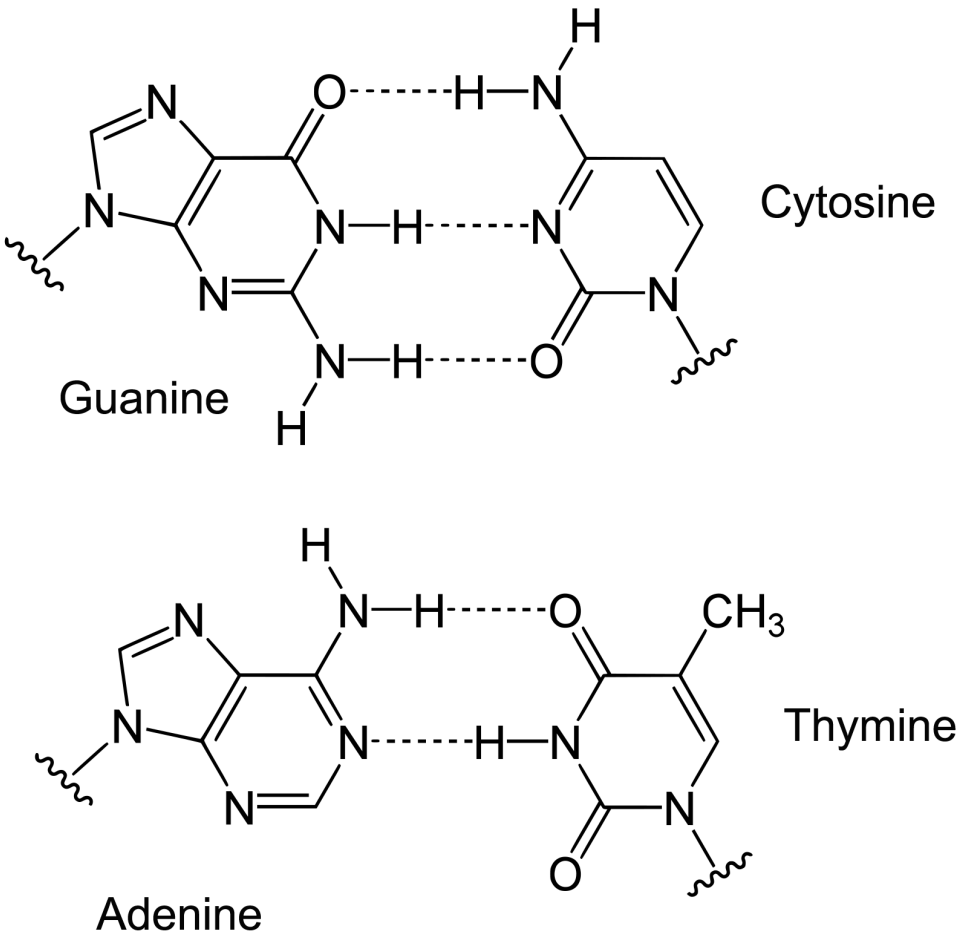

Figure 1.3: Hydrogen bonding in the base pairs of DNA. Adenine and thymine form two hydrogen bonds, while guanine and cytosine are linked by three bonds.

covalently bound to an electronegative donor atom (D), it can form another extra bond, i.e., hydrogen bond, with an acceptor atom (A) possessing lone pair of electrons as:

$$D^{\delta-} - H^{\delta+} + A^{\delta-} \rightleftarrows D^{\delta-} - H^{\delta+} \cdots A^{\delta-}$$

The superscript represents the partial charge of each atom.

Although the hydrogen bond is longer and weaker than the covalent bond between the same atoms, it plays an important role in maintaining the physiochemical properties of matters. The simplest example of hydrogen bond exists in water. It provides water with many special properties, such as high melting and boiling points. Hydrogen bonding is also crucial in stabilizing the three-

dimensional structures of proteins and double helices of DNA molecules (see Fig. 1.3) [6].

Generally the interactions above belong to the electrostatic interactions originating from charges or dipoles, while the hydrophobic effect in the following subsection depends on the thermodynamic properties of matter.

Hydrophobic Effect

Hydrophobic effect denotes the phenomenon of aggregation of nonpolar molecules or nonpolar portions of molecules for reducing the extent of their contact with water molecules. For example, the formation of micelles results from the self-assembly of surfactant molecules in water. Less water molecules are needed to surround the nonpolar surfactant molecules after the self-assembly, which is much more entropically favourable than the unaggregated state (see Fig. 1.4). In other words, the hydrophobic effect stabilize the nonpolar molecules in aqueous solution energetically. Hydrophobic effect is commonly observed in a diversity of biological phenomenons. Protein folding is one typical example of hydrophobic effect [7, 8].

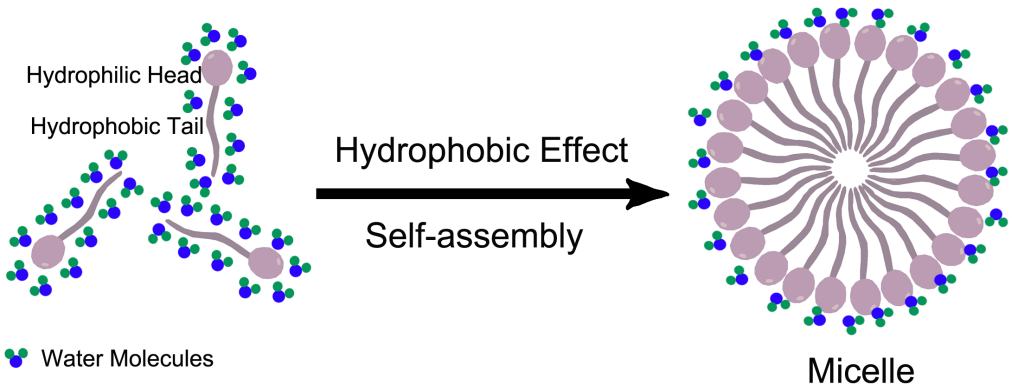

Figure 1.4: Schematic illustration of micelles formation due to the hydrophobic effect: self-assembly of surfactant molecules consisting of hydrophilic heads and hydrophobic tails reduces the total number of water molecules required to surround them separately. It is an entropic and energetically favourable state compared with the non-aggregated state.

1.2 Molecular Motion in Liquids

All molecules are in constant motion driven by their kinetic energy. The degree of freedom of molecular motion depends on the phase of matters (i.e., gas, liquid or solid state). The motion of molecules in liquids can be generally catalogued into two main groups: a) rotational motion without changing the position of centre of mass but the orientation of molecular axis in space; b) translational movement of a centre of mass with fixed orientation of molecule [9]. Any molecular motion is the combination of both of them.

Brownian Motion and Diffusion

Brownian motion is the random motion of particles suspended in a fluid due to the collision with other atoms or molecules. The motion was first discovered by a botanist Robert Brown in 1827 while he was studying the pollen grains suspended in water under a microscope [10]. Brown observed that the particles ejected by the pollen grains were conducting random movement. However, he was not able to explain the mechanisms behind this phenomena since the concept of "atoms and molecules" had not been a well-documented concept at that time.

The mechanism behind Brownian motion was proposed by other scientists at the beginning of the XXth century. Among them, the explanations from Albert Einstein and Marian Smoluchowski gained the most intensive attentions in the field of physics. Einstein described the Brownian motion using a diffusion equation for the Brownian particles, in which the diffusion coefficient of the particle (D) was related to its mean square displacement (MSD) [11]:

$$MSD =< (r(t) - r(0))^2 >= nDt, \tag{1.1}$$

where n is a dimensionality parameter equal to 2, 4, or 6 for 1-, 2-, or 3-dimensional diffusion, respectively, and $r(t)$ denots the position of a particle at time t. Smolu-

chowski's derivation of Brownian motion started from the same premise as that of Einstein and got the same expression for *MSD* [12].

Fick's Laws

Scientific study of diffusion can be traced back to the experiments performed by Thomas Graham around 1830s [13,14]. On the basis of Graham's research, Adolf Fick proposed his laws of diffusion in 1855 [15], which are known as Fick's Laws. He treated diffusion as the migration of matter down a concentration gradient by analogy to the flow of heat and electric current which were actual migration of heat and charges down a temperature and electrical potential gradient respectively.

Fick's first law, relating the diffusive flux to the concentration gradient (∇C), is given by:

$$\boldsymbol{J} = -D\nabla C, \tag{1.2}$$

where J is the number of molecules going through a unit area in a unit time and D is the diffusion coefficient.

Fick's second law predicts how diffusion causes the concentration (C) change as a function of time t, which is expressed as:

$$\frac{\partial C}{\partial t} = D\nabla^2 C. \tag{1.3}$$

Stokes-Sutherland-Einstein (SSE) Equation

Sutherland, Smoluchowski and Einstein independently revealed the temperature-dependence of diffusion rates in their theoretical papers on "Stokes" particles in Brownian motion at the beginning of XX century [11,16,17]. The general form of the equation, currently called Stokes-Sutherland-Einstein (SSE), is given as [18]:

$$D_0 = \mu k_{\mathrm{B}} T, \tag{1.4}$$

where D_0 is the self-diffusion coefficient of the "Stokes" particle, k_{B} is the Boltzmann's constant, T is the absolute temperature and μ is the ratio of the particle's

velocity ν to the applied drag force F_{d}. For spherical particle with radius R_{h}:

$$F_{\mathrm{d}} = 6\pi\eta R_{\mathrm{h}}\nu, \tag{1.5}$$

where η is the dynamic viscosity of the medium. To combine the two equation above, we obtain the final SSE equation as:

$$D_0 = \frac{k_{\mathrm{B}}T}{6\pi\eta R_{\mathrm{h}}}. \tag{1.6}$$

SSE equation reveals the relation between diffusion coefficient of a particle and its hydrodynamic radius in a fluid. Deviations from SSE equation were observed when very small probe were used [19]. Additionally, breakdown of the SSE equation in complex liquids were also reported. Validity of the SSE equation is retained if the viscosity of medium is not treated as a constant, but as a function of probe size [20]. Then the effective viscosity in Eq. 1.5 is experimentally determined.

1.3 The Phenomena of Fluorescence

Fluorescence, one type of luminescence, is the spontaneous emission of light from excited substance [21]. The story of fluorescence started with a report by N. Monardes in 1565. However, the major experimental and theoretical aspects of fluorescence were really understood only after the emergence of quantum theory in the twentieth century (i.e., 1918-1935). Numerous observations and achievements related to fluorescence, Jablonski's diagram for example [22], were published during this period in succession [23].

The Perrin-Jablonski Diagram

The Perrin-Jablonski diagram, named after French physicist Francis Perrin and Polish physicist Aleksander Jablonski, is a useful tool for visualizing the possible processes involved in fluorescence, including photons absorption, internal conversion, fluorescence emission, etc (see Fig 1.5). When a molecule (or a particle)

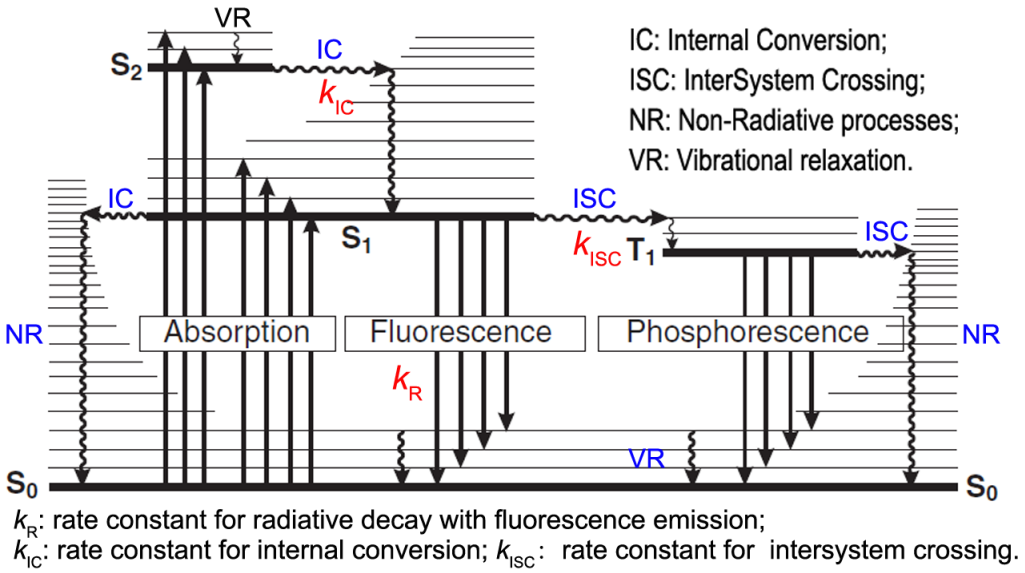

Figure 1.5: Simplified Perrin-Jablonski diagram [23]. S_0, S_1, S_2 correspond to singlet ground, first and second excited states of the molecule. T_1 represents first excited triplet state.

interacts with a photon whose energy equals to the difference between ground and excited state of the molecule, electrons may absorb the energy of photon and then jump to an excited state (e.g., $S_0 \rightarrow S_1$ or S_2). Because the excited state is far from thermodynamic equilibrium, the molecule tends to return to the ground state from the first excited singlet state ($S_1 \rightarrow S_0$) via nonradiative and radiative decay. During the nonradiative, decay energy is released as heat to the surroundings if differences between the energy levels are small. In the radiative processes the emitted photons are observed as fluorescence. If the emission process occurs in the absence of an external stimulus/magnetic field, it is called spontaneous emission. If the emission takes place in the presence of external stimuli, for example external electromagnetic field, then it is called stimulated emission. In the stimulated emission the energy transferred to the electromagnetic field creates new photons with the same phase, frequency, polarization, and direction of travel as the photons of the incident wave. Therefore, stimulated emission can be applied to many fields, such as the amplification of laser and stimulated emission depletion

(STED) microscopy, because of its unique properties.

If the geometry of an excited molecule in a vibrational state of the singlet state is identical to that of the molecule in the triplet state, intersystem crossing may occur. Then photons emitted from the transition between $T_1 \rightarrow S_0$ are observed as phosphorescence.

Fluorescence Lifetime

Generally fluorescence lifetime denotes the time of a fluorophore spending in the excited state. The excitation of a fluorescent sample by an infinitely sharp pulse of light leads to a certain number of molecules to the excited state. The return of the excited molecules to the ground state via radiatively and nonradiatively decay, or intersystem crossing. In chemical kinetics, the rate of deactivation of excited molecules can be expressed by the following differential equation [21, 23]:

$$\frac{dN(t)}{dt} = (k_{\mathrm{R}} + k_{\mathrm{NR}})N(t), \tag{1.7}$$

where $N(t)$ is the number of excited molecules at time t after excitation. k_{R} and k_{NR} are the rate constants for radiative and nonradiative processes respectively. And,

$$k_{\mathrm{NR}} = k_{\mathrm{IC}} + k_{\mathrm{ISC}}, \tag{1.8}$$

where k_{IC} is the rate constant of internal conversion ($S_1 \rightarrow S_0$) without fluorescence emission, k_{ISC} is the rate constant of intersystem crossing ($T_1 \rightarrow S_0$). Integration of Eq. 1.7 yields

$$N(t) = N_0 \exp(-t/\tau_{\mathrm{fl}}), \tag{1.9}$$

where τ_{fl} is the fluorescence lifetime and is defined as

$$\tau_{\mathrm{fl}} = 1/(k_{\mathrm{R}} + k_{\mathrm{NR}}). \tag{1.10}$$

In fluorescence experiments we actually measure the fluorescence intensity $I(t)$ rather than the number of excited molecules, since I(t) is proportional to $N(t)$.

Then we can rewrite Eq. 1.9 as

$$I(t) = I_0 \exp(-t/\tau_{\text{fl}}). \tag{1.11}$$

The average fluorescence lifetime of a fluorophore can be determined from the fitting of experimental data with Eq. 1.9. For organic molecules, it ranges from tens of picoseconds to hundreds of nanoseconds. By contrast, phosphorescence lifetime usually last from microseconds to hours – much longer than that of fluorescence lifetime.

Additionally, the fluorescence lifetime is one of the most important characteristics of a fluorophore because it defines the time window for the observation of dynamic phenomena of the molecule [23]. It is a relatively long process compared to the time-scale of various molecular events. The fluorophore may undergo a variety of transformations during this time, such as electron redistribution, geometric alteration to reorganization of the surrounding molecules and chemical reactions [24]. As a result, the value of fluorescence lifetime varies in different situations and environments.

Quantum Yields

Quantum yield Q is defined as the ratio of the number of emitted photons from fluorophores (P_{em}) to the number of absorbed photons (P_{ab}) over the whole duration of the decay. In other words, it is the fraction of excited molecules that return to the ground state with the emission of fluorescence photons [23]:

$$Q = \frac{P_{\text{em}}}{P_{\text{ab}}} = \frac{k_{\text{R}}}{k_{\text{R}} + k_{\text{NR}}}. \tag{1.12}$$

Apparently both quantum yield and fluorescence lifetime depend on the rate constants k_{R} and k_{NR}. A molecule may be nonfluorescent because of a large rate constant of nonradiative decay or a slow rate constant of radiative process. Substances with large quantum yields, rhodamine family for example, usually have excellent fluorescent properties (i.e., shine brightly after excitation)

1.4 Experimental Techniques

This section introduces the working principle and theoretical background of experimental techniques we employed in the studies of intermolecular interactions. Introduction to fluorescence correlation spectroscopy (subsection 1.3.1), stimulated emission depletion fluorescence correlation spectroscopy (subsection 1.3.2), dynamic light scattering (subsection 1.3.3), and Taylor dispersion analysis (subsection 1.3.4) are included respectively.

Fluorescence Correlation Spectroscopy (FCS)

Fluorescence correlation spectroscopy (FCS) was first introduced by Magde, Elson and Webb in the early 1970s for the determination of the chemical kinetics of the intermolecular interaction between DNA and ethidium bromide [25–27]. Since the advent of confocal microscopy illumination, FCS retrieved a renaissance in the 1990s [28–30]. In FCS, fluctuations of fluorescence emitted from probes diffusing through a focal volume are recorded. Autocorrelation of the signal reveals the characteristic time scales of the fluctuations. Combined with a proper theoretical model, such analysis may offer various information on the physiochemical properties of the probes, such as diffusion coefficients, concentrations, structures, singlet-triplet lifetime, dynamics of any reaction they are involved in, etc [8, 31]. In the following paragraph more details are provided.

FCS Setup In FCS experiments we record the fluctuation of fluorescent signals resulting from the motion of fluorescent molecules within a focal volume (FV) created by a confocal microscopy and laser source. Coupled with the microscopy, a single-photon-counting detector is indispensable for the detection of photons emitted from fluorescent molecules. Generally, the essential components of the FCS setup are:

- Laser line for exciting probes (in constant wave or pulsed model);

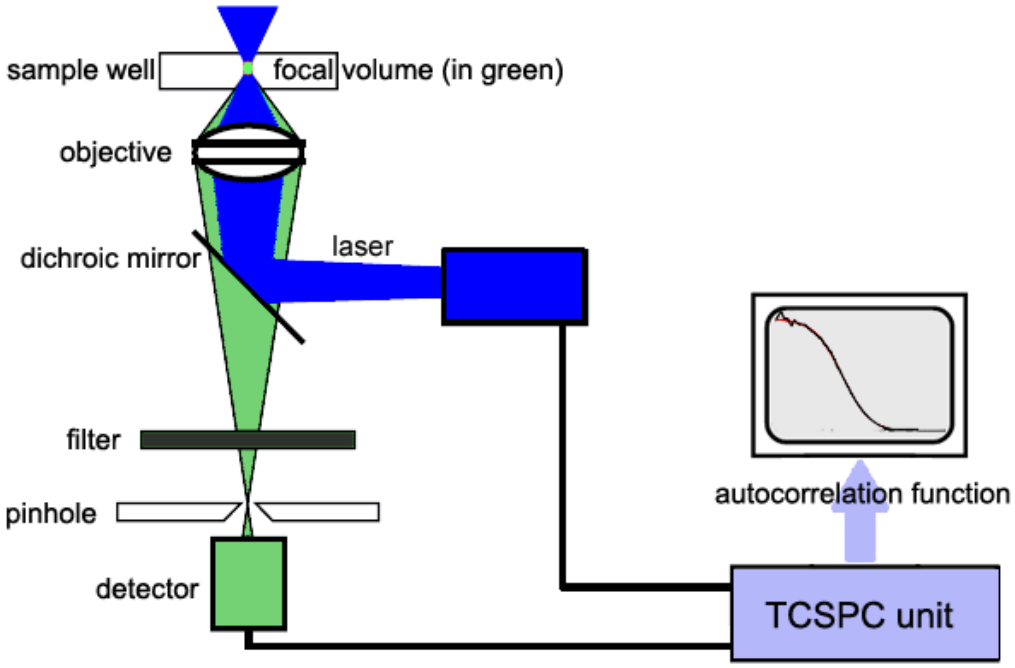

Figure 1.6: Simplified scheme of the FCS setup. The light from a laser source passes through a water immersion microscope objective to excite probes within a focal volume (FV). The emitted fluorescence signals are collected by the detector and further fed to TCSPC unit. Autocorrelation analysis of the signals reveals the characteristic time-scales of the fluctuations, e.g., residence time of the probes inside the focal volume.

- Single-photon sensitive detectors;
- Dichroic mirror for separating fluorescence signal from excitation light;
- Objective with high *NA* (numerical aperture) to reduce aberration and increase the yields of photons;
- Temperature controller;
- Acquisition and analysis software.

A simplified scheme of a typical FCS setup is presented in Fig. 1.6. A laser beam passing through a water immersion microscope objective create an illuminated spot called focal volume (FV) or observation volume in the sample solution. Emitted fluorescent signals from the excited probes in the FV are collected by the objective and then pass through the pinhole via dichroic mirrors and filters. With

the help of pinhole, we can minimize the volume of FV to 0.2 fL at least. Filters remove the background light at given wavelength range and cut the residual excitation light. After pinhole, signals are fed to detectors and time-correlated single photon counting (TSCPC) unit. The latter records the number of detected photons in each detection event and then stores it in a histogram which represents the form of the decay [21].

Theory of FCS FCS is a technique based on the analysis of the fluctuations in the fluorescent signals. It can be quantified mathematically in terms of autocorrelation function (ACF). ACF exhibits the self-similarity of a signal as a function of lag time τ, which provides the characteristic time of undergoing processes. According to the definition, ACF is simply written as [32]:

$$G(\tau) = \frac{< \delta I(t)\delta I(t+\tau) >}{< I(t) >^2}, \tag{1.13}$$

where $\delta I(t)$ is the deviation of fluorescence intensity at time t from the mean value:

$$\delta I(t) = I(t) - < I(t) > . \tag{1.14}$$

Analysis of $G(\tau)$ provides information on the residence time of probes inside the FV. Once we know the geometry of FV, the diffusional properties of probes can be obtained. The profile of FV is described by a three-dimensional Gaussian distribution of fluorescent intensity as [21]:

$$F(\mathbf{r}) = I_0 \exp[\frac{-2(x^2+y^2)}{L^2} - \frac{2z^2}{H^2}], \tag{1.15}$$

where $F(\mathbf{r})$ is fluorescent intensity at any position $\boldsymbol{r}$ within the Gaussian profile, L and H are the radii of Gaussian profile in the x-y plane and z direction (see Fig. 1.7). The Gaussian function does not have sharp boundaries, thus the values of L and H only represent the distances from the ellipsoidal centre to the position where the intensity $F(\mathbf{r})$ reduced to the $1/e^2$ of the maximum value I_0 at the x-y plane and z direction respectively.

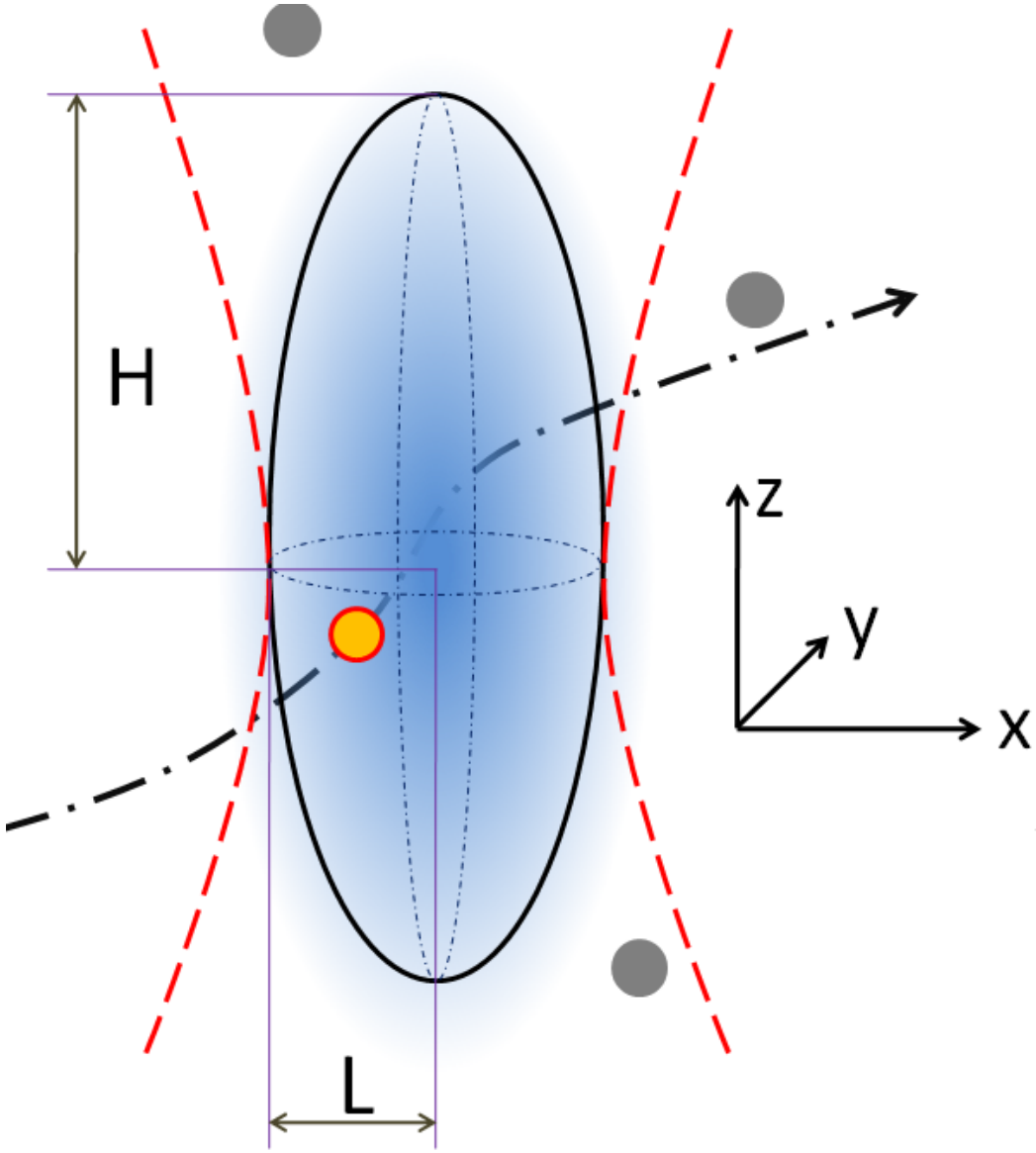

Figure 1.7: The profile of FV in FCS setup: an elongated ellipsoid within which the intensity distribution of light follows 3D Gaussian function. L and H are the radii of the ellipsoid in x-y plane and z direction respectively. The fluctuations of fluorescent intensity due to the Gaussian distribution of light intensity and the motion of the probes in the FV.

Assuming the fluorescence property of a probe does not change during the observation time, we obtain ACF for the free diffusion of single component in three-dimensional space (3D):

$$G_{3D}(\tau) = \frac{1}{CV_{\text{eff}}} \frac{1}{(1+\frac{\tau}{\tau_1})} \frac{1}{\sqrt{(1+\frac{\tau}{\kappa^2\tau_1})}}, \tag{1.16}$$

where V_{eff}, representing the effective volume of FV, is defined as

$$V_{\text{eff}} = \frac{(\int F(\mathbf{r})dV)^2}{\int F^2(\mathbf{r})dV} = \pi^{3/2}L^2H \tag{1.17}$$

And κ, the structure parameter, is equal to the ratio of the long radius H to the short radius L of the FV:

$$\kappa = H/L. \tag{1.18}$$

The average residence time of a probe in the FV, τ_1, is related to the its self-diffusion coefficient D_0 in form of :

$$\tau_1 = L^2/4D_0. \tag{1.19}$$

In the case of $\tau = 0$, we can extract the average number of molecules (N) in the FV from amplitude of ACF:

$$G(0) = \frac{1}{CV_{\text{eff}}} = \frac{1}{N}. \tag{1.20}$$

In some special situation, cell membranes for example, the diffusion of probes is confined in the x-y plane of FV. Therefore, it is necessary to use the 2D model of ACF ($\kappa = 0$) to analyse the diffusion of probes. Then Eq. 1.16 is simplified into [32]:

$$G_{2\text{D}}(\tau) = \frac{1}{CV_{\text{eff}}}\frac{1}{(1+\frac{\tau}{\tau_1})}. \tag{1.21}$$

Another important phenomena we may encounter in FCS experiments is the changes in the fluorescent properties of probes while they are diffusing in the FV. Instead of recalculating the ACF for this issue, an extra term $G_X(\tau)$ is added to Eq. 1.13 if the fluorescence fluctuations originated from these changes are much faster than those resulted from the diffusion of probes on time-scales [32]:

$$G_{\text{total}}(\tau) = G_{3D}(\tau) \cdot G_{\text{X}}(\tau). \tag{1.22}$$

One of the most common changes of the fluorescent properties arises from the singlet to triplet state transition ($S_1 \rightarrow T_1$, see Fig. 1.5). During this transition

probes do not emit any photons and hence stay dark. The transition is described by a simple exponential decay $G_{\mathrm{t}}(\tau)$:

$$G_{\mathrm{t}}(\tau) = 1 + \frac{p}{1-p}\exp(\frac{-\tau}{\tau_{\mathrm{t}}}), \tag{1.23}$$

where p is the average fraction of probes in the triplet state and τ_{t} is the lifetime of triplet state (ranging from nanoseconds to microseconds). Compared to the typical residence time of a probe in FV (usually dozens of microseconds), this "flickering" time is very short. Hence, combining Eq. 1.16 and 1.23 to Eq. 1.22 we rewrite the ACF with the triplet state transition included for probes freely diffusing in 3D into a more general form:

$$G_{\mathrm{total}}(\tau) = \frac{1}{N}\left(1 + \frac{p}{1-p}\exp\left(\frac{-\tau}{\tau_{\mathrm{t}}}\right)\right)\left(\frac{1}{CV_{\mathrm{eff}}}\frac{1}{\left(1+\frac{\tau}{\tau_1}\right)}\frac{1}{\sqrt{\left(1+\frac{\tau}{\kappa^2\tau_1}\right)}}\right). \tag{1.24}$$

For the case of multi-component diffusion with different mobility, Eq. 1.16 is modified when all kinds of motions are taking into account:

$$G_{\mathrm{m}}(\tau) = \frac{1}{N}\sum_i \frac{A_{\mathrm{i}}}{(1+\frac{\tau}{\tau_{\mathrm{i}}})\sqrt{(1+\frac{\tau}{\kappa^2\tau_{\mathrm{i}}})}}, \tag{1.25}$$

where index i refers to the i-th component and A_i denotes its fraction. However, this formula consists of too many free parameters. It is advised to conduct other independent measurements, such as dynamic light scattering or taylor dispersion analysis, to fix the values of some free parameters in Eq. 1.25. Then more accurate fitting results will be obtained.

STimulated Emission Depletion-FCS (STED-FCS)

Due to the diffraction limit, the length-scale of FV in FCS can not be reduced below $\sim$ 200 nm. Stimulated emission depletion (STED) nanoscopy, one of the super-resolution techniques which emerged in recent years, breaks the diffraction

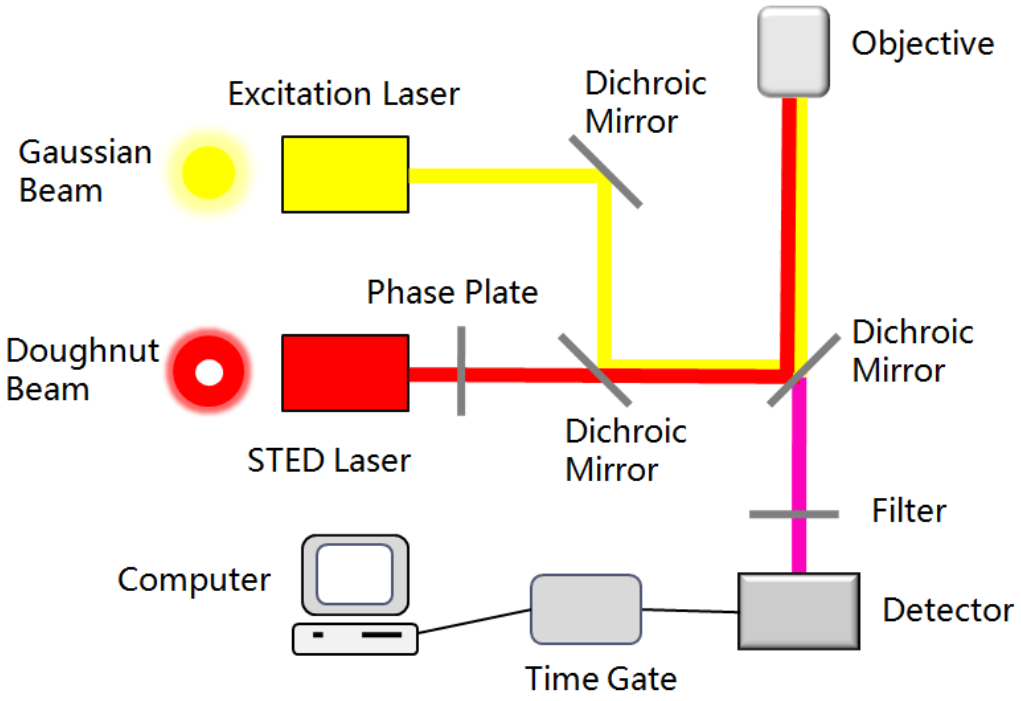

Figure 1.8: Schematic illustration of STED-FCS setup. Excitation (Gaussian distribution) and STED laser beams (doughnut shape) are combined by dichroic mirrors to form a subdiffraction-size spot, leaving only probes in the center capable of visible fluorescence. Fluorescence signals (magenta) are detected by the single-photon-counting detector, whose detection events are time-gated with respect to the excitation pulses and then registered by a computer. The size of the FV can be dynamically controlled by adjusting the power of STED beam.

limitation and offers a spatial resolution down to $\sim$ 20 nm by employing a depleting laser beam (doughnut shape with zero-intensity at centre) coaxial to the excitation beam [33–35]. In principle the depleting laser beam trims the observation volume to sub-diffraction size by inhibiting the spontaneous emission of probes with the stimulated emission (Fig. 1.8). Combination of STED with FCS (STED-FCS) provides much more detailed information on the intermolecular interaction at sub-diffraction scale [36]. A number of such studies have been reported in the 2D systems (e.g., membrane lipids) [37–41]. However, few related works in the aqueous solutions of chemical substances have been reported using STED-FCS due to the lack of the analytical form of autocorrelation function (ACF) for its 3D observation volume [42–44].

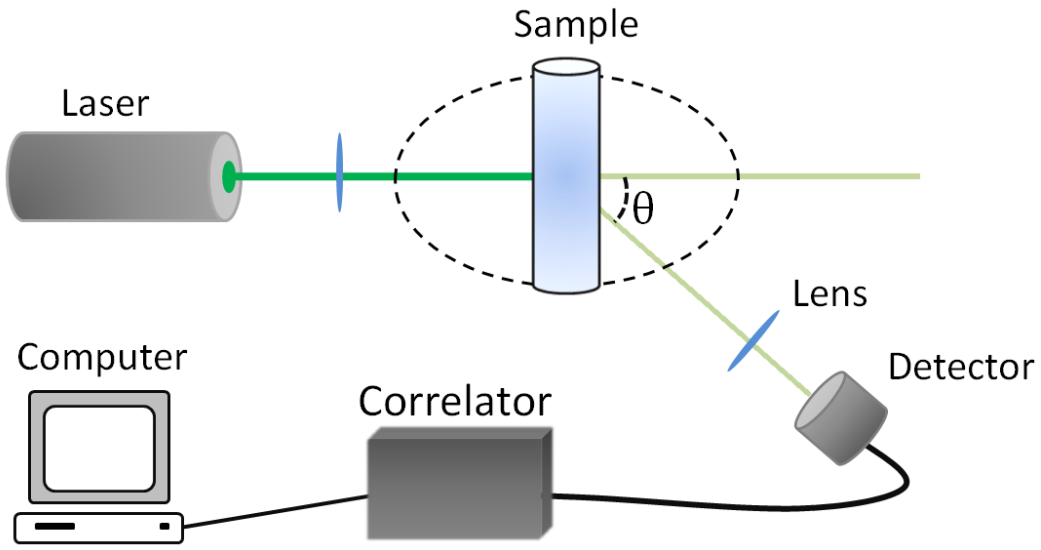

Figure 1.9: Simplified scheme of DLS setup. The fluctuations in the intensity of scattered light due to the Brownian motion of particles are collected by the detector. Information on the time scale of movement of the particles can be obtained from the analysis of the fluctuations using ACF. θ is the scattering angle, which can be adjusted by a goniometer in experiments.

Dynamic Light Scattering (DLS)

Dynamic light scattering, also called photon correlation spectroscopy or quasi-elastic light scattering [45], is a technique for the determination of diffusion coefficients, sizes and size distribution of small particles in solutions [46]. Similar to the mathematical principle of FCS, DLS also relies on the autocorrelation analysis of signals fluctuation. Differing with FCS, DLS records the scattered light signals directly from the particles undergoing Brownian motion. Fluorescent labelling of the interested particle is not necessary in DLS experiments. Therefore, on one hand DLS can be much more widely applied to various systems compared to FCS; On the other hand, DLS lacks of high sensitivity and precise selectivity of targeted signals from a complicated system since all the particles scatter light. To some extent, the two techniques, DLS and FCS, can complement each other in the study of diffusion.

Generally a typical DLS setup consists of a continuous wave laser line, photon

detector and the software for data analysis (see Fig. 1.9). When an incident light hits small particles undergoing Brownian motion in a solution, the light will be absorbed or scattered in any directions. Due to the constant movements of the particles, constructive or destructive interference among the scattered light occurs. These cause the fluctuations of the light intensity [47]. Similar to FCS, the mobility of particles can be derived from the fluctuations of intensity using ACF:

$$g(q,\tau) =< i(q,t)i(q,t+\tau) > . \tag{1.26}$$

where i is the scattered intensity at given time t and $t+\tau$ at given wave vector q. The wave vector is a quantity depending on the experimental setup:

$$q = \frac{4\pi n}{\lambda} \sin(\frac{\theta}{2}), \tag{1.27}$$

where λ is the wavelength of the incident beam, n is the refraction index of the solution, and θ is the angle at which the detector is located with respect to the incident beam (see Fig. 1.9).

For dilute suspension of the monodispersed particles in Brownian motion, $g(q,\tau)$ is a single-exponential function:

$$g(q,\tau) = B + A\left(\exp\left(-\tau/\tau_{\mathrm{c}}\right)\right)^2, \tag{1.28}$$

where B is the baseline of the function, A is the coherence factor which is regarded as a fitting parameter in the data analysis.

From the obtained decay time τ_{c} we can determine the cooperative diffusion coefficient via:

$$\frac{1}{\tau_c} = D_{\mathrm{c}} q^2. \tag{1.29}$$

The self-diffusion coefficient of particles at infinite dilution ($C_{\mathrm{p}} \to 0$), D_0, can be determined via the relation [48]:

$$D_{\mathrm{c}} = D_0(1 + \alpha C_{\mathrm{p}}), \tag{1.30}$$

where α is a constant. The cooperative diffusion coefficient depends on the particle concentration due to the presence of mutual interactions between solvent molecules

and particles (attraction or repulsion). The hydrodynamic radius of the particle, R_{h}, can be determined by D_0 using SSE equation (see Eq. 1.6).

Taylor Dispersion Analysis (TDA)

G. Taylor proposed a mathematical model for describing the dispersion process of substances in a laminar flow confined in a long, straight capillary in 1953 [49]. Due to the concentration gradient between the central part and walls of the capillary after injection, the substances diffuse in radial direction. The concentration distribution of these substances at the end of the capillary is given by the Gaussian distribution. The normalized form of the function is given by:

$$P(t) = \frac{1}{2\sqrt{\pi\sigma t}} \exp\left(-\frac{(l-ut)^2}{4\sigma t}\right), \tag{1.31}$$

where σ is the dispersion coefficient, t is time, l is the capillary length, and u is the average velocity of the flow in the capillary.

In TDA experiments we determine the diffusion coefficient of substances (D_{st}) in a laminar flow from the measured dispersion coefficient in the straight capillary, according to the Taylor theory [50, 51]:

$$\sigma = \frac{u^2 R_{\mathrm{c}}^2}{48 D_{\mathrm{st}}}, \tag{1.32}$$

where R_{c} is the radius of the capillary.

In practice it is advised to use a coiled capillary instead of the straight one whose length is usually at least 15 m. The coiled capillary has following advantages:

- less space occupation;
- better temperature control;
- shorter data acquisition time;
- longer durability.

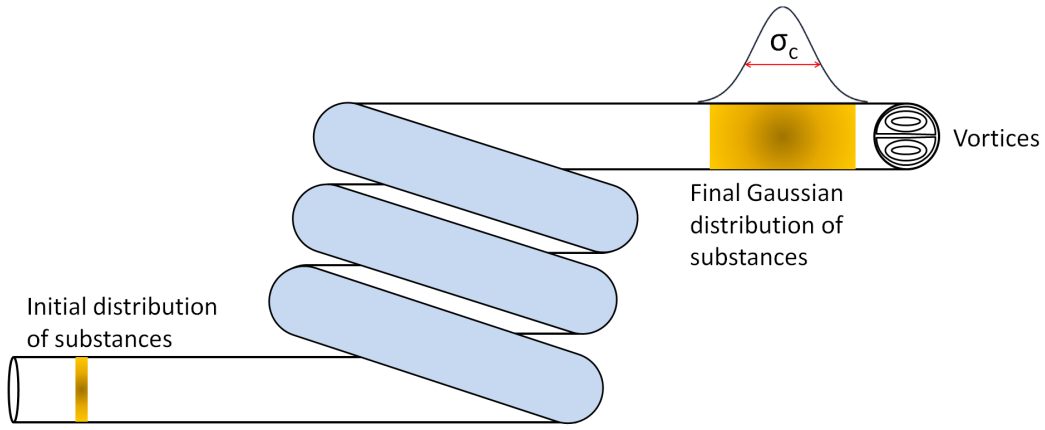

Figure 1.10: Dispersion of substances in a coiled capillary. The concentration distribution of interested substances displays a Gaussian profile at the end of the capillary. The dispersion coefficient, σ_c, is determined from the full width at half maximum of the Gaussian function. Vortices appear in the coiled capillary because of the curve path of flow.

However, centrifugal force is generated due to the curved path of the flow in a coiled capillary, which is negligible in the case of straight capillary. The centrifugal force generates local vortices, and then narrows the distribution of substances in the capillary (see Fig. 1.10). In this case, the equation relating to the dispersion and diffusion coefficient of substances is modified [50]:

$$D_{\text{coil}} = -\frac{1}{48}\frac{u^2 R_{\text{c}}^2}{\sigma_{\text{c}} \cdot A \cdot LambertW\left(-1, -\frac{1}{192}\frac{r_{\text{c}}\gamma \exp\left(-B/A\right)}{R_{\text{c}}\rho\sigma_{\text{c}}A}\right)}, \tag{1.33}$$

where ρ is the density of the carrier phase, γ is the viscosity of the carrier phase, r_{c} is the radius of curvature of the coiled capillary, and σ_{c} is the dispersion coefficient in a coiled capillary. $LambertW$ is the LambertW function, which can be approximated by the relation:

$$LambertW(-1, x) \approx W(x) = l_1 - l_2 + \frac{l_2}{l_1} + \frac{l_2(-2 + l_2)}{2l_1^2}, \tag{1.34}$$

where $l_1 = \ln(-x)$ and $l_2 = \ln\left(-\ln\left(-x\right)\right)$.

Another important application of TDA is the determination of equilibrium constant for complex-formation [52]. Taking the formation of ligand-macromolecule complex for example, we need to determine the diffusion coefficients of ligand (D_{l})

and macromolecule (D_{m}) in aqueous solutions using Eq. 1.33 separately. Then to measure the effective diffusion coefficient of the ligand in macromolecule solution (D_{+}) using the same method, the equilibrium constant K is obtained from the established relation [52, 53]:

$$KC_{\mathrm{m}} = \frac{D_{+} - D_{\mathrm{l}}}{D_{\mathrm{m}} - D_{+}}, \tag{1.35}$$

where C_{m} is the concentration of macromolecules.

Chapter 2

Protein/Surfactant Interactions

Structural dynamics of proteins plays essential roles in their biological functions and are of great interests in the fields of biochemistry and biophysics. However, it is still difficult to monitor it precisely and conveniently using convention methods [54]. In this chapter, we investigated the structural transition of protein bovine serum albumin (BSA) in low concentrated cationic (cetyltrimethylammonium chloride, CTAC), anionic (sodium dodecyl sulfate, SDS), and nonionic (pentaethylene glycol monododecyl ether, $C_{12}E_5$ and octaethylene glycol monododecyl ether, $C_{12}E_8$) surfactant solutions by FCS and fluorescence lifetime analysis at a single-molecular level. We observed different structures of BSA and lifetimes of the dye ATTO-488 labelled to BSA in these surfactant solution. What's more, we revealed the principal factor that caused the structural transitions of BSA in these solutions.

2.1 Experimental Section

Materials and Methods

Cationic surfactant CTAC (purity: 99%) and anionic surfactant SDS (purity: 99.9%) were purchased from TCI and Roth, respectively. Nonionic surfactants

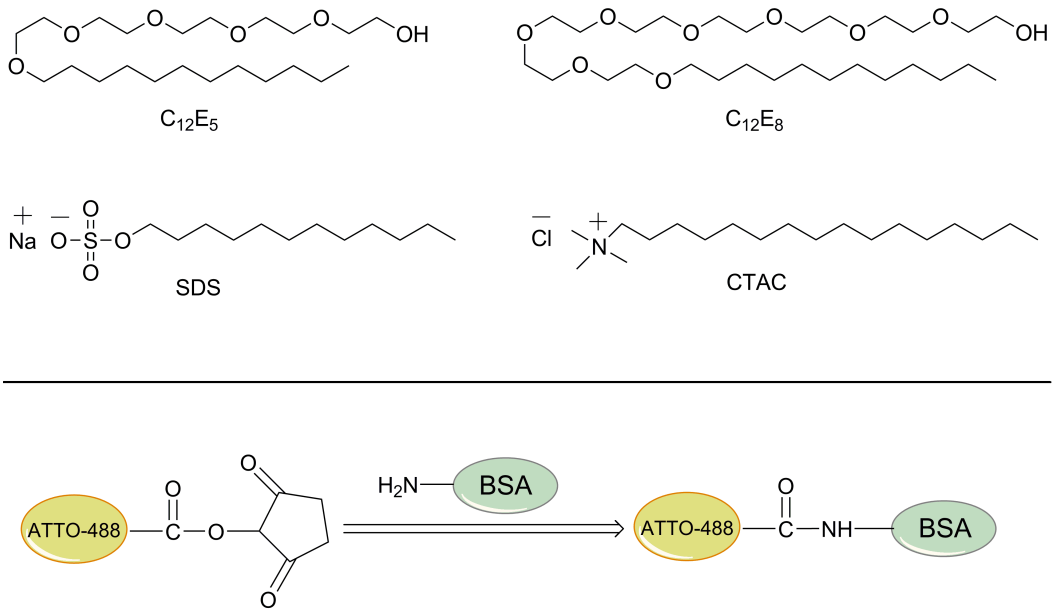

Figure 2.1: Upper panel: chemical structures of used surfactants. Lower panel: scheme for labelling protein BSA with fluorescence dye ATTO-488.

$C_{12}E_5$ (purity: 99%) and $C_{12}E_8$ (purity: 99%) were purchased from Fluka. The chemical structures of the surfactants see the upper panel of Fig. 2.1. Fluorescence dyes rhodamine 110, BSA and ATTO-488 protein label kit were purchased from Sigma-Aldrich.

Labelling BSA with ATTO NHS-Ester Firstly, we dissolved 1 mg of BSA in 1 M of labeling buffer (mixture of PBS buffer and 0.2 M sodium bicarbonate solution, pH 8.3). Then we dissolved 1.0 mg of ATTO-488 NHS-ester in 50 μl of anhydrous, amine-free DMSO. Next, we added a three-fold molar excess of the ATTO-488 solution to the protein solution with gentle shaking. We incubated the reaction mixture protected from light for up to 1 hour at the room temperature. Finally, we separated the ATTO-BSA conjugate from the free dye by a gel filtration column. We assumed that ATTO-488 was such a small molecule that the physical and chemical properties of BSA were not affected by labelling.

The FCS setup used in our experiments was a commercial inverted NIKON EZ-C1 confocal microscope. The focal setup was additionally equipped with Pi-

coHarp 200 made by PicoQuant GmbH and a 488 nm Argon-Ion laser for illumination. A water immersion objective with a numerical aperture (NA) equals 1.2 and magnification of 60 was used in FCS measurements. Before each measurement a drop of filtered, de-ionized water was used as the immersion medium between the sample in the cover-glass and objective. During measurements the laser power was set at a constant level and the focal volume was at a constant distance of 10 μm from the edge of the cover-glass. An avalanche photo diode was used for detection. BSA labelled with ATTO-488 at concentration of $\sim 10^{-9}$ M was added to all surfactant solutions. 200 μl of the solution was transported into the sample container (8 chambered Coverglass-Lab-Tek®) and further analyzed by FCS. Each measurement (duration 60 s) was repeated at least ten times at 25 ℃. The obtained autocorrelation function curves were analyzed by SymPhoTime and Gnuplot program.

Fluorescence lifetime of ATTO-BSA in surfactant solutions was measured with the same laser line but in pulsed model at 25 ℃. The values of fluorescence lifetime were acquired from the fits of the fluorescence decay curves using the mono-exponential model (Eq. 1.11).

2.2 Results and Discussion

Diffusional and Structural Properties of BSA

We measured the diffusion of ATTO-BSA at various concentrations of $C_{12}E_5$ (CMC = 0.06 mM or 0.0024%) and $C_{12}E_8$ (CMC = 0.09 mM or 0.0048%) [55]. We did not observe any noticeable changes in the residence time of BSA in the FV in these solutions (Fig. 2.2 (A) and (B)). The residence time of BSA in these solutions fitted by Eq. 1.24 was around 0.16 ms (see Fig. 2.2 (E)), which was roughly the same as in pure water. Therefore the structure of BSA was stable in the nonionic surfactant solutions [56]. Our previous work on the mobility of

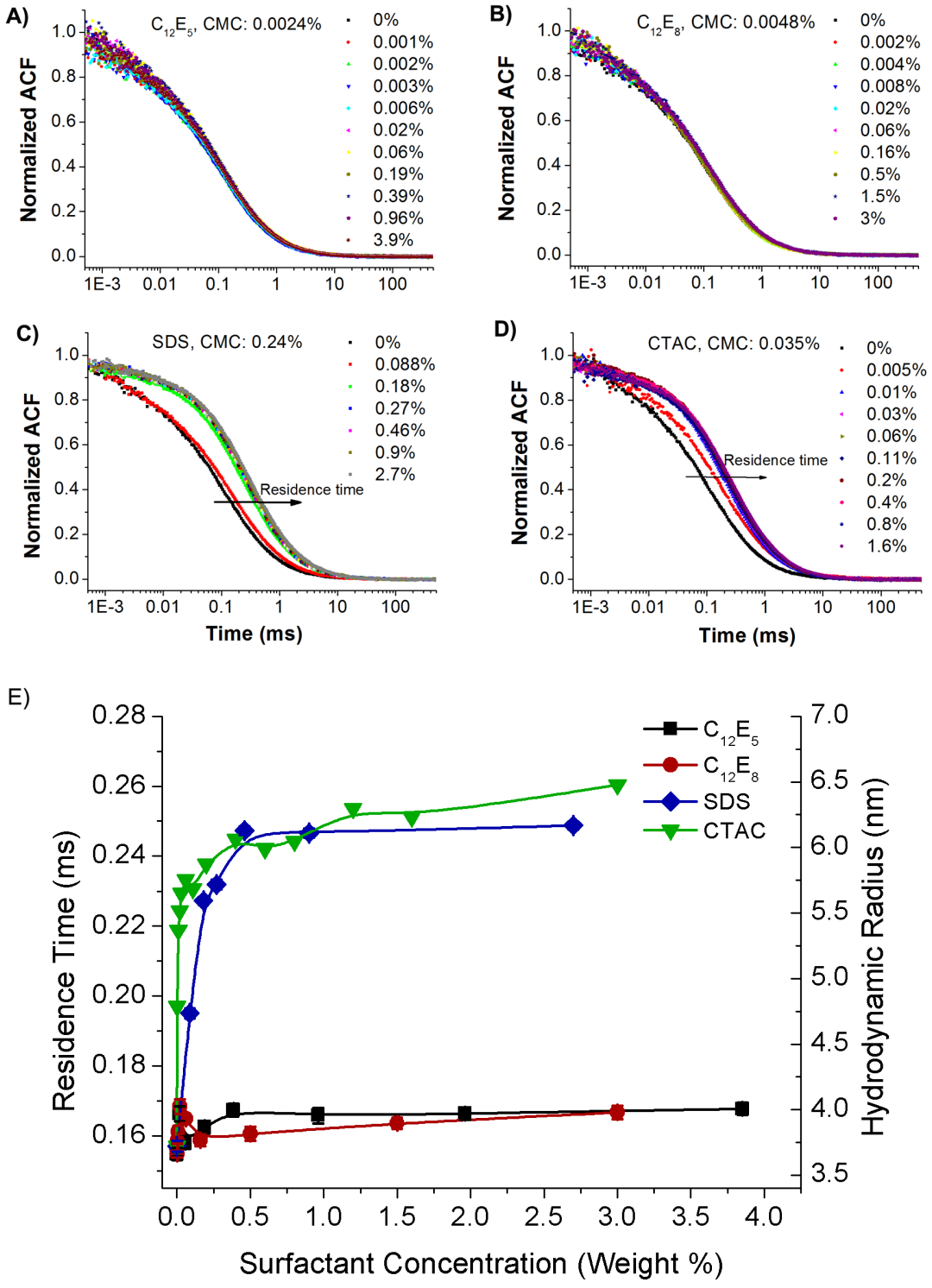

Figure 2.2: (A-D) Normalized experimental autocorrelation function curves of ATTO-BSA diffusing in the solutions of $C_{12}E_5$, $C_{12}E_8$, SDS and CTAC, respectively. The overlapped sets of data points in (A) and (B) indicated that the residence time of BSA in the $C_{12}E_5$ and $C_{12}E_8$ solutions did not depend on the surfactant concentration. In (C) and (D), sudden increases in the residence time were found in both the SDS or CTAC solutions at concentrations below the CMC. (E) Residence times and hydrodynamic radii of BSA in four surfactant solutions as a function of concentration. The residence times and hydrodynamic radii of the ATTO-BSA in $C_{12}E_5$ or $C_{12}E_8$ solutions were roughly the same as in pure water, whereas sudden transitions were observed in the ionic surfactant solutions. Structure of BSA underwent apparent changes in the ionic surfactant solutions. Error bars were smaller than the symbols.

lysozyme protein in the hexaethylene glycol monododecyl ether ($C_{12}E_6$) solutions was also consistent with the present result. The diffusion coefficient of lysozyme did not change in the $C_{12}E_6$ solutions within the same range of surfactant concentration [57].

In the case of BSA diffusing in highly diluted solutions of SDS, we observed an abrupt increase in the residence time (Fig.2.2 (C)). The transition took place at the concentration of 0.088% SDS, which is three times below CMC (0.24% at 25 ℃) [58]. A slight increase in the SDS concentration (to 0.18%) led to a sudden jump of the residence time. The jump indicated that the structure of BSA underwent a significant change in this concentration range. As it increased up to 0.46%, the residence time of BSA approached a constant value.

This result is in line with the classic "necklace-bead" model which attributes the structural change of the protein to the protein-surfactant interactions and binding. The model features: (I) specific binding, where only a small amount of surfactant molecules binds to the specific high-energy sites of the protein without changing its structure; (II) non-cooperative binding; (III) cooperative binding, where unfolding of protein is believed to start, and (IV) saturation, suggesting that further binding of surfactant does not occur on the protein [59]. We observed that when the concentration of SDS was below 0.088%, the interaction between BSA and SDS belonged to the region (I): only a small amount of SDS molecules bound to the specific high-energy site of the protein without causing its structural change. The region of saturation (above 0.18%, below CMC) was clearly seen in Fig. 2.2 (C) and was very close to the earlier report from the dynamic light scattering (DLS) measurements with the result of 0.21% [60]. Nevertheless, the regions (II) and (III) where the protein began to unfold, from 0.088% to 0.18% in our case, was too narrow to be distinguished. A similar trend was also observed in the BSA-CTAC system (Fig. 2.2 (D)). The structural transition of BSA took place at the concentration of 0.005% CTAC in solution, which was seven times smaller than the CMC (0. 035% or 1.1 mM, 25 ℃) [61]. BSA became saturated

with CTAC once the concentration of CTAC increased to 0.02% (still below its CMC).

Nonionic surfactants ($C_{12}E_5$ and $C_{12}E_8$) bound to BSA through hydrophobic interactions and hydrogen bonds, however, these interactions were too weak to change the structure of BSA [62]. Instead, they prevented the protein from aggregation [58, 63]. By contrast, the electrostatic interactions between the ionic surfactants and BSA were much stronger than the hydrophobic interactions, leading to the significantly structural changes of BSA. Therefore, the electrostatic interaction seemed to be the most significant driving force that led the structural changes of BSA [64].

Zirwer *et al* proposed an empirical equation: $R_{\mathrm{h}} = (2.8 \pm 0.3)\ N_{\mathrm{a}}^{0.5\pm0.02}$ Å, to predict the hydrodynamic radius of a highly unfolded protein, where N_{a} denoted the number of amino acid residues in a single polypeptide chain [65]. The calculated hydrodynamic radius of unfolded BSA ($N_{\mathrm{a}} = 583$) was 6.8 ± 0.7 nm according to the empirical equation. Using the diffusion coefficient of rhodamine 110 ($D_{\mathrm{rh110}} = 4.7 \pm 0.4 \times 10^{-10}\ \mathrm{m^2 s^{-1}}$) for calibration, we calculated the hydrodynamic radius of BSA in surfactant solutions via Eq. 1.6. The calculated hydrodynamic radius of BSA after the structural transition was 6.2 nm (Fig. 2.2(E)), close to the calculated value using the empirical equation and the published result of 6.0 nm by DLS [60]. The calculated radius of BSA-CTAC complex was 6.5 nm, slightly bigger than that of BSA-SDS complex.

In some cases the increase of hydrodynamic radius resulted from the self-aggregation of proteins. However, it happened only when the protein concentration was high enough [66]. In our experiment, we did not observe such a phenomenon because of the extremely low concentration of BSA in surfactant solutions (in the nanomole range). We compared the average numbers of BSA molecules, N, staying in the FV in each BSA-surfactant system from the fits of autocorrelation curves using Eq. 1.24. The value of N did not change as the increase of surfactant concentration (Fig. 2.3), proving the non-aggregation be-

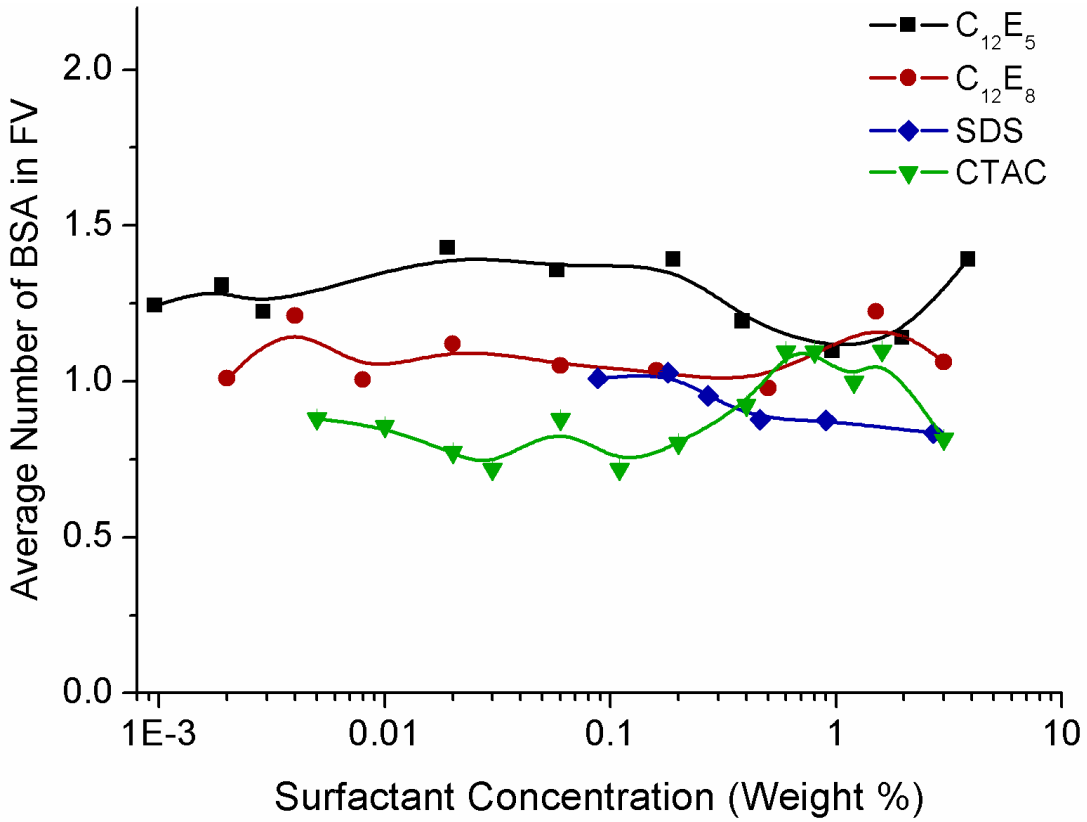

Figure 2.3: The average numbers of ATTO-BSA (N) in the FV in $C_{12}E_5$, $C_{12}E_8$, SDS and CTAC solutions as a function of surfactant concentrations. Error bars are smaller than the symbols.

haviour of BSA in these solutions. Slight fluctuations of N in each system might result from the high sensitivity of FCS technique, which required the probe concentration in the nanomole range only. Riekkola group also proved that BSA did not aggregate in the presence of SDS [64].

There is still no consensus on the causes of structural transition of proteins in surfactant solutions [67]. Based on the experimental results of SDS and CTAC, we concluded that BSA experienced a sudden structural transition in ionic surfactant solution at a concentration far below the CMC where only surfactant monomers were present. In other words, we inferred the structural transition of BSA was caused by ionic surfactant monomers.

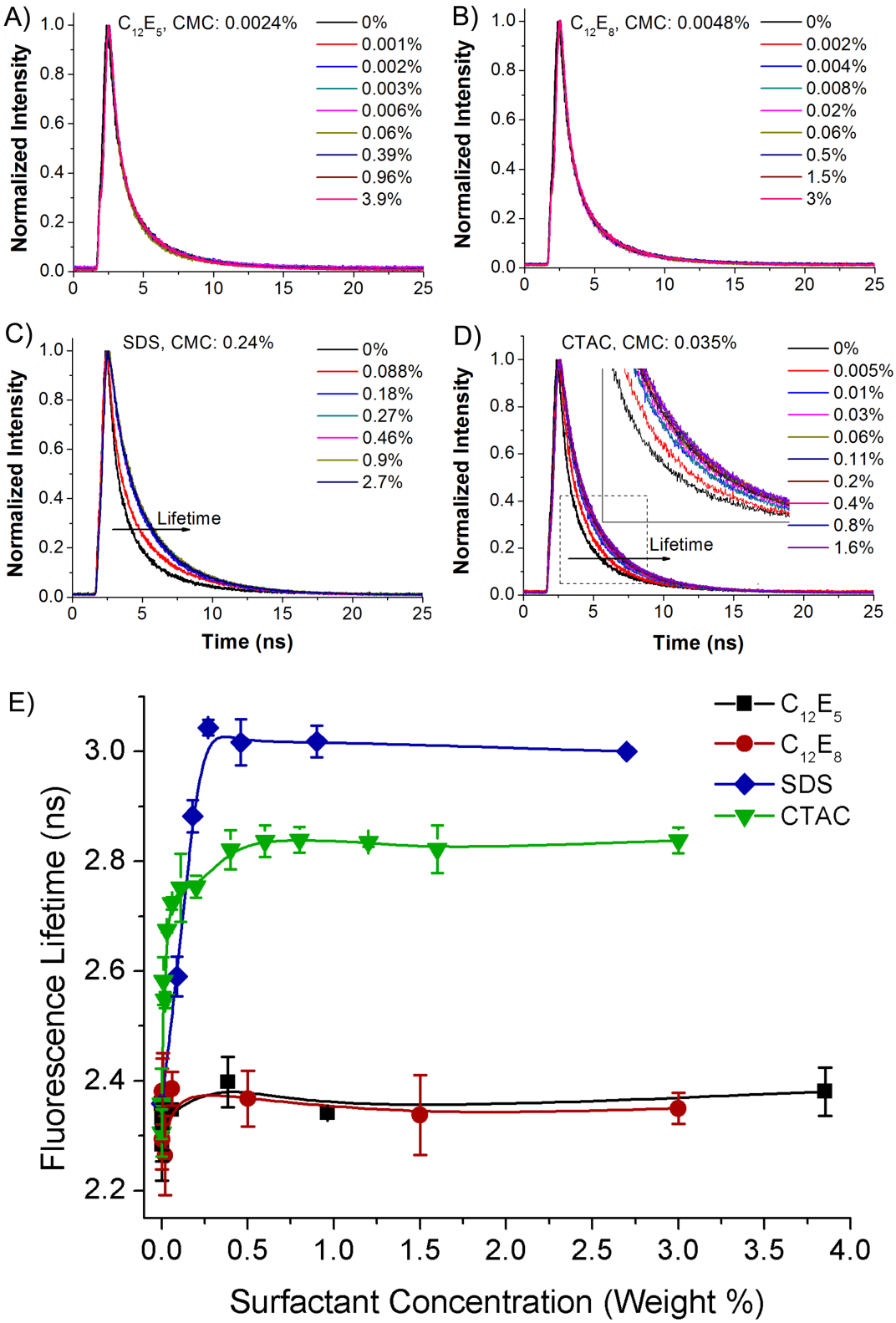

Figure 2.4: (A-D) Fluorescence decay curves of ATTO-BSA in $C_{12}E_5$, $C_{12}E_8$, SDS and CTAC solutions with various concentrations of surfactant. The overlapped curves in (A) and (B) suggested a constant fluorescence lifetime of ATTO-BSA in $C_{12}E_5$ and $C_{12}E_8$ solutions, while right-shifted curves to longer time region in (C) and (D) indicated the increase in the lifetime of the probe in SDS and CTAC solutions below the CMC; (E) Average values of fluorescence lifetimes of ATTO-BSA in the $C_{12}E_5$, $C_{12}E_8$, SDS and CTAC solutions as a function of concentration determined by Eq. 1.9. The lifetimes of the probe in the $C_{12}E_5$ or $C_{12}E_8$ solutions were roughly the same as in pure water, however, sudden jumps were observed in ionic surfactant solutions.

Fluorescence Lifetime Analysis

The fluorescence lifetime of a fluorophore is determined by its chemical structure and shape [65]. However it can be affected by the external nanoenvironment and intermolecular interactions [24]. To confirm the structural transition of BSA originating from the protein-surfactant interaction, we analysed the fluorescence lifetime properties of ATTO-BSA in the four surfactant solutions. We observed that the fluorescence decay of ATTO-BSA in nonionic surfactant $C_{12}E_5$ and $C_{12}E_8$ solutions with various concentration did not change apparently (Fig. 2.4 (A) and (B)). The value of fluorescence lifetime fitted by Eq. 1.9 was 2.36 ns and independent on the surfactant concentration. In contrast, sudden increases in the fluorescence lifetime of ATTO-BSA were observed in the ionic surfactant solutions (Fig. 2.4 (C) and (D)). It increased by 28%, from 2.36 to 3.0 ns, in SDS solution with the transition concentration at 0.088% (below its CMC) and by 21%, from 2.36 to 2.84 ns, in CTAC solution with the transition point at 0.005% (below its CMC). In both cases these transitions occurred at the same concentration as observed in FCS experiments.

The increased fluorescence lifetime of ATTO-BSA in ionic surfactant solutions indicated different nanoenvironments around ATTO-488, which might result from either the unfolding of BSA or from the presence of surfactants. In order to find out the causes behind the fluorescence lifetime transition of ATTO-488, we measured the fluorescence lifetime of free ATTO-488 in these surfactant solutions. The fluorescent intensity decay of ATTO-488 in the four surfactant solutions with various concentrations displayed the same profile (Fig 5 (A)). The fitted value of the fluorescence lifetime of ATTO-488 was 4.17 ns, close to the reported result (4.1 ns) from Kapusta [68]. In contrast, the fluorescence lifetime of ATTO-488 decreased by as many as 44%, to 2.36 ns, after binding to BSA (Fig 5 (B)). We inferred that the fluorescence lifetime of ATTO-488 was only influenced by BSA but not by the surfactants in solutions.

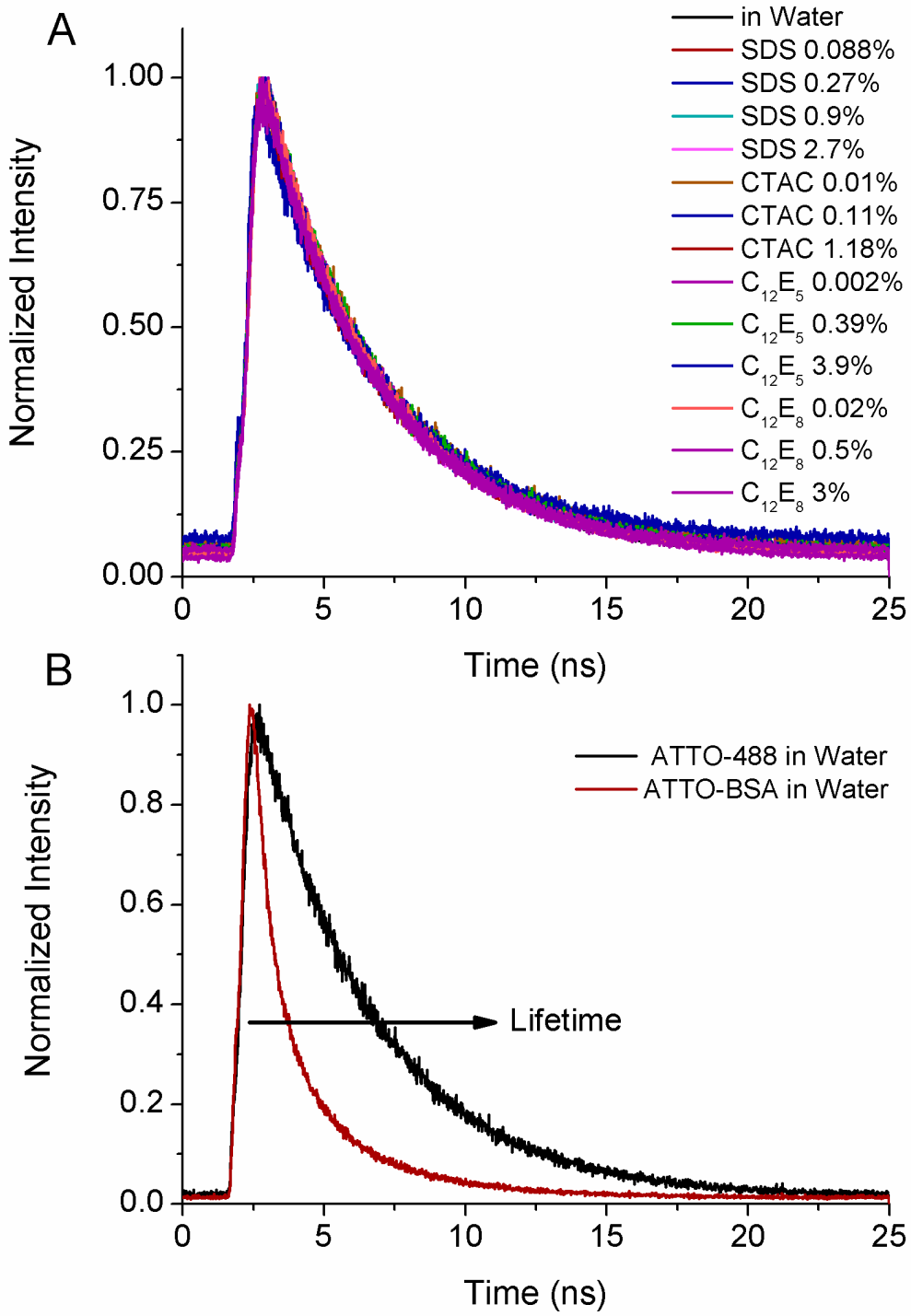

Figure 2.5: (A) Fluorescence decay curves of dye ATTO-488 in $C_{12}E_5$, $C_{12}E_8$, SDS and CTAC solutions with selected concentrations. The overlapped curves suggested marginal changes in the fluorescence lifetime of ATTO-488 in the four surfactant solutions. (B) Fluorescence decay curves of dye ATTO-488 and ATTO-BSA in water. A dramatically decrease in the fluorescence lifetimes of ATTO-488 was observed after labelling to BSA.

Therefore we attributed the fluorescence lifetime transition of ATTO-BSA in the ionic surfactant solutions to the structural changes of BSA. According to Eq. 1.10, the sum of rate constant of radiative and nonradiative processes, $k_{\mathrm{R}} + k_{\mathrm{NR}}$, was inversely proportional to the average fluorescence lifetime. The unfolding of BSA reduced its quenching effect on the dye, leading to the decrease in k_{NR}. Consequently, the fluorescence lifetime of ATTO-488 increased suddenly after the structural transition of BSA. This point of view got support from the work of Lober's group. They found that the fluorescenc lifetime of dye 8-ANS labelled to the bovine carbonic anhydrase B and human $\alpha-$lactalbumin significantly increased after the denaturation of protein by guanidinium chloride [69]. In contrast, the nonradiative process in ATTO-BSA was not influenced by nonionic surfactant solutions at all due to the unchanged structure of BSA. The fluorescence lifetime of the probe in nonionic surfactant solutions stayed constant.

Noticeably, the structural transition of BSA in ionic surfactant solutions obtained from the fluorescence lifetime analysis coincided with the results from FCS measurements. We concluded that the structural transition of BSA was induced by ionic surfactant monomers but not micelles, since the concentrations where the transition occurred were far below the CMC of surfactants. The hydrodynamic radii and fluorescence lifetimes of ATTO-BSA before and after the structural transitions are summarized in Table 2.1.

Table 2.1: Comparison of hydrodynamic radii (R_{h}) and fluorescence lifetimes (τ_{fl}) of ATTO-BSA in water and various surfactant solutions.

	R_{h} (nm)	τ_{fl}(ns)
Without structural change		
Water	3.88 ± 0.029	2.36 ± 0.064
$C_{12}E_5$	3.99 ± 0.11	2.34 ± 0.041
$C_{12}E_8$	$(4.01 \pm 0.092)(3.79)^*$	2.34 ± 0.044
With structural transition		
SDS (2.7%)	$(6.16 \pm 0.029)(5.9)^*$	3.02 ± 0.028
CTAC (3.0%)	6.52 ± 0.037	2.84 ± 0.023

*Reference values from dynamic light scattering experiment in Ref. 59

Chapter 3

Dye/Micelle Interactions

Equilibrium and rate constants are quantitative descriptors for processes of complex-formation in various chemical and biological systems. However, these parameters are difficult to determine, especially in the locally confined, heterogeneous, and dynamically changing living matter. In this chapter we address this challenge by applying FCS and STED-FCS separately to quantitatively study the binding/unbinding kinetics of complex formation in a model system of the dyes and micelles in water. The equilibrium and rate constants were determined from the experiments supplemented by our analytical formula for the probes undergoing a diffusion-reaction process. This work may pave a promising application toward quantitative characterization of intermolecule interactions *in vitro* and *in vivo*.

3.1 Theoretical Section

Formation of Dye-micelle Complexes

Surfactant molecules in an aqueous solution are inclined to aggregate to form micelles (denoted A) by self-assembly when the concentration is above the critical micelle concentration (CMC). The concentration of micelles $[A]$ can be determined

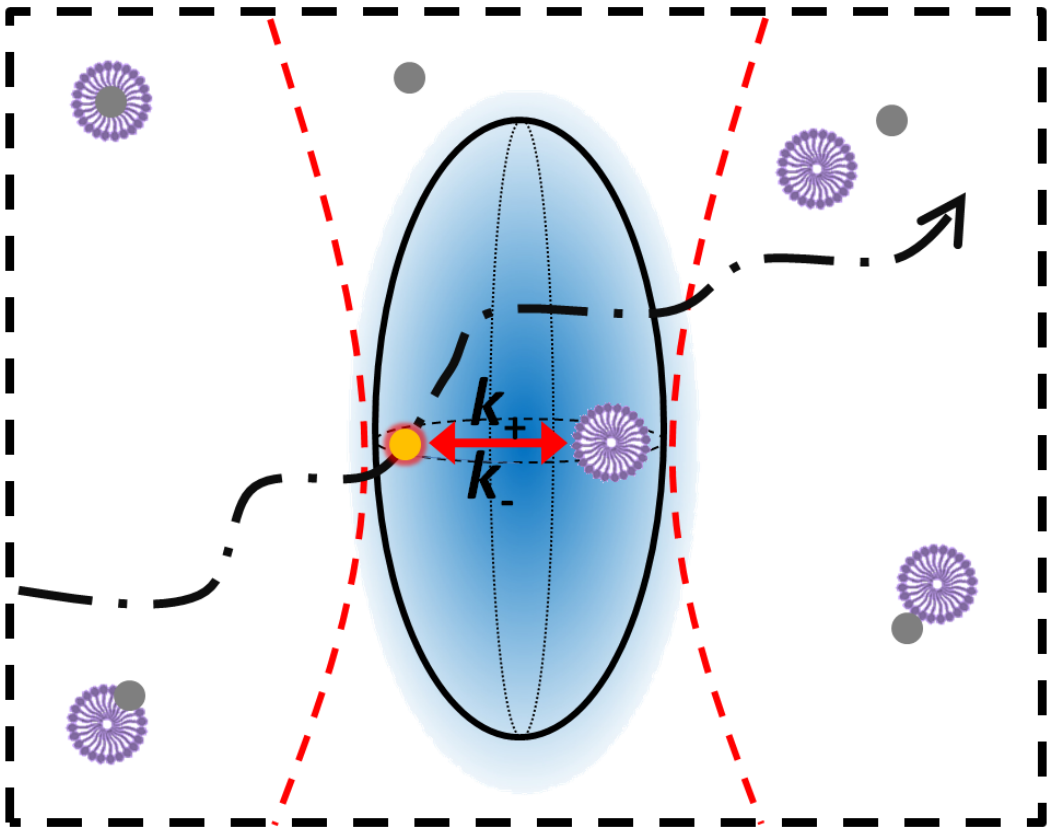

Figure 3.1: Schematic representation of dye-micelle interaction within the FV of FCS. Kinetic information such as the equilibrium and rate constants for the dye-micelle interactions can be obtained from the analysis of experimental data using proper theoretical model.

from the surfactant concentration $[S]$ as follows:

$$[A] = ([S] - [\mathrm{CMC}])/N_{\mathrm{ag}}, \tag{3.1}$$

where N_{ag} is the mean number of aggregated surfactant molecules in one micelle. In dilute solution N_{ag} is constant since the shape and size of micelles are usually fixed. The values of N_{ag} and CMC for all surfactants used in this work are listed in Table 3.1.

A dye molecule diffusing in a micellar solution can be either in a free-diffusion state or bound-diffusion state due to the intermolecular interaction [73–75]. The particular advantages of dye-micelle model for the intermolecular interaction studies have already been introduced previously [31]: high stability of each component, simple interaction mechanism, no side-products, large difference in the diffusion

Table 3.1: Diffusion coefficients, hydrodynamic radii, electric charges, critical micelle concentrations (CMC) and the aggregation numbers (N_{ag}) of studied samples. All values are obtained from literatures, FCS or DLS measurements at 25 ℃.

	D ($\times 10^{-10}$ m^{2}s^{-1})	R_h (nm)	Charge	CMC (mM)	N_{ag}
Rh110	(4.7 ± 0.4) [70]	(0.52 ± 0.05)	Zwitterionic		
ATTO-488	(4.0 ± 0.1) [71]	(0.62 ± 0.02)	Zwitterionic		
ATTO-647N	$(3.5 \pm 0.1)^*$	(0.62 ± 0.02)	Cationic		
$C_{12}E_8$	$(0.34 \pm 0.01)^*$	$(7.2 \pm 0.02)^*$	Neutral	0.082 [55]	95 [72]
SDS	$(0.92 \pm 0.02)^*$	$(2.7 \pm 0.06)^*$	Negative	8.2 [58]	60 [58]
CTAC	$(0.8 \pm 0.01)^*$	$(3.1 \pm 0.04)^*$	Positive	1.1 [61]	80 [61]

*Values from FCS measurements; *Values from DLS measurements.

coefficient between the free and bound probe, and full reversibility of the process. The binding/unbinding processes between dyes and micelles can be treated as a pseudo-first-order reaction with the equilibrium constant K:

$$\mathrm{A} + \mathrm{B} \overset{K}{\rightleftharpoons} \mathrm{C}, \tag{3.2}$$

where B and C denote the dyes and dye-micelle complexes, respectively. The equilibrium constant K is related to the association and dissociation rate constants (k_+, k_-) and the concentrations of each component at the equilibrium state ($[A]^{\mathrm{eq}}$, $[B]^{\mathrm{eq}}$, $[C]^{\mathrm{eq}}$), as:

$$K = \frac{k_+}{k_-} = \frac{[C]^{\mathrm{eq}}}{[A]^{\mathrm{eq}}[B]^{\mathrm{eq}}}. \tag{3.3}$$

The relaxation rate R of intermolecular interaction, which describes the rate of a reaction's return to equilibrium, is defined as [26]:

$$R = k_+([A]^{\mathrm{eq}} + [B]^{\mathrm{eq}}) + k_-. \tag{3.4}$$

Because the micelle concentration is always much higher than the dye concentration in our FCS experiments, i.e., $[A]^{\mathrm{eq}} \gg [B]^{\mathrm{eq}} \approx 10^{-9}$ M, we use the approximation:

$$R = k_+[A]^{\mathrm{eq}} + k_- \approx k_+[A] + k_-. \tag{3.5}$$

It follows that the higher the micelle concentration, the larger the relaxation rate of dye-micelle interaction (i.e., the shorter the time of the return to the equilibrium). Combining Eq. 3.3 and 3.5, we get

$$R = k_+[A] + k_+/K. \tag{3.6}$$

Approximate Form of ACF

Due to the dye/micelles interaction there are three diffusional components present in the FV of FCS: micelles (A), dyes (B) and dye-micelle complexes (C). The diffusion coefficients of each component are denoted D_{A}, D_{B} and D_{C}, respectively. To investigate the binding/unbinding processes of the dye-micelle interaction, characterized by the equilibrium constant K and relaxation rate R, we use an approximate form of the FCS autocorrelation function ($G_{\mathrm{a}}(t)$) derived in the framework of Magde's theory [25–27]. The derivation of $G_{\mathrm{a}}(\tau)$ is based on the following two assumptions: (1) The diffusion coefficient of micelle is constant and much smaller than that of the dye, then the diffusion coefficient of the dye-micelle complex can be approximated as $D_{\mathrm{C}} = D_{\mathrm{A}} \ll D_B$; (2) The quantum yield of the dye fluorescence, Q_{B}, does not change after binding to the micelle, i.e., $Q_{\mathrm{B}} = Q_{\mathrm{C}} = Q$. This assumption has been confirmed by quantum yield measurements [31].

Taking into account the intrinsic triplet state transition of fluorescent dyes, we obtain the following approximate formula for the autocorrelation function:

$$\begin{aligned} G_a(\tau) = \frac{1}{N}\left(1+\frac{p}{1-p}\exp\left(\frac{-\tau}{\tau_{\mathrm{t}}}\right)\right)\Bigg\{ & h\left(\frac{\tau}{\tau_+}\right)\left[1-\exp\left(-R\tau_\Delta\left(1+\frac{\tau}{\tau_+}\right)\right)\right] \\ & + \beta h\left(\frac{\tau}{\tau_{\mathrm{A}}}\right)\left[\exp\left(-R\tau_\Delta\left(1+\frac{\tau}{\tau_+}\right)\right)\right] + \\ & (1-\beta)\,h\left(\frac{\tau}{\tau_{\mathrm{B}}}\right)\left[\exp\left(-R\tau\right)\exp\left(-R\tau_\Delta\left(1+\frac{\tau}{\tau_-}\right)\right)\right]\Bigg\}, \end{aligned} \tag{3.7}$$

in which

$$\tau_{\mathrm{A}} = L^2/4D_{\mathrm{A}},\ \tau_{\mathrm{B}} = L^2/4D_{\mathrm{B}},\ \tau_\pm = L^2/4D_\pm,\ \tau_\Delta = L^2/4D_\Delta, \tag{3.8}$$

are the effective diffusion times of the probe through the FV. They are related to the effective diffusion coefficients respectively as

$$D_+ = D_{\mathrm{A}}\beta + D_{\mathrm{B}}(1-\beta),\ D_- = D_{\mathrm{A}}(1-\beta) + D_{\mathrm{B}}\beta,\ D_\Delta = D_{\mathrm{A}} - D_{\mathrm{B}}, \tag{3.9}$$

where

$$\beta = k_+[A]^{\mathrm{eq}}/R = K[A]^{\mathrm{eq}}/(1+K[A]^{\mathrm{eq}}). \tag{3.10}$$

The function

$$h(t) = (1+t)^{-1}(1+t/\kappa^2)^{-1/2} \tag{3.11}$$

is the normalized autocorrelation function for the single-component diffusion and t denotes the dimensionless residence time.

The parameters characterizing the dimension of the focal volume: H, L and κ, are known from the calibration measurements of reference fluorescent dyes with known diffusion coefficient D_{B}. D_{A} is the diffusion coefficient of micelles determined by DLS. The equilibrium constant was determined by TDA. The rest parameters (τ_{A}, τ_{B}, τ_{Δ}, $\tau_{\pm}$ and β) whose values depend on dimensions of FV and micellar concentration in Eq. 3.7 can be exactly calculated and then fixed in the fitting procedure. **The target quantity R is the only free parameter needed to be fitted, besides the intrinsic triplet-state parameters (p and τ_{t}) which have confined values**.

In the case of dyes diffusing in concentrated micelle solutions where the relaxation rate for dye-micelle interaction is extremely big, we have $R\tau_{\Delta} \to \infty$. Then Eq. 3.7 reduces to the known form for the single-component diffusion (cf. Eq. 1.24):

$$G_{\infty}(\tau) = \frac{1}{N}\left(1 + \frac{p}{1-p}\exp\left(\frac{-\tau}{\tau_{\mathrm{t}}}\right)\right) h\left(t/\tau_{+}\right). \tag{3.12}$$

In the case of dyes diffusing in the diluted micelle solutions where $R\tau_{\Delta} \approx 0$, Eq. 3.7 reduces to:

$$G_0(\tau) = \frac{1}{N}\left(1 + \frac{p}{1-p}\exp\left(\frac{-\tau}{\tau_{\mathrm{t}}}\right)\right) \left[\beta h\left(t/\tau_{\mathrm{A}}\right) + (1-\beta)\, h\left(t/\tau_{\mathrm{B}}\right)\right], \tag{3.13}$$

which is the same expression as the ACF for the two-component diffusion [76].

3.2 FCS Section

We recorded the diffusion of rhodamine 110 in CTAC solutions and observed a gradual shift of the autocorrelation curves toward long-time region as the surfactant concentration increased (see Fig. 3.2). However, the viscosity of such diluted

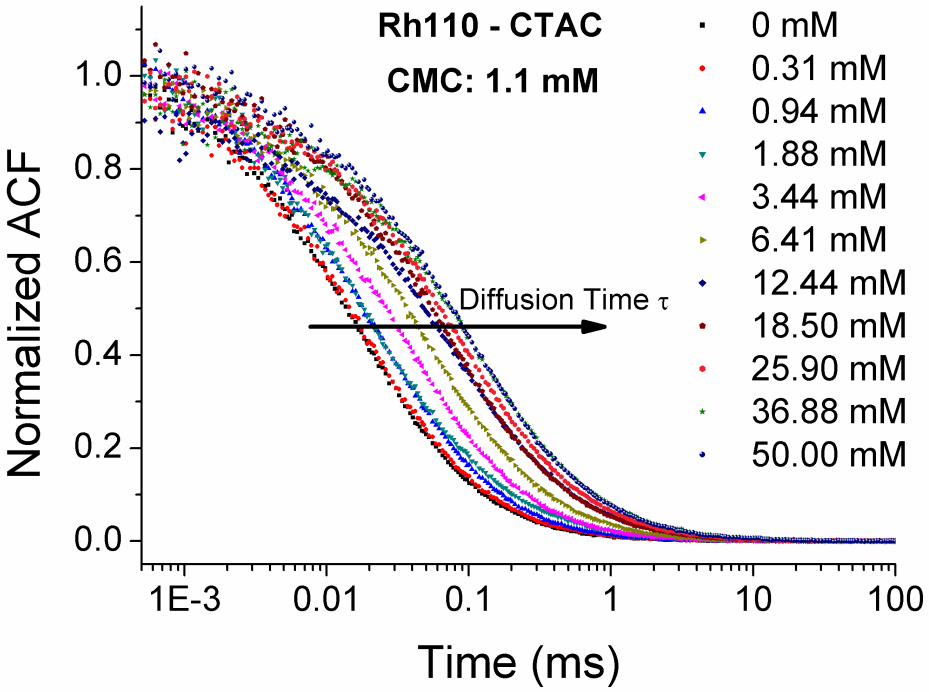

Figure 3.2: Normalized experimental autocorrelation curves of rhodamine 110 diffusing in the CTAC solutions at various concentrations. The diffusion times of rhodamine 110 shifted gradually to the long-time region as the increases of CTAC concentration.

solutions did not change noticeably with the surfactant concentration. Thus, the increase in the diffusion time of rhodamine 110 implied that the free diffusion of dyes was gradually hindered due to the formation of dye-micelle complexes. The more dye-micelle complexes were formed in the solution, the longer the diffusion time was observed.

Such a hindered diffusion was also reported in the work of Zettl *et al* [75], in which they focused on the formation of micelles near the CMC. They analysed their experimental autocorrelation curves using the two-component model for FCS with a simple assumption that the relaxation rate of the dye-micelle reaction was much longer than the typical diffusion time of micelle through the FV. However without a proper analysis of the relaxation rate of the reaction that occur in the system, two-component model may give false values of the diffusion times and the

fractions of each component. Consequently, the size of CTAC micelles probed by different probes was not even equal if the curves were fitted by the two-component model [75]. Two-component model can only be applied to the situation where the relaxation rate of the intermolecular interaction is much smaller than the diffusion time of probes in the FV. In this case we observe two diffusive components in the system, i.e., the probes and complexes.

Analysis of FCS Data with $G_{\mathrm{a}}(\tau)$

The autocorrelation function, given by Eq. 3.7, is dedicated to determine the relaxation rate of moderate interaction, in which the residence time of the probe is smaller than the relaxation rate. We measured the collective diffusion coefficient (D_{c}) of the CTAC, SDS and $C_{12}E_8$ micelle in aqueous solution as a function of micellar concentration at 25 ℃ by DLS (cf. Fig. 3.3). It reduced to self-diffusion coefficients D_0 of micelles when extrapolated the linear fit to zero concentration using Eq. 1.30. For each micelle the obtained D_0 from DLS was consistent with the published results [61, 61, 77]. Since we measured the diffusion of dye-micelle complex at nanomole concentration in FCS, it was reasonable to use D_0 from DLS for all the micelles. Additionally, our previous small angle neutron scattering (SANS) experiments and literature data also showed that the size and structure of micelles do not change in such dilute region [78, 79].

The equilibrium constant of the Rh110-CTAC interaction was determined by TDA. We used a long, coiled capillary to measure the diffusion coefficients of rhodamine 110 in water and in CTAC solutions according to Eq. 1.33. The determined equilibrium constant for the Rh110-CTAC system was 4.28×10^4 M^{-1} according to Eq. 1.35.

After obtaining the equilibrium constant K from TDA and the diffusion coefficients of micelles from DLS, we calculated the values of parameters τ_{Δ}, $\tau_{\pm}$ and β according to Eq. 3.8, 3.9 and 3.10. Then we fitted the autocorrelation

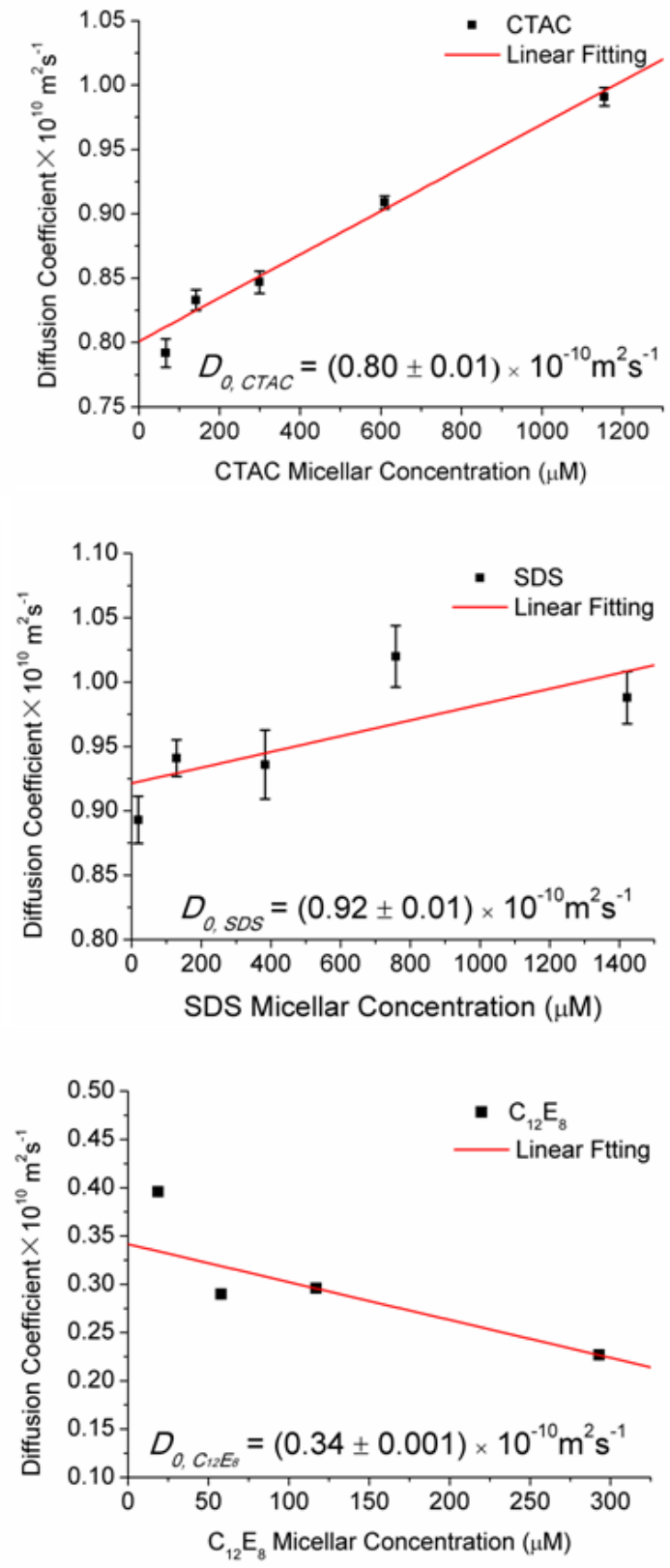

Figure 3.3: Linear fits of the collective diffusion coefficients of CTAC, SDS, and $C_{12}E_8$ micelles in aqueous solutions via Eq. 1.30. Extrapolation concentrations to infinite dilution gave the self-diffusion coefficient of each micelle. All measurements were performed by DLS at 25 ℃. These plots showed that nonionic micelles attract each other weakly, whereas ionic ones repelled each other.

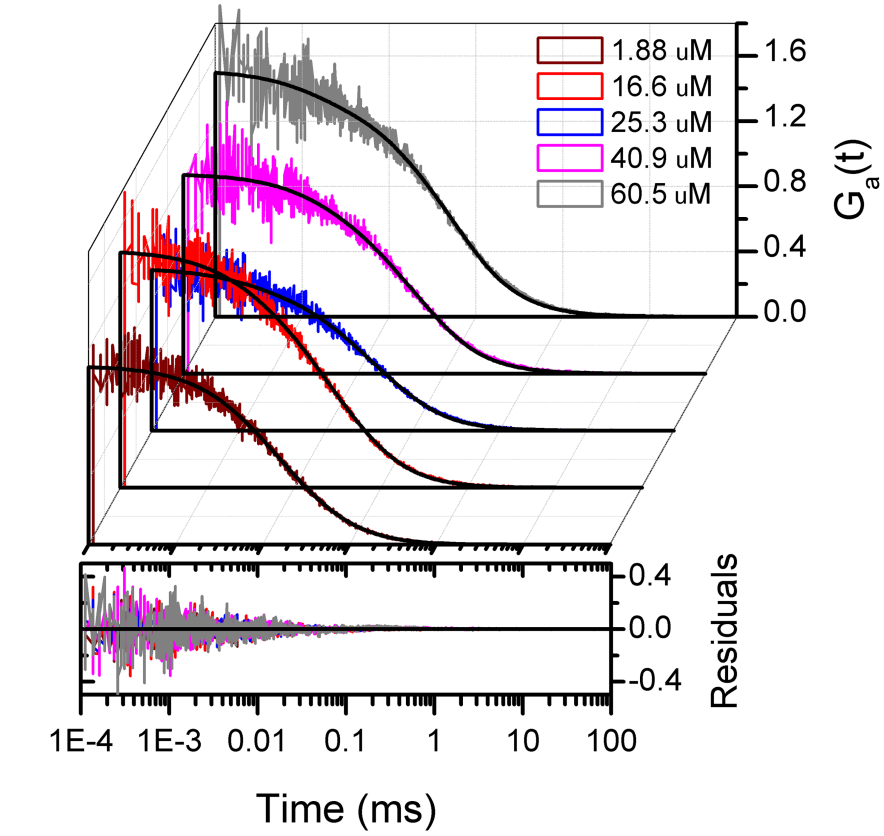

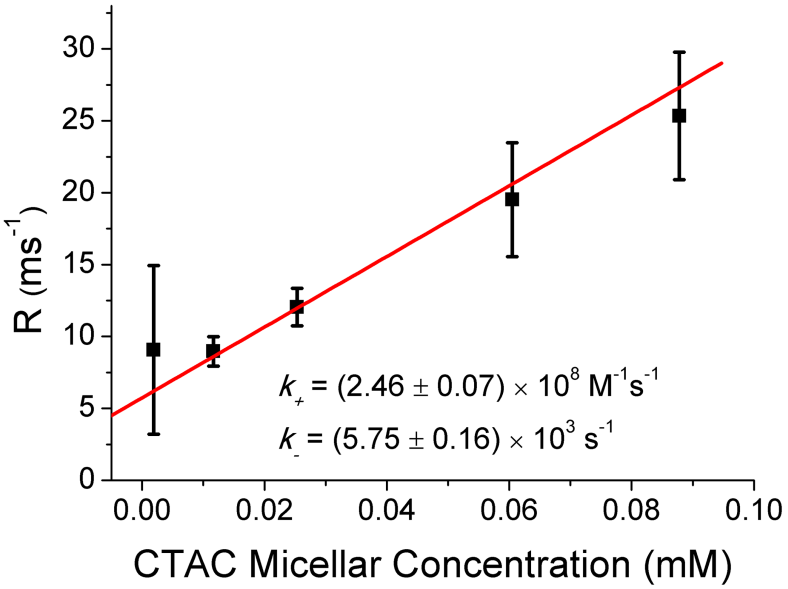

Figure 3.4: Upper panel: experimental autocorrelation curves of rhodamine 110 diffusing in diluted solutions of CTAC and the fitting curves using Eq. 3.7. The plotted residuals corresponded to the deviations of the fits from experimental data. Lower panel: the fitted values of R plotted as a function of CTAC micelle concentration according to Eq. 3.6, in which K was fixed at value known from TDA measurements. The association rate constant k_+ was obtained from the slope of fitting (red line), then the dissociation rate k_- was calculated according to Eq. 3.3.

curves for rhodamine 110 diffusing in the CTAC micelle solutions with Eq. 3.7 (see Fig. 3.4, upper panel). The values of R obtained from the fits were plotted as a function of CTAC micellar concentration (Fig. 3.4, lower panel). The association rate constant $k_+ = 2.46 \times 10^8$ $M^{-1}s^{-1}$ were obtained from the slope of the linear fit using Eq. 3.6, in which the value of K was also inferred from TDA and fixed at 4.28×10^4 M^{-1} during the fitting process. The determined k_+ for the Rh110-CTAC system was one order of magnitude higher than that of DNA-EtBr interaction revealed by Magde *et al* [26]. The value of k_-, calculated according to Eq. 3.3, amounted to 5.75×10^3 s^{-1}.

Determination of the Equilibrium Constant by FCS

Since R increased as the micelle concentration increase we expected that at sufficiently high concentration of micelle the fast limit (i.e., Eq. 3.12) of Eq. 3.7 could be applied due to $R\tau_\Delta \to \infty$. Then we determined the equilibrium constant from the dependence of the effective diffusion coefficient D_+ on the concentrations of micelles according to the definition of D_+ and β:

$$K[A] = \frac{D_+ - D_B}{D_A - D_+}, \tag{3.14}$$

where D_+ was calculated from the relation $D_+ = L^2/4\tau_+$, in which τ_+ was the fitted effective diffusion time of dye through the FV using $G_\infty(\tau)$.

We measured the diffusion of rhodamine 110 in a series of CTAC micellar solutions at relatively high concentrations. The experimental curves were well fitted by $G_\infty(\tau)$ apparently (see Fig. 3.5). Then substituting D_+ determined from FCS and the self-diffusion coefficient of micelles D_A obtained from DLS into Eq. 3.14, we obtained the equilibrium constant K from the slope of the linear fit as a function of micelle concentration (cf. lower panel of Fig. 3.5). For the Rh110-CTAC system the equilibrium constant determined by Eq. 3.12 was 4.32×10^4 M^{-1}, consistent with the value of 4.28×10^4 M^{-1} obtained from TDA measurements.

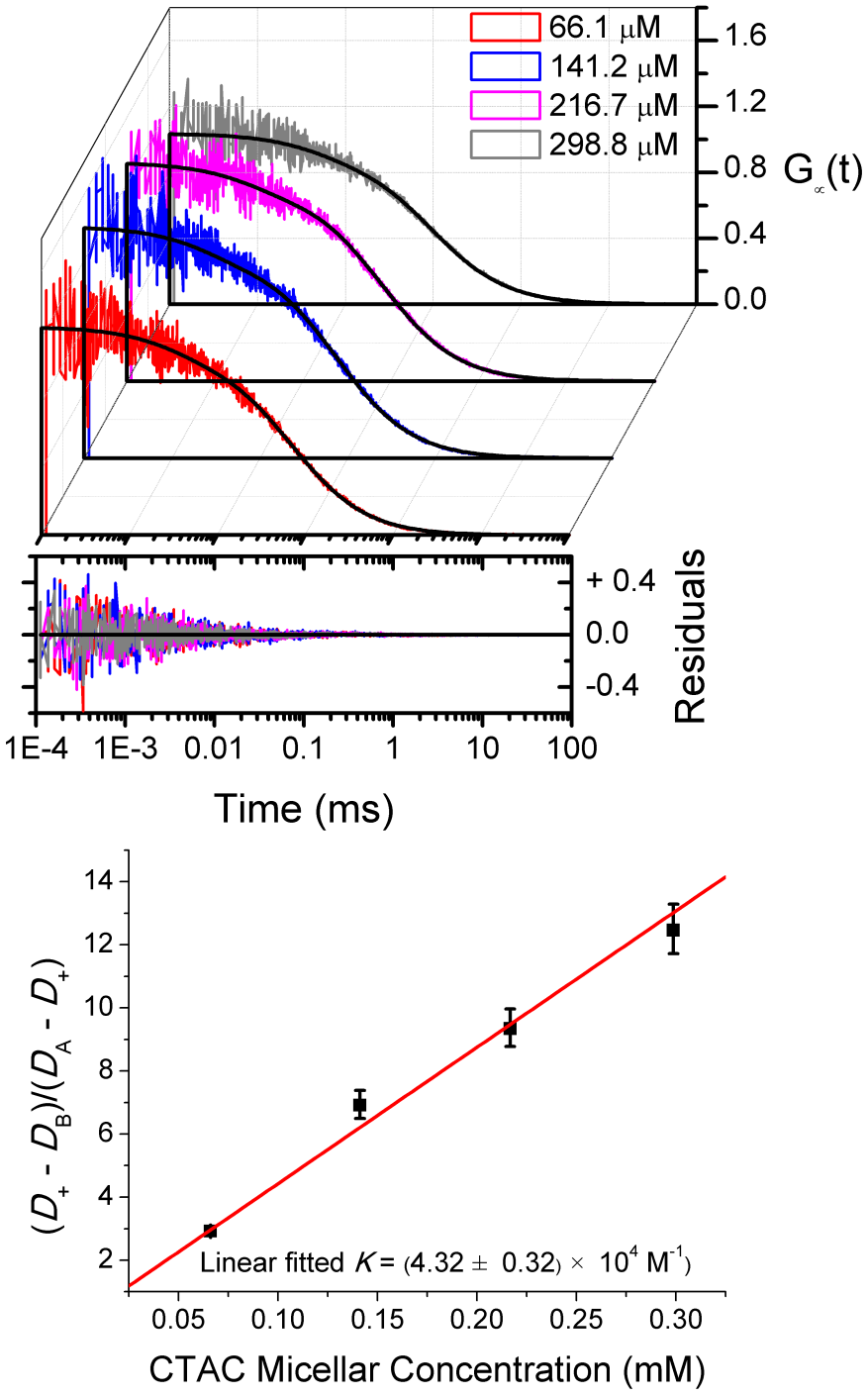

Figure 3.5: Upper panel: experimental autocorrelation curves for rhodamine 110 diffusing in the relatively concentrated solutions of CTAC micelle and their fitting curves using Eq. 3.12. Lower panel: fitted equilibrium constant K of Rh110-CTAC interaction from the slope of fitting using Eq. 3.14.

Weak and Strong Interactions

We also utilized FCS to probe the intermolecular interactions between dye ATTO-488 and other micelles, i.e., $C_{12}E_8$ and SDS, at the concentrations both below and above their CMCs. We did not observe any noticeable changes in the diffusion time of ATTO-488 in the two surfactant solutions from the experimental ACFs (see Fig. 3.6 (A) and (B)). The values of the effective diffusion time obtained from the fits of experimental data using $G_\infty(\tau)$ were roughly the same as in pure water. This meant that the intermolecular interactions in these surfactant and micelle solutions were too weak to hinder the free diffusion of ATTO-488. Our previous work on the mobility of fluorescence dye TAMRA in the low concentrated solutions of hexaethylene glycol monododecyl ether ($C_{12}E_6$) agreed with the present result [57]. The diffusion coefficient of TAMRA also did not change in the C_{12} E_6 solutions within the same range of surfactant concentration where the viscosity of the surfactant solution was the same as that of water.

In contrast, the effective diffusion time of ATTO-488 in CTAC solutions and rhodamine 110 in SDS solutions experienced sudden increases when the surfactant concentrations were just above their CMC (see Fig. 3.6 (C) and (D)). The dyes were supposed to bind to the micelles immediately and then diffuse together through the FV. In Dosche and Ghosh works they also observed such attachment of hydrophobic dyes to various surfactant micelles from FCS [80, 81].

The formation of dye-micelle complexes was mainly driven by the hydrophobic effect and electrostatic forces. Higher affinity of the zwitterionic dye ATTO-488 to the cationic CTAC micelles than the anionic SDS and neutral $C_{12}E_8$ micelles could be attributed to the stronger hydrophobic effect from the CTAC micelle which possesses four more alkyl groups than SDS and $C_{12}E_8$. The interactions between rhodamine 110 and $C_{12}E_8$, CTAC, SDS micelles were getting stronger gradually, which was mainly attributed to the increases of electrostatic interactions between them.

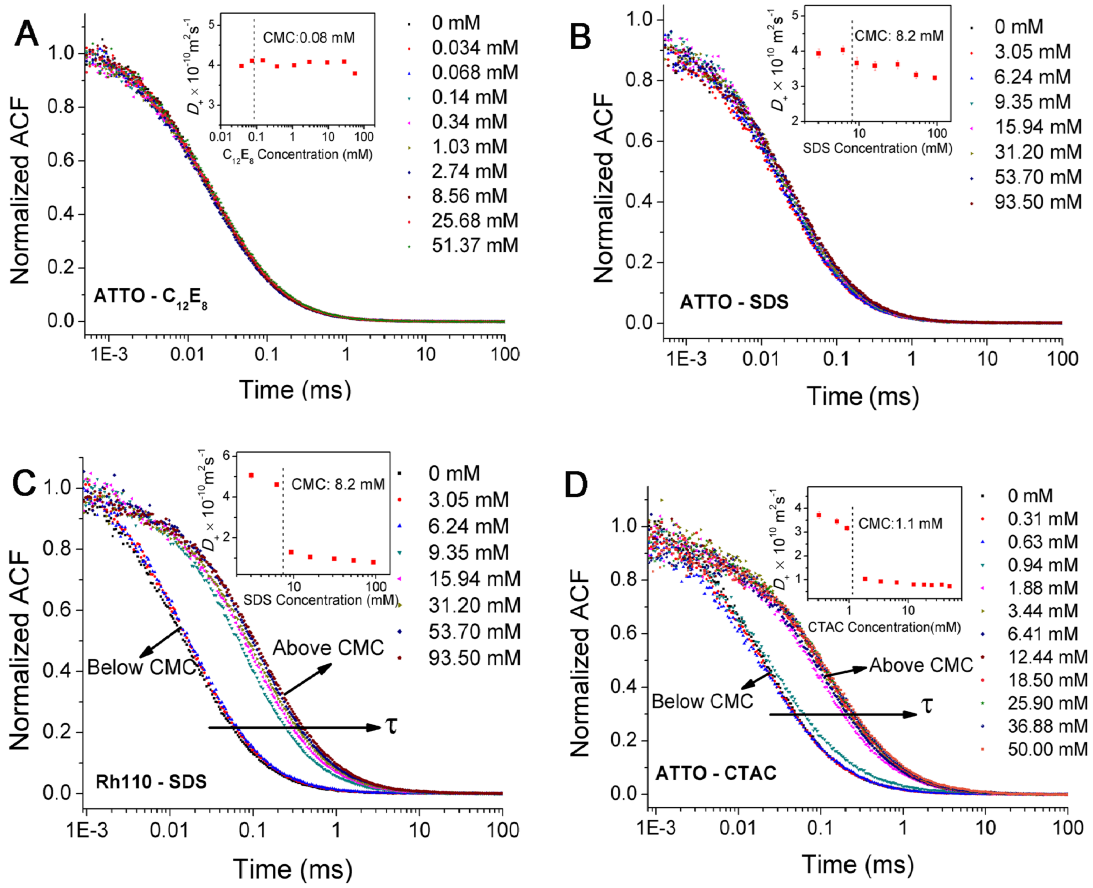

Figure 3.6: (A-D) Normalized experimental autocorrelation curves for ATTO-488 and rhodamine 110 in the solutions of $C_{12}E_8$, SDS and CTAC with various surfactant concentrations. Inset: the effective diffusion coefficients (D_+) obtained from the fits of experimental curves using Eq. 3.12. The overlapping sets of data points in (A) and (B) indicated that the diffusion times of ATTO-488 in the $C_{12}E_8$ and SDS solutions were independent on the surfactant concentrations. Whereas in (C) and (D), sudden increases in the diffusion time were observed in the Rh110-SDS and ATTO-CTAC systems at the concentrations just above the CMC. The dyes bound to the ionic micelles immediately once they just encounter.

Kinetics of Dye-Micelle Interactions

We categorized the dye-micelle interactions as: weak, intermediate or strong, according to the dependence of D_+ on the surfactant concentration. For weak interactions, i.e., ATTO-$C_{12}E_8$ or ATTO-SDS systems, D_+ changed marginally as a function of the surfactant concentration. It indicated the free diffusion of ATTO-488 in these solutions (see inset of Fig. 3.6 (A) and (B)). For strong interactions, e.g., Rh110-SDS or ATTO-CTAC systems, D_+ dropped sharply when the surfactant concentration exceeded the CMC (see inset of Fig. 3.6 (C) and (D)). This demonstrated that almost all dye molecules bound strongly to the micelles. For intermediate interactions, the Rh110-CTAC system for example, D_+ decreased moderately as the surfactant concentration increased. These three concentration-related behaviours of D_+ observed from FCS were also reported in the work of Vagias group, where they used molecular dynamics to simulate the diffusion of spherical tracers in a generic bead-spring polymer solution. Three kinds of diffusion were observed from the different levels of attraction between the tracer and polymer in the simulation [82].

Since FCS showed a good accuracy in determining the equilibrium constant for Rh110-CTAC interaction at relatively high concentrations of micelles, we also applied this method to other dye-micelle systems. In Table 3.2, we showed the values of K for the studied dye-micelle interactions. In the case of strong interactions (Rh110-SDS and ATTO-CTAC systems), the fitted values of K were roughly one order of magnitude larger than those of intermediate ones. The reported value of K for the interaction between rhodamine 123 and $C_{12}E_7$ was 1.6×10^4 M^{-1} [74], very close to the value of Rh110-$C_{12}E_8$ interaction in this work.

Next, we used the equilibrium constant obtained from FCS experiments with concentrated micelle solutions to retrieve the relaxation rates of the same dye-micelle system with diluted solutions of micelles using Eq. 3.7. Then we determined the rate constants k_+ and k_- of intermediate and strong interactions based

Table 3.2: The equilibrium constants K, association k_+ and dissociation k_- rate constants, and the association rate constants of the diffusion-controlled reaction estimated by Smoluchowski equation k_{dc}, of the studied dye-micelle systems. K was obtained from Eq. 3.14 and $k_\pm$ were obtained from Eq. 3.7 and 3.6 respectively.

	K ($\times 10^4$ M^{-1})	$-\Delta G$ (kJ mol^{-1})	k_+ ($\times 10^8$ M^{-1}s^{-1})	k_- ($\times 10^3$ s^{-1})	k_{dc} ($\times 10^{10}$ M^{-1}s^{-1})
Rh110-$C_{12}E_8$	2.32 ± 0.21	24.9	12.16 ± 6.07	52.4 ± 26.2	2.9
Rh110-CTAC	4.32 ± 0.32	26.44	2.14 ± 0.01	6.58 ± 0.06	1.5
Rh110-SDS	15.8 ± 0.09	29.66	0.51 ± 0.08	0.32 ± 0.05	1.36
ATTO-CTAC	46.7 ± 7.8	32.34	0.74 ± 0.01	0.16 ± 0.01	1.35

on the relation between K and R (cf. Eq. 3.6), which were collected in Table 3.2 together with the diffusion-controlled association rate constant k_{dc}. The values of k_+ in our dye-micelle systems were roughly one to two orders of magnitude smaller than the k_{dc}. The latter was estimated from the Smoluchowski equation:

$$k_{\mathrm{dc}} = 4\pi D_{\mathrm{dm}} R_{\mathrm{dm}} N_{\mathrm{A}}, \tag{3.15}$$

where D_{dm}, R_{dm} are the sums of the diffusion coefficients and the hydrodynamic radii of the dyes and micelles, respectively, and N_{A} is Avogadro's constant. The reported values of the association rate constant for various dye-micelle interactions ranged from 10^6 M^{-1}s $^{-1}$ to the diffusion-controlled limit, i.e., 10^{10} M^{-1}s^{-1} [73, 74, 83].

Hence we describe the dye-micelle reaction as a two-step process: the encounter formation and complex formation:

$$A + B \overset{k_{\pm \mathrm{dc}}}{\longleftrightarrow} [A \cdot B] \overset{k_{\pm \mathrm{r}}}{\longleftrightarrow} C \tag{3.16}$$

In the first step, one micelle and one dye molecule get into contact to form an encounter intermediate $[A \cdot B]$ driven by free diffusion under the diffusion-controlled rate k_{dc}. Next, the dye-micelle complex is formed through the hydrophobic and electrostatic interactions with a reaction rate k_{r}. The value of k_{r} can be simply estimated via [84]:

$$\frac{1}{k_+} = \frac{1}{k_{\mathrm{dc}}} + \frac{1}{k_{\mathrm{r}}}. \tag{3.17}$$

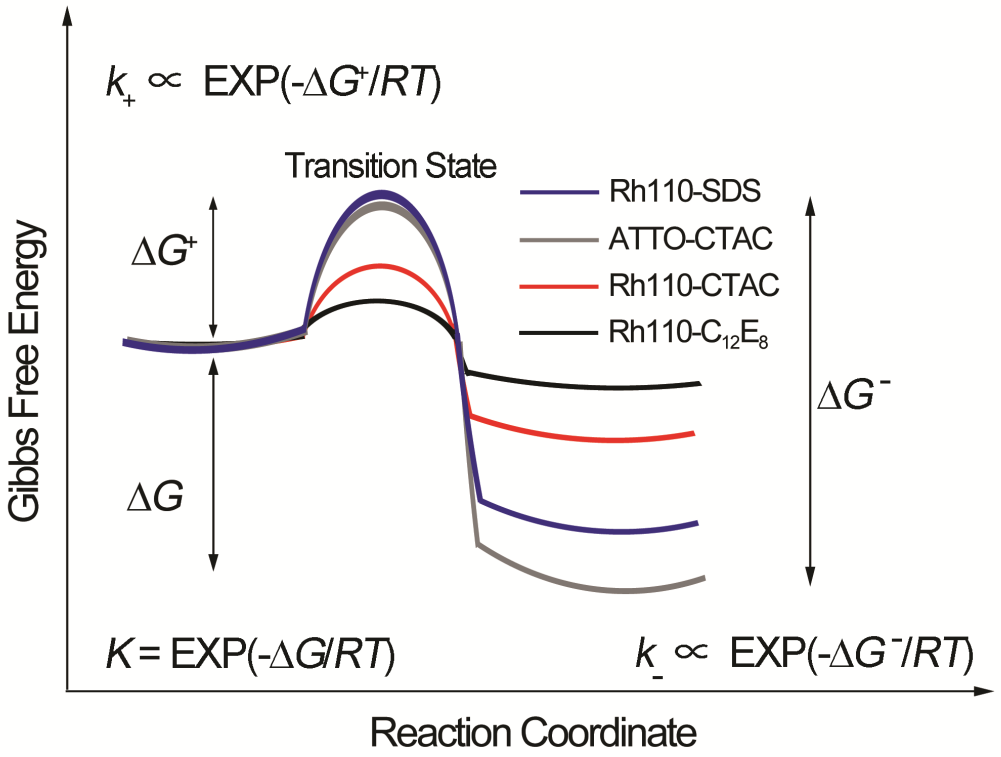

Figure 3.7: A simple scheme of the changes in Gibbs free energy of studied dye-micelle systems due to the complexes formation. Here R_{gc} is the gas constant and T denotes temperature. The equilibrium constant K depends on the free-energy differences (ΔG) of the bound and unbound states. The rate constants (k_+, k_-) depend on the free-energy differences (ΔG^+, ΔG^-) between the two states and the transition state. To simplify the illustration of ΔG, we arbitrarily set the same initial state of each reaction.

The calculated value of k_r was roughly equal to k_+ in our dye-micelle systems, indicating that the complex formation was a reaction-controlled process.

The micelles behaved like "soft cages" which hindered the entrance and exit of dyes when they collided with micelles. The activation energies, labelled with ΔG^+ and ΔG^-, for the studied dye-micelle interactions were shown schematically in Fig. 3.7. In the aspects of thermodynamics we can only determine the Gibbs free energy difference but not the absolute values of them. The free energy differences (ΔG) between the bound and unbound states for various dye-micelle systems were calculated on the basis of the expression: $\Delta G = -R_{gc}T \ln K$, where R_{gc} was the

Table 3.3: Fitted values of the triplet state kinetics: the triplet-state lifetime τ_t and the fraction of dyes in the triplet state p.

	$\tau_t(\mu s)^*$	$p(\%)^*$	$\tau_t(\mu s)^{\#}$	$p(\%)^{\#}$
Rh110-$C_{12}E_8$	2.7 ± 1.3	13.6 ± 4.0	3.3 ± 0.3	14.5 ± 2.1
Rh110-CTAC	3.9 ± 1.0	13.8 ± 3.9	2.3 ± 0.6	7.7 ± 0.8
Rh110-SDS	3.4 ± 1.6	9.7 ± 2.9	2.0 ± 0.6	4.0 ± 0.5
ATTO-CTAC	3.9 ± 1.7	13.6 ± 3.5	5.9 ± 1.4	8.3 ± 0.8

*fitted by Eq. 3.12, # fitted by Eq. 3.7.

gas constant. The energy barriers of intermediate interactions were much lower than those of strong interactions. And the values of the dissociation rate constant for strong interactions were at least one order of magnitude smaller than for the intermediate interactions.

Triplet-state Kinetics

The fractions of dye molecules in the triplet state, p, and the triplet-state lifetime, τ_t, were also obtained from Eq. 3.7 and 3.12. The fitted values of p and τ_t (see Table 3.3) were in line with the published results for rhodamine 110 (1.9 μs, 10%) and ATTO-488 (2.9 μs, 10%) in aqueous media determined by total internal reflection fluorescence correlation spectroscopy (TIR-FCS) [85].

3.3 STED-FCS Section

Due to the diffraction limit, the length-scale of observation volume in standard FCS experiments cannot be reduced below ~200 nm. However, this limitation can be circumvented by means of stimulated emission depletion (STED). STED nanoscopy offers spatial resolution down to ~20 nm by employing a depleting laser beam (shaped into a "donut" with zero intensity at center) coaxial to the excitation beam [33–35]. In principle, the depleting laser suppresses spontaneous fluorescence from the outer part of the confocal volume, trimming the effective observation volume to sub-diffraction size. Combination of STED with

FCS (STED-FCS) allows one to perform experiments at higher probe concentrations and shorter length-scales of observation volume than confocal FCS [36]. This is particularly useful for biological [86–88] and anomalous diffusion investigations [37,89]. A number of such studies have been reported in 2D systems (e.g., lipid membranes) [37–41]. However, few studies using STED-FCS in solutions have been published. This is largely due to troublesome analysis and interpretation of STED-FCS data, related to non-3D-Gaussian observation volume and lack of the analytical form of autocorrelation function for such systems [42–44]. Our recently proposed solution [43], based on realistic description of the 3D observation volume under STED and empirically justified approximation of the ACF, allows us to overcome these issues. Herein, we develop this solution for quantitative studies of diffusion-reaction processes at sub-diffraction length-scales. A unique advantage of STED-FCS for binding/unbinding kinetics studies is direct, gradual control over the size of the observation volume. This allows one to cross in a single experimental system between the large "observation volume" regime, where multiple binding/unbinding acts occur while the probe resides in the observation volume and a single, effective diffusion coefficient is observed, and the "small observation volume" regime, where distinct populations of free and bound probes are observed. In this section, we demonstrate a successful application of STED-FCS to quantification of the equilibrium and rate constants of supramolecular interactions on a simple model of fluorescent dye reversibly binding to surfactant micelles.

Experimental Details

STED-FCS experiments were conducted with MicroTime 200 (PicoQuant, Berlin, Germany) time-resolved fluorescence microscope with a STED add-on and a 100 × /1.4 oil immersion objective (Olympus M Plan Apochromat). The system was equipped with the *easy*STED phase plate set [90] to form a depletion beam in

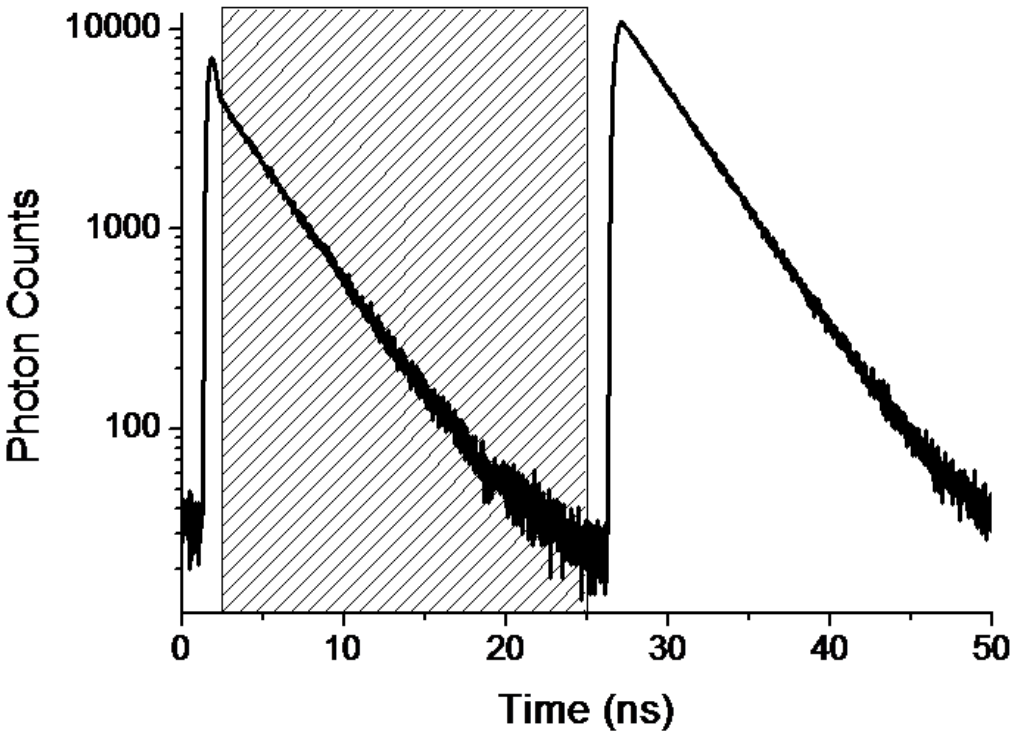

Figure 3.8: Representative Time-Correlated Single Photon Counting (TCSPC) histogram recorded during one STED-FCS measurement ($P_{\mathrm{STED}}/P_{\mathrm{SAT}} = 1.7$) of ATTO647N diffusing in PBS. Both excitation and STED lasers were operated in pulsed mode. The frequency of the STED pulse, 20 MHz, was 1/2 frequency of the excitation one (40 MHz). Therefore, in each cycle STED pulse was introduced in the first section (patterned area) synchronizing with the excitation pulse during $1.7 - 2.2$ ns, while in the second section of the cycle (white background area, after 26.7 ns) only excitation pulse was applied. Photons were assigned to the STED and non-STED sections using time-tagging, which allowed us to record an intrinsic non-STED reference within every measurement. So in one measurement we acquired data in both "confocal" and "confocal+STED" condition, without the need for extra series of measurements.

donut-shape where the intensity of the depleting beam at the center was around 1% of its maximum, while the excitation beam was unaffected. Excitation and depletion lasers (LDH-640 and VisIR 765, PicoQuant) [91] were operated in pulsed mode. To increase the resolution and data quality of STED-FCS, time-gated approach was applied [92–94]. During the time-gated process only photons arriving within a time window at a certain delay T_{g} (2.6 ns) after the excitation pulse were included for data processing.

Both excitation and depletion lasers (LDH-640 and VisIR 765 "STED") were operated in pulsed mode [91]. The repetition rate of the excitation laser was 40 MHz (i.e., one pulse every 25 ns), while the STED laser was operated at half of this frequency. Therefore, STED pulse was introduced after every other excitation pulse, so that an intrinsic, on-line non-STED reference was recorded for every experiment (cf. Fig. 3.8). Each recorded photon was assigned either to the excitation-only or excitation-with-STED pulse. This allowed us to use the ratio of residence times of the probes under STED to the ones under non-STED condition, i.e., $\tau_{\mathrm{STED}}/\tau_{\mathrm{confocal}}$, to describe the changes in apparent diffusion behaviours of the probe as the varying of observation volume, rather than the absolute values of τ_{STED}. Therefore, any errors connected with the non-perfect shape of the beam could be largely cancelled out.

In the STED section of the histogram, the fluorescence decay had another fast component, which mostly originated from the bleed-through of the stimulated emission to the detection channel. Because these photons were from the depleted region (outside the intended observation volume), we disregarded them and only included in the autocorrelation photons recorded between 2.6 and 25 ns (patterned area in Fig. 3.8) to increase the resolution and data quality of STED-FCS. [92–94] Since the delay between pulses was at least three orders of magnitude shorter than the diffusion time, the pulsed mode operation did not influence the autocorrelation in the range of diffusion-related lag times.

Results and Discussion

Depending on the ratio of the average time spent by the dye in the observation volume (determined by the volume size) to the relaxation rate, qualitatively different regimes can be distinguished in terms of autocorrelation data analysis. In the large volume regime, the effective residence time of probes is substantially longer than the relaxation time ($1/R$), namely $\tau_{\Delta} \gg 1/R$. Then, equilibrium is

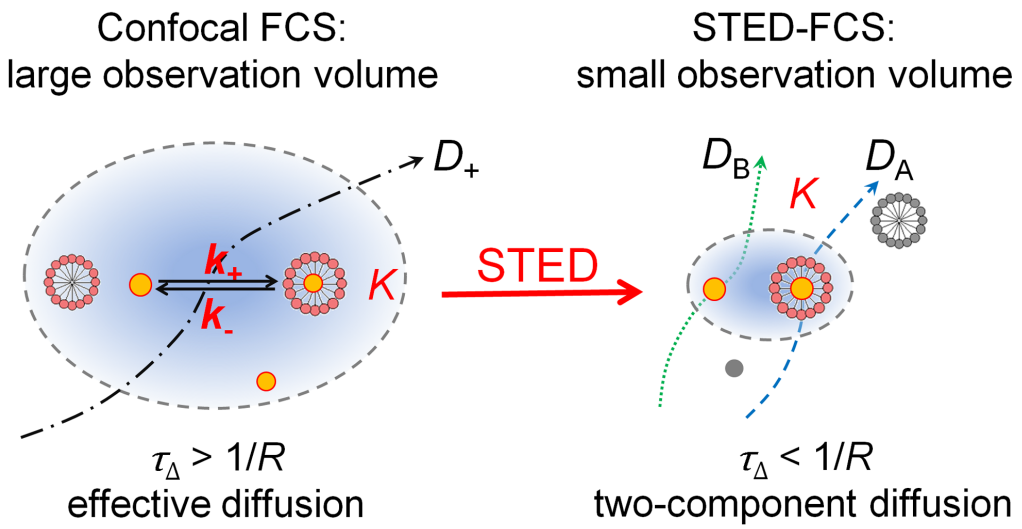

Figure 3.9: Schematic illustration of the complex formation processes in a dye-micelle system within a large and small observation volume of STED-FCS. In the large volume, multiple association/dissociation acts occur during a single passage of the dye through the observation volume, and a single, effective diffusion coefficient is measured. In the small volume, diffusion overruns the reaction, and two distinct components (free dyes and dye-micelle complexes) are observed.

established within the observation volume while the probe is detected. A single, effective diffusion coefficient is obtained, including multiple association/dissociation acts, as well as diffusion of free dyes and dye-micelle complexes in the intervening periods. Contrarily, in the small volume regime, the residence times are shortened and equilibrium is not attained inside the observation volume. There is not enough time for association/dissociation acts to occur before the probe diffuses out of the observation volume (i.e., $\tau_\Delta \ll 1/R$). Hence, motions of dye-micelle complexes and free dyes (D_A and D_B) are recorded separately. In the regime where $\tau_\Delta \approx 1/R$, neither of the two simplifications is valid and the full autocorrelation model including diffusion of the two species as well as the reaction needs to be applied. With a system characterized by an appropriate relaxation rate, it is possible to observe the transition between the aforementioned regimes, simply by controlling the size of the observation volume using STED (see Fig. 3.9).

To allow for quantitative STED-FCS analysis in solutions, we apply the recently developed methodology based on a realistic model of the non-3D-Gaussian

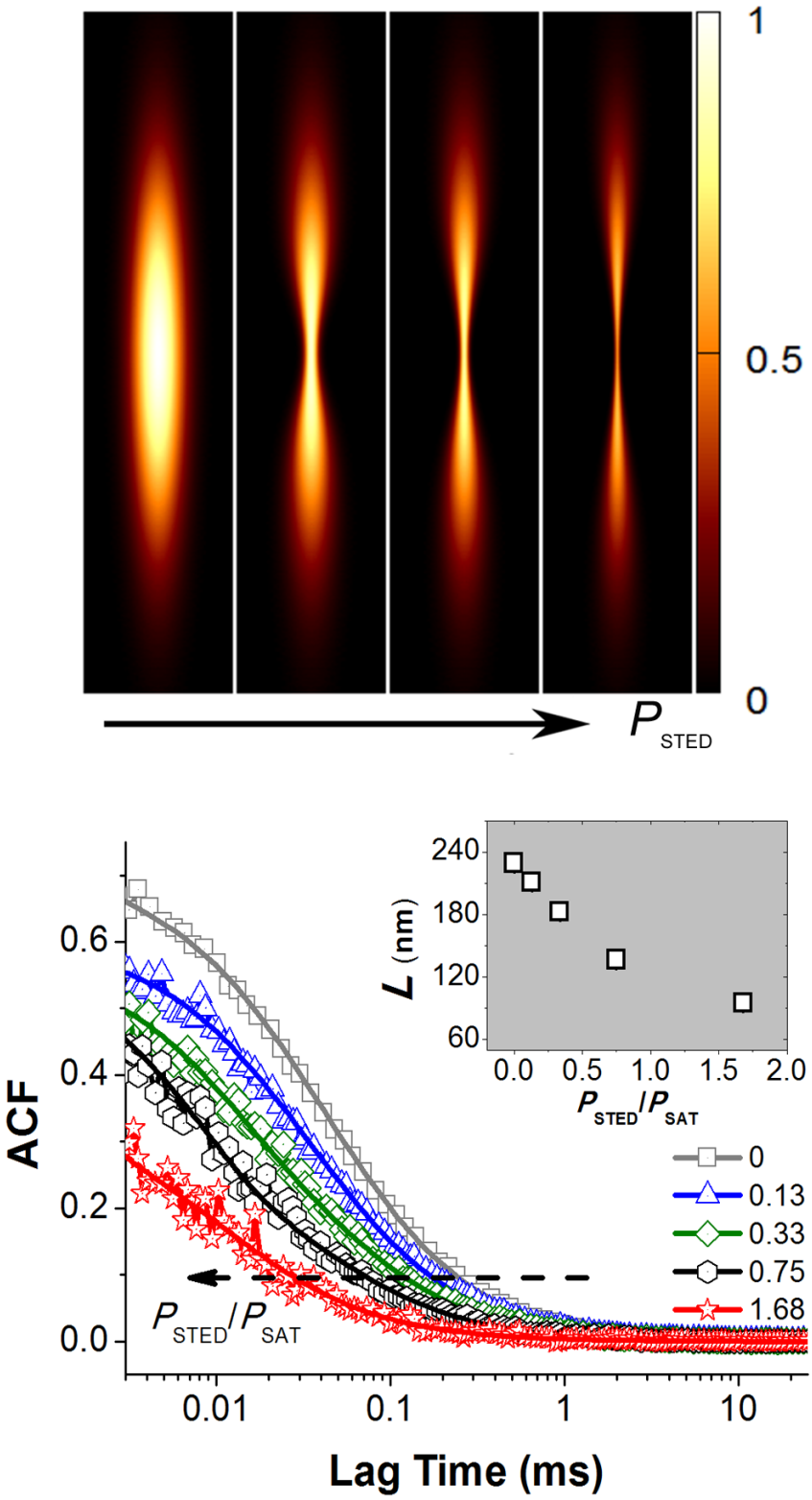

Figure 3.10: Upper panel: representative profiles of effective observation volumes of STED-FCS under various STED powers P_{STED}. For details on the excitation, depletion, and observation profiles see Ref. 43. Low panel: experimental STED-FCS autocorrelation curves for ATTO647N diffusing in PBS (open symbols) under various values of $P_{\mathrm{STED}}/P_{\mathrm{SAT}}$ and the fits using Eq. 1.21 (solid lines). Inset: change in the effective radii of the observation volume with STED power, determined from Eq. 1.19.

shape of observation volume [43]. Briefly, the radial profile of a STED beam is given by a first-order Laguerre-Gaussian function [95, 96]. Its width evolves along the axial direction, causing most efficient depletion at the focal plane and relatively weaker influence on STED at the off-focus regions. This leads to the hourglass-like shape of the observation volume (see Fig. 3.10 upper panel), as well as a decrease in the effective signal-to-noise ratio with increasing STED power due to high contribution of the fluorescence from the dim yet extensive fringes [43]. Still, each radial section of the observation volume retains a Gaussian profile. Due to strong elongation of the effective observation volume, the contribution of axial diffusion of the probes to the autocorrelation function is negligible. These factors justify application of a simple 2D autocorrelation fitting model (cf. Eq. 1.21). This approximation has been validated by computer simulations and a series of experiments with various probes (radii ranging from 0.7 to 6.9 nm) and different medium compositions [42, 43].

Under STED conditions, L of the focus plane decreases with STED power (P_{STED}) as [97,98]: $L = L_0/\sqrt{1 + P_{\mathrm{STED}}/P_{\mathrm{SAT}}}$, where L_0 is the radius of confocal observation volume. P_{SAT} is the saturation power, characteristic for a given fluorophore in given conditions, defined as the STED power at which the overall intensity of spontaneous fluorescence is decreased by half [33, 98]. However, the effective L of STED-FCS in solution corresponds to the radius of the brightest sections of the observation volume and is not equivalent to the detection radius at the focal plane (L ($z = 0$)) due to the axial evolution of the STED profile [43]. Therefore, unlike the experiments in 2D systems [37, 38], L of STED-FCS in solutions cannot be directly obtained from bead scanning experiments. Instead, a series of FCS measurements under various STED power settings for a reference probe with known diffusion coefficient need to be performed to calibrate the dependence of effective L on $P_{\mathrm{STED}}/P_{\mathrm{SAT}}$. The value of P_{SAT} of the reference probe was determined by finding the P_{STED} at which the fluorescence intensity dropped by half. In this work, we used ATTO647N (with determined $P_{\mathrm{SAT}} = 11$ mW)

diffused in phosphate-buffered saline (PBS), taking $D_B = 352\ \mu m^2 s^{-1}$; this value was established in independent FCS measurements at $T = 298\ K$ [99].

As expected, experimental ACFs for ATTO647N in PBS shifted toward shorter lag time region as the STED power increased. The diffusion times were obtained from the fits of the experimental curves using Eq. 1.21. Based on these values, we calculated L using Eq. 1.19. It decreased from 230 nm at $P_{STED} = 0$ to 95 nm at $P_{STED} \approx 1.7 P_{SAT}$ (see the inset of Fig. 3.10). Increasing the STED power even further led to ACFs of poor quality due to low signal-to-noise ratio (SNR) at high STED power [43].

When we measured diffusion of ATTO647N in $C_{12}E_8$ solutions with FCS (at $P_{STED} = 0$), we observed a gradual shift of the autocorrelation curves toward the longer lag time region as the micelle concentration increased (Fig. 3.11). Since the viscosity experienced by ATTO647N in these relatively dilute solutions could be treated as constant and equal to the buffer viscosity [100], we attributed the prolongation of diffusion time to the formation of dye-micelle complexes. All the autocorrelation function curves could be fitted with the simple 3D single-component model for FCS (cf. Eq. 3.12). Since this case fell within the large volume regime ($\tau_\Delta \gg 1/R$), multiple attachment/disattachment acts between the dye and micelles occurred during the probe's residence in the observation volume and averaged out to produce a single, effective value of diffusion time (τ_+). On this basis the effective diffusion coefficient, D_+, was calculated using Eq. 3.8. In the low $C_{12}E_8$ concentration limit, D_+ approached the value characteristic for the dye diffusion in pure buffer. With increasing micelle concentration, D_+ gradually approached the value measured for self-diffusion of $C_{12}E_8$ micelles using dynamic light scattering ($0.34 \times 10^{-10}\ m^2 s^{-1}$, Fig. 3.3)– see the inset of Fig. 3.11. This proved the formation of dye-micelle complexes in the solutions and showed that at high micelle concentrations the dye spent most of the time as a part of the complex (and, rapidly encounters another binding partner after detachment).

The equilibrium constant for the ATTO647N/$C_{12}E_8$ complex formation was

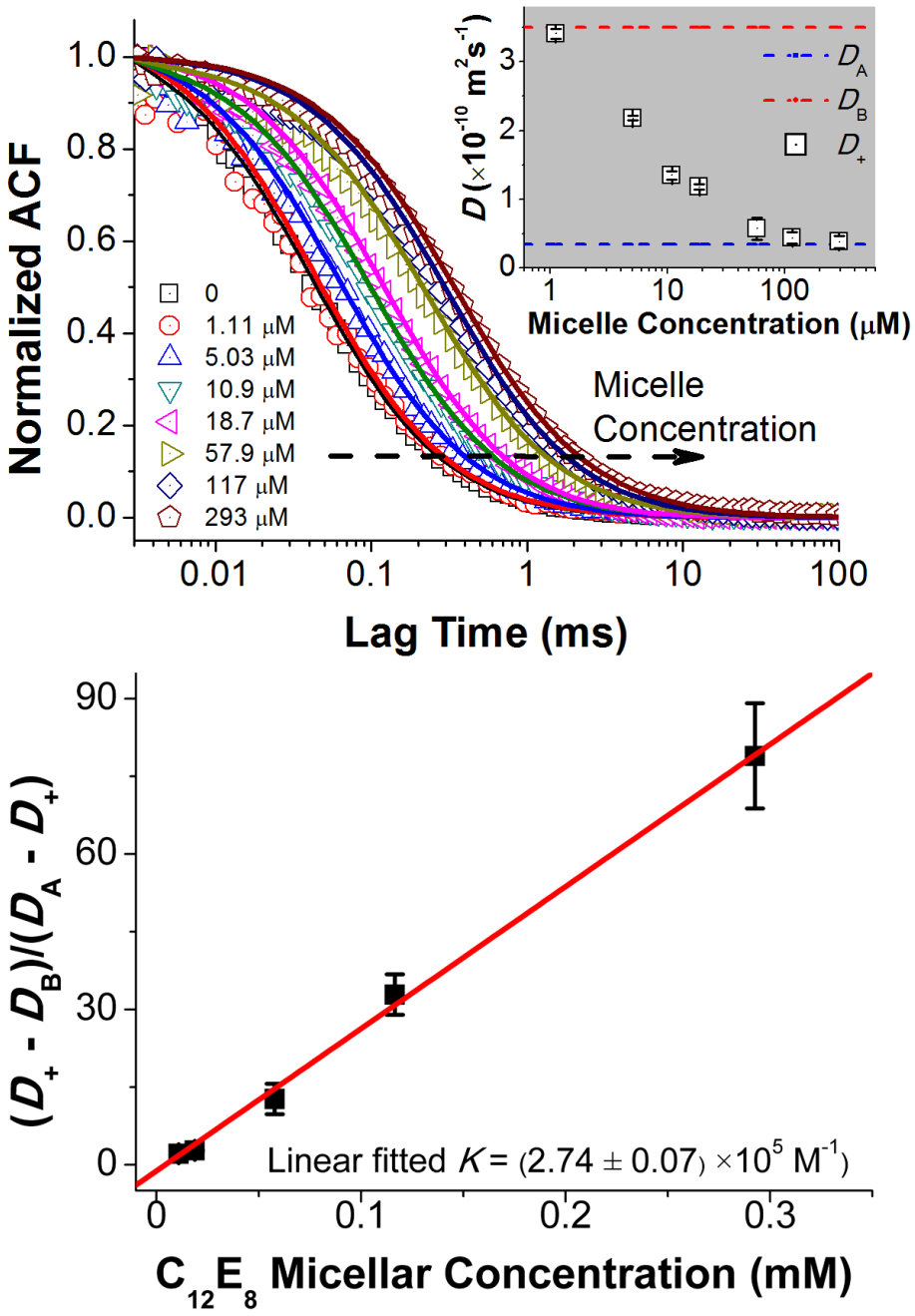

Figure 3.11: Upper panel: normalized experimental autocorrelation curves of ATTO647N in solutions of $C_{12}E_8$ with various concentrations (open symbols) and the fits (solid lines) using Eq. 3.12. Inset: measured diffusion coefficients of ATTO647N (open circle, FCS measurements), $C_{12}E_8$ micelles (open triangle, dynamic light scattering) and effective diffusion coefficients of ATTO647N in $C_{12}E_8$ solutions (D_+, open rectangles). Lower panel: equilibrium constant for ATTO647N/$C_{12}E_8$ complex formation determined from the slope of the linear fitting using Eq. 3.14.

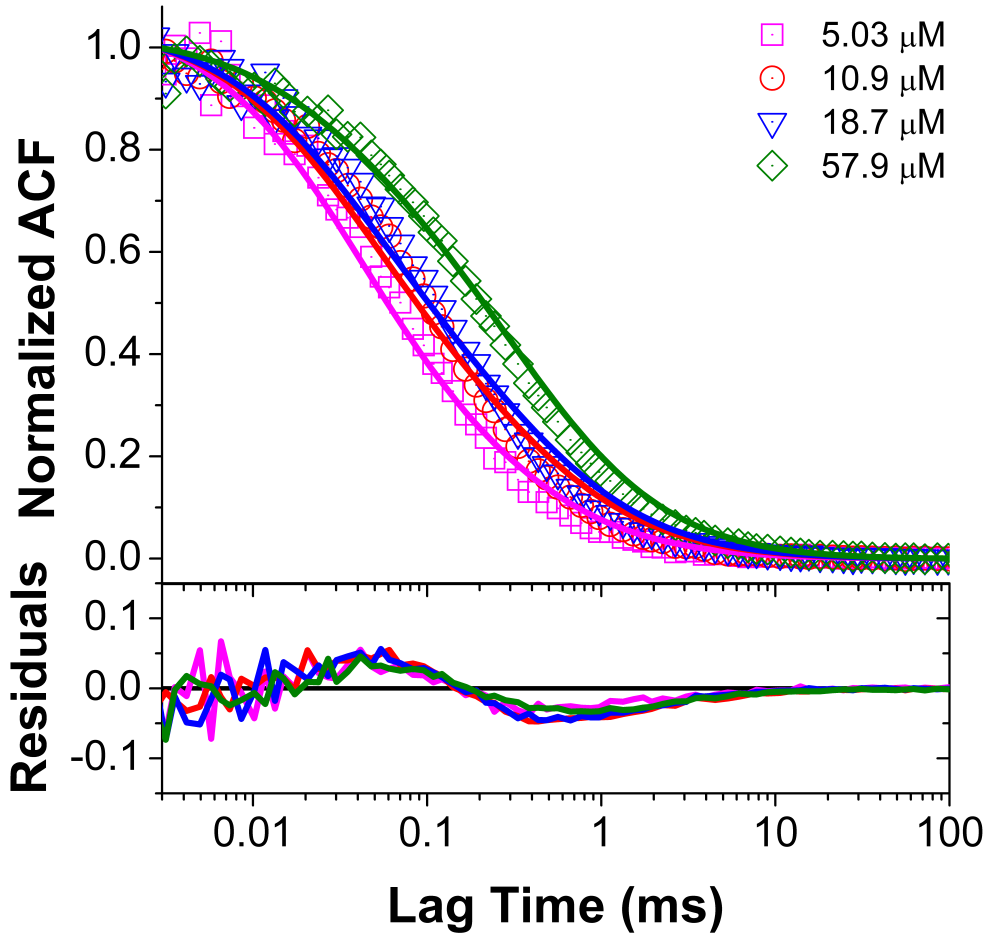

Figure 3.12: Experimental autocorrelation curves of ATTO647N in the $C_{12}E_8$ solutions (open symbols) and the corresponding fits of the 3D, two-component model (Eq. 3.13, solid lines). Apparently, the fits were too poor to rely on due to the large residuals (high systematic errors).

established from the slope of the linear dependence of D_+ on the concentration of micelles $[A]$ (see lower panel of Fig. 3.11), according to Eq. 3.14. The obtained value of $K = 2.74 \times 10^5$ M^{-1} indicated a slightly stronger interaction than the case of $C_{12}E_8$ and rhodamine 110, described in our previous study [31]. This probably resulted from the positive charge of ATTO647N that promoted its electrostatic attraction to the micelle shell.

For comparison, we also tried to fit the experimental autocorrelation curves with the two-component model, which included the contributions of free dye and

dye-micelle complexes separately. Both the diffusion times were fixed on the basis of calibration data. However, the fits were of poor quality, revealing systematic deviations (see Fig. 3.12). This supported the claim that the equilibrium was established within the FCS observation volume in this case, only permitting to observe the effective diffusion rather than the individual contributions of the substrate and the product.

To reach the intermediate range region, where $\tau_\Delta \approx 1/R$, we performed experiments at moderate STED power ($P_{\mathrm{STED}}/P_{\mathrm{SAT}} = 0 - 0.75$) and low micelle concentrations ($1.11 - 10.9$ μM). Autocorrelation curves were fitted using Eq. 3.7. At the lowest concentration of micelles (1.11 μM) we obtained the minimum $R = 17.8$ ms^{-1}, implying that the average time scale of the association/disassociation process (0.056 ms) was already much shorter than the diffusion time of dye-micelle complexes through the non-STED observation volume (0.39 ms) but slower than that of free dyes (0.038 ms). As expected, the relaxation rate of the dye-micelle interaction increased with the micelle concentration: the average distance between the dye and a micelle were shorter so that the diffusive search for another binding partner after detachment from the former one took less time. This led us back to the $\tau_\Delta \gg 1/R$ regime, where the reaction-diffusion model reached its limiting case of single-component model (cf. Eq. 3.12,). Then, only a single, effective diffusion coefficient was observed, which revealed no kinetic information. To keep the full reaction-diffusion autocorrelation model valid at higher micelle concentrations (i.e., to retain the $\tau_\Delta \approx 1/R$ condition), we reduced the diffusion times by means of reducing the observation volume using STED. All the R valued obtained from valid ACF fits using the full reaction-diffusion model were plotted in the inset of Fig. 3.13 as a function of micelle concentration. The association rate constant ($k_+ = 2.95 \pm 0.32 \times 10^9$ M^{-1}s^{-1}) was obtained from the slope of the linear fit using Eq. 3.6. The retrieved k_+ value was roughly one order of magnitude smaller than the diffusion-limited value $k_{\mathrm{dc}} = 2.29 \times 10^{10}$ M^{-1}s^{-1} estimated from the Smoluchowski equation. It also is in line with the results of

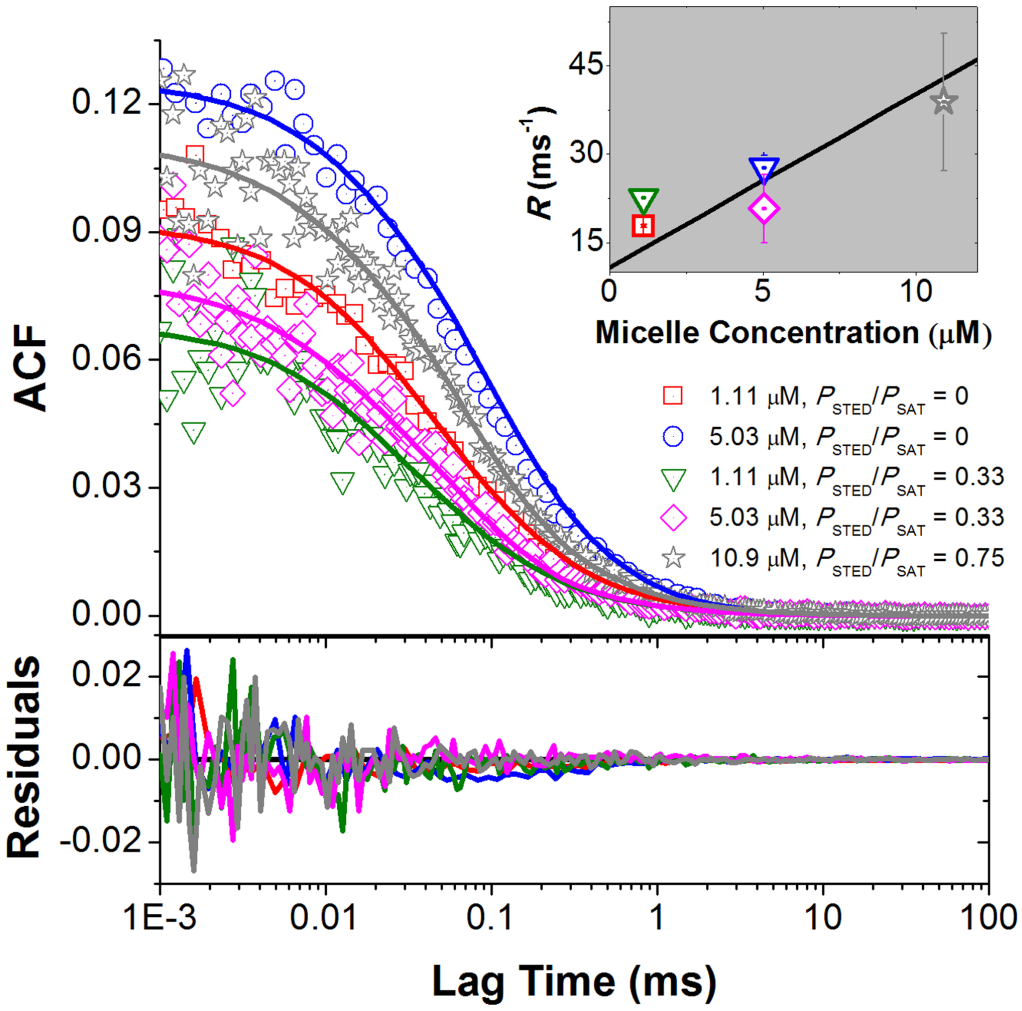

Figure 3.13: Experimental autocorrelation curves of ATTO647N in $C_{12}E_8$ solutions ($1.11 - 10.9$ μM, open symbols) under moderate STED conditions ($P_{\mathrm{STED}}/P_{\mathrm{SAT}} = 0 - 0.75$). The curves were fitted using the reaction-diffusion model of autocorrelation function (Eq. 3.7, solid lines) to obtain the chemical relaxation rates R of the reaction process, plotted as a function of micelle concentration in the inset. The association rate constant $k_+ = 2.95 \times 10^9$ $\mathrm{M^{-1}s^{-1}}$ was obtained from the slope of the fit according to Eq. 3.6 (black line), where K was fixed at the value determined from Eq. 3.14.

previous dye-micelle interaction study.

Stability of the complex is inversely proportional to the disassociation rate constant k_- [101]. k_- can be calculated from the ratio of K to k_+ and for the ATTO647N/$C_{12}E_8$ system equals $1.08 \pm 0.12 \times 10^4$ $\mathrm{s^{-1}}$. The equilibrium and rate constants for ATTO647N/$C_{12}E_8$ determined from our experiments and model are close to the values reported for coumarine 152 and TX100 micelles by Bordello *et*

al [74].

Further increase in the STED power in the dye-micelle systems and corresponding decrease in the diffusion times allowed us to reach the "small volume" regime, where $\tau_\Delta \ll 1/R$. This corresponded to the other limiting case of the autocorrelation model for reaction-diffusion, where diffusion times of all reagents were short enough to be observed irrespective of the attachment/disattachment events – at the time-scale of observation, the reaction could be treated as frozen. Knowing the disassociation rate k_- from the experiments in the reaction-diffusion regime, we estimated the lifetime of the complexes to be ~ 0.1 ms. Taking advantage of STED, we could decrease the diffusion time of the dye-micelle complexes below this critical time-scale.

Therefore, at higher STED power ($P_{\mathrm{STED}}/P_{\mathrm{SAT}} > 0.75$) the appropriate model for ACF analysis is the simple two-component model (cf. Eq. 3.13). Results for ATTO647N diffusion in low-concentration micelle solutions at $P_{\mathrm{STED}}/P_{\mathrm{SAT}} = 1.7$ are presented in Fig. 3.14. The two-component model (with β as the sole fitting parameter, $\tau_{\mathrm{A}} = 66$ μs and $\tau_{\mathrm{B}} = 6$ μs as fixed parameters) provided high quality fits, with no systematic deviations. As expected, the fraction of dye-micelle complexes (β) increased with the micelle concentration. The equilibrium constant $K = 2.14 \times 10^5$ M^{-1}, was determined on this basis as:

$$K[A] = \frac{\beta}{1-\beta}. \tag{3.18}$$

This value is closely comparable to the value determined from the single-component model analysis of the non-STED experiments (2.74×10^5 M^{-1}).

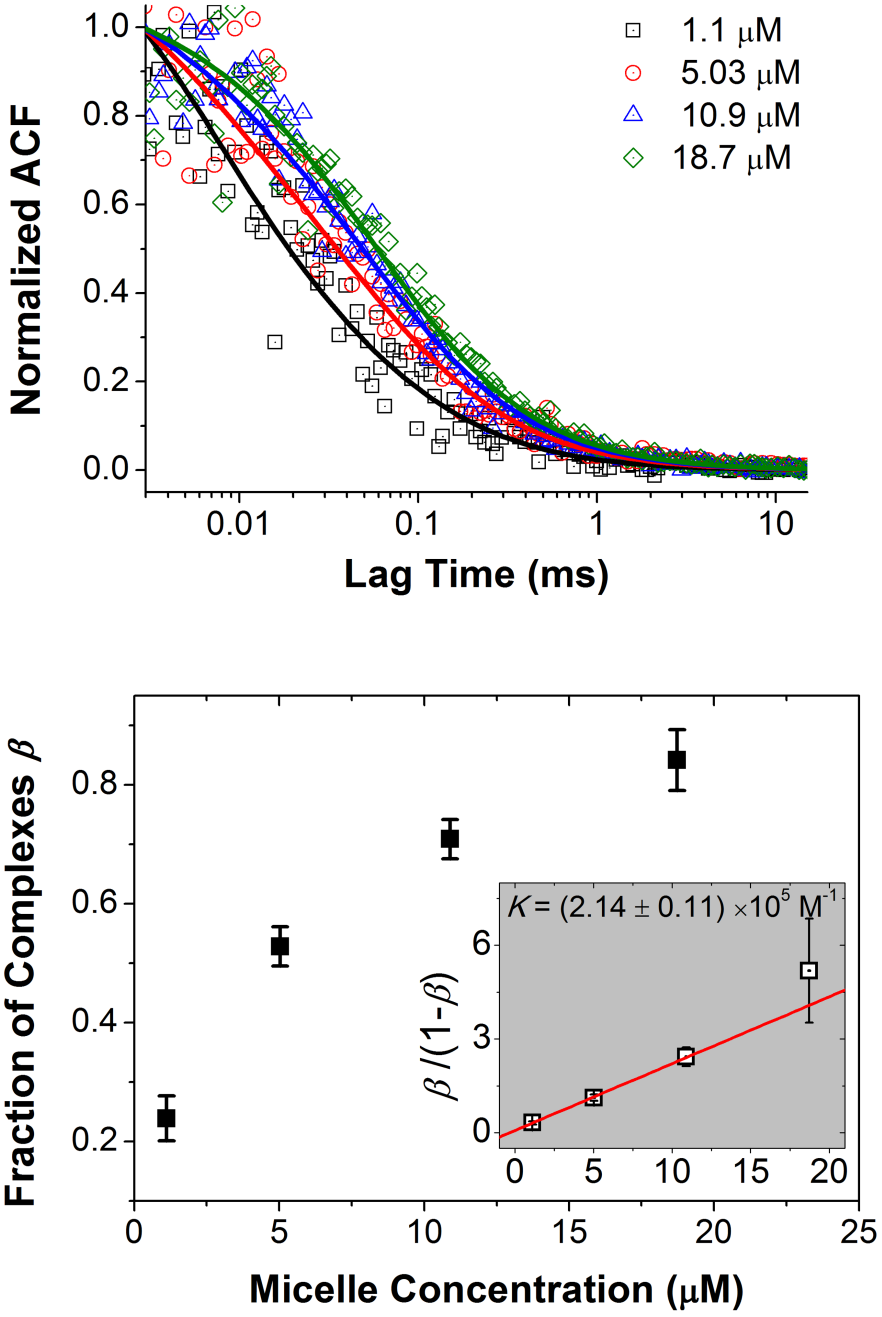

Figure 3.14: Upper panel: experimental (open symbols) and the fitting curves (solid lines) of ATTO647N diffusing in low concentrated $C_{12}E_8$ solutions under high STED power ($P_{\mathrm{STED}}/P_{\mathrm{SAT}} = 1.68$). The two-component model (cf. Eq. 3.13) gave good fits to the experimental curves apparently. Lower panel: fractions of the dye-micelle complexes determined from the two-component model. Inset: equilibrium constant obtained from the slope of the linear fitting from Eq. 3.18.

Chapter 4

DOX-DNA Interactions

Doxorubicin (DOX), sold under the trade name Adriamycin, is a drug widely used for the treatment of various cancers such as leukaemia, lymphoma as well as soft tissue sarcomas [102]. It ranks among the most effective anticancer drugs ever developed. A variety of biochemical evidences suggest that the planar structure of DOX molecule functions primarily by intercalation between the base pairs of double-stranded DNA (dsDNA), anchoring on one side by its sugar moieties that sit in the DNA minor groove (Fig. 4.1), blocking the processes of replication and transcription, and then initiates DNA damages [103].

Despite the extensive usage of DOX in the clinics, the molecular mechanism of drug action leading to cell death is still controversial [104]. What's more, the dose-dependent side effects of DOX on cells and tissues, e.g., cardiotoxicity, extremely reduce its clinical efficacy [102]. Hence, in order to deeply understand the action of DOX on DNA, it is crucial to quantitatively determine the binding affinity of DOX to DNA. This quantity may provide clues for enhancing the anticancerous efficacy of the drug and reducing its side effects to healthy cells and tissues.

Recently considerable number of works focused on the study of mechanism of DOX-DNA interaction using various methods *in vitro*. However, the published values of equilibrium constant determined by those methods such as isothermal titration calorimetry, temperature-jump relaxation measurements, fluorescence

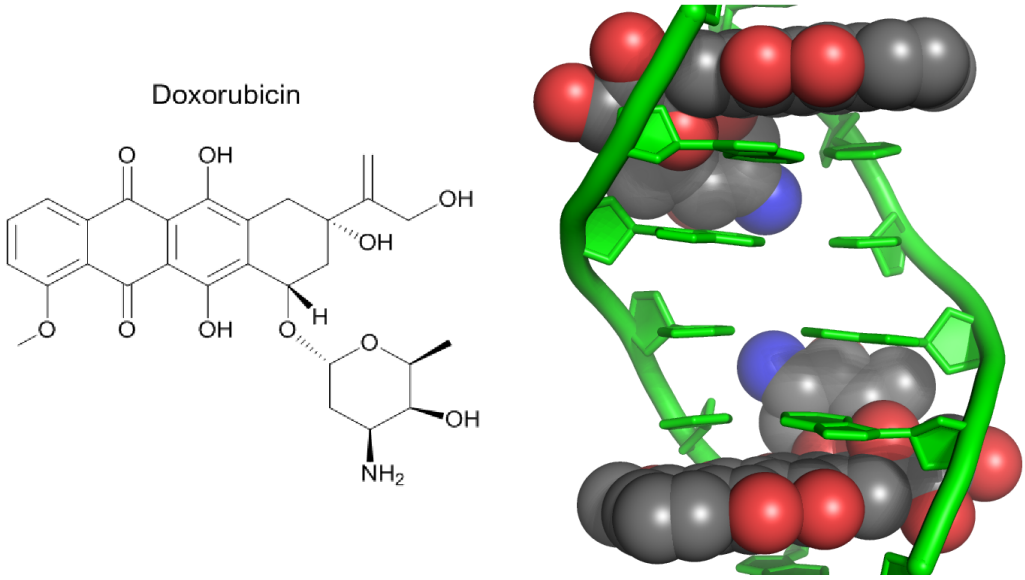

Figure 4.1: Chemical structure of DOX and schematic illistration of intercalation of DOX into a double stranded DNA (in green) by anchoring its sugar moieties into the DNA minor groove.

spectroscopy, etc., are not so consistent with each other (values ranging from 10^4 to 10^8 M^{-1}) [105–111]. Therefore, precise and convenient methods for the investigation of such special intermolecular interaction are still needed. In this chapter we employ FCS as a main tool, supplemented by DLS, to probe the DOX-DNA interaction *in vitro* at single-molecule level. Equilibrium constant and its temperature-dependence of the DOX-DNA interaction were determined. Additionally, we also revealed the influence of an important cross-linker widely presented in cells, formaldehyde, on the formation of DOX-DNA complexes.

4.1 Materials and Methods

Doxorubicin (purity: $>$ 99%) was purchased from BIOTANG Inc. Formaldehyde solution (36-38%, chemically pure) was bought from Chempur. Calf thymus DNA (ctDNA, 42% in GC base pairs) was purchased from Merck. Plasmid DNA (pUC19, 51% in GC base pairs) was purchased from Thermo Fisher Scientific in vials of 10 units (1 unit is defined as the DNA sample that yields an absorbance

of 1.0 at 260 nm in 1.0 mL of water in a 1.0 cm optical path cuvette). All DNA samples were dissolved in the Tris-HCl solutions (pH 7.4, I = 10 mM). The concentrations of both DNAs, expressed as the molarity of base pairs (the average molecular weight of one base pair was set at 650 Da), were confirmed by absorbance measurements at 260 nm. FCS and DLS measurements were performed with the same setup and settings described in former chapters, if not otherwise specified.

4.2 Results and Discussion

Formation of DOX-DNA Complexes

We recorded the diffusion of rhodamine 110 and DOX in the solutions of pUC19 and ctDNA by FCS separately. In the case of rhodamine 110 diffusing in the two DNA solutions, no interaction was observed from all the overlapped ACFs of rhodamine 110 in various concentrations of DNA solutions (see Fig. 4.2). In contrast, we clearly saw the presence of second components from the long lag-time region of the ACFs in the cases of DOX. We inferred the second-component originated from the formation of DOX-DNA complexes, considering that the diffusion of DNA was much slower than that of free DOX.

We attempted to fit the experimental curves with the single-component model (Eq. 3.12), however, the fit was too poor according to the large residuals (see Fig. 4.3). We also tried to fit the curves with the full model for FCS (i.e., Eq. 3.7). The fitting procedure was the same as that in the dye/micelles cases, where the relaxation rate R was the only fitting parameter. The fitted values of R were around 0 in both DNA cases, demonstrating two-component diffusion (DOX and DOX-DNA complex) in the systems. This was in line with the expectation: since the concentration of DOX (1 nM) was much higher than those of DNAs (to sub-nanomole) but much lower than those of base pairs (from μM to mM), there

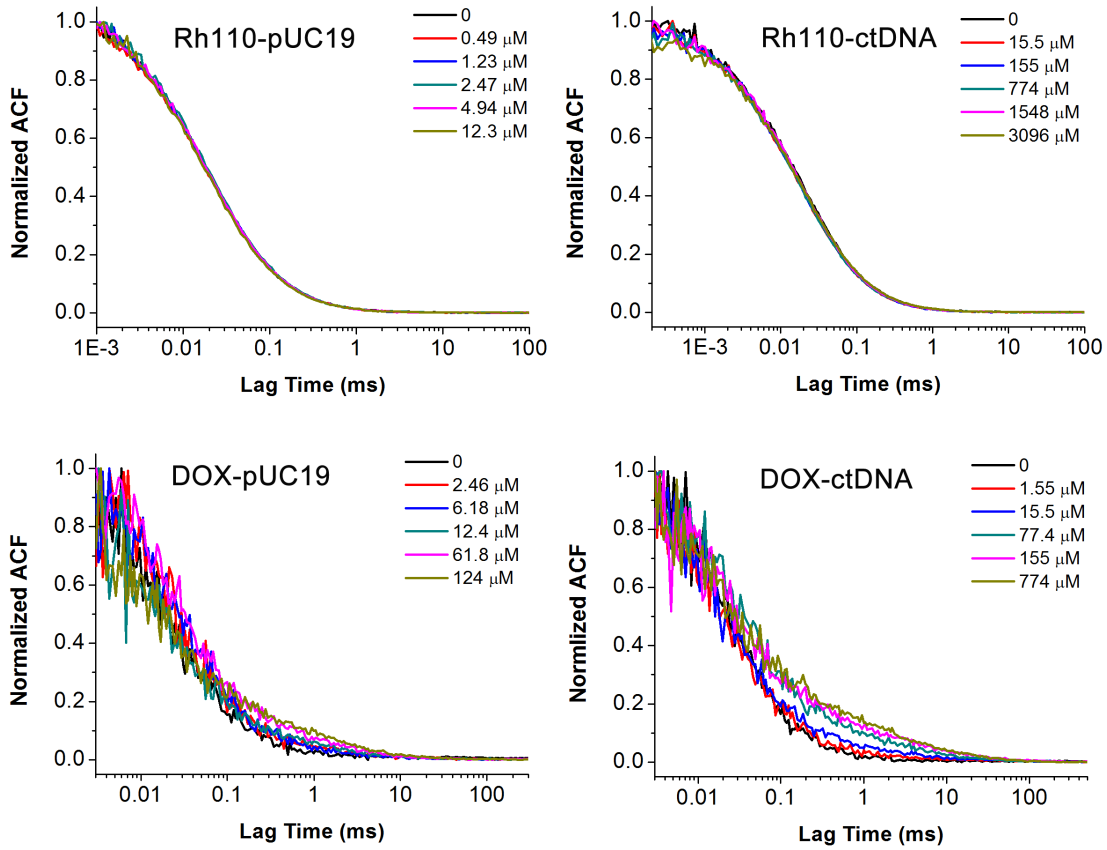

Figure 4.2: Normalized experimental ACFs of rhodamine 110 and DOX diffusing in the solutions of pUC19 and ctDNA with various concentrations respectively. The overlapped curves of rhodamine 110 in both DNA solutions suggested no interaction between them, while apparent interactions between DOX and the two DNAs were observed from the gradual shifts of ACFs as a function of DNA concentration.

were always free DOX and DOX-DNA complexes presenting in the focal volume. Therefore, it was justified to fit experimental curves with the two-component model (Eq. 3.13), in which β was the only fitting parameter. Other parameters such as the diffusion coefficients of DOX and DNA were known form calibration experiment and DLS measurements separately.

We measured the diffusion coefficient of ctDNA in Tris-HCl buffer (pH 7.4, I = 10 mM) at 25 ℃ using DLS. The determined self-diffusion coefficient of the ctDNA was 1.95×10^{-12} m^{2}s^{-1} (see Fig. 4.4), consistent with the published values (1.9×10^{-12} m^{2}s^{-1}) [112]. The diffusion coefficient of pUC19 was taken from the

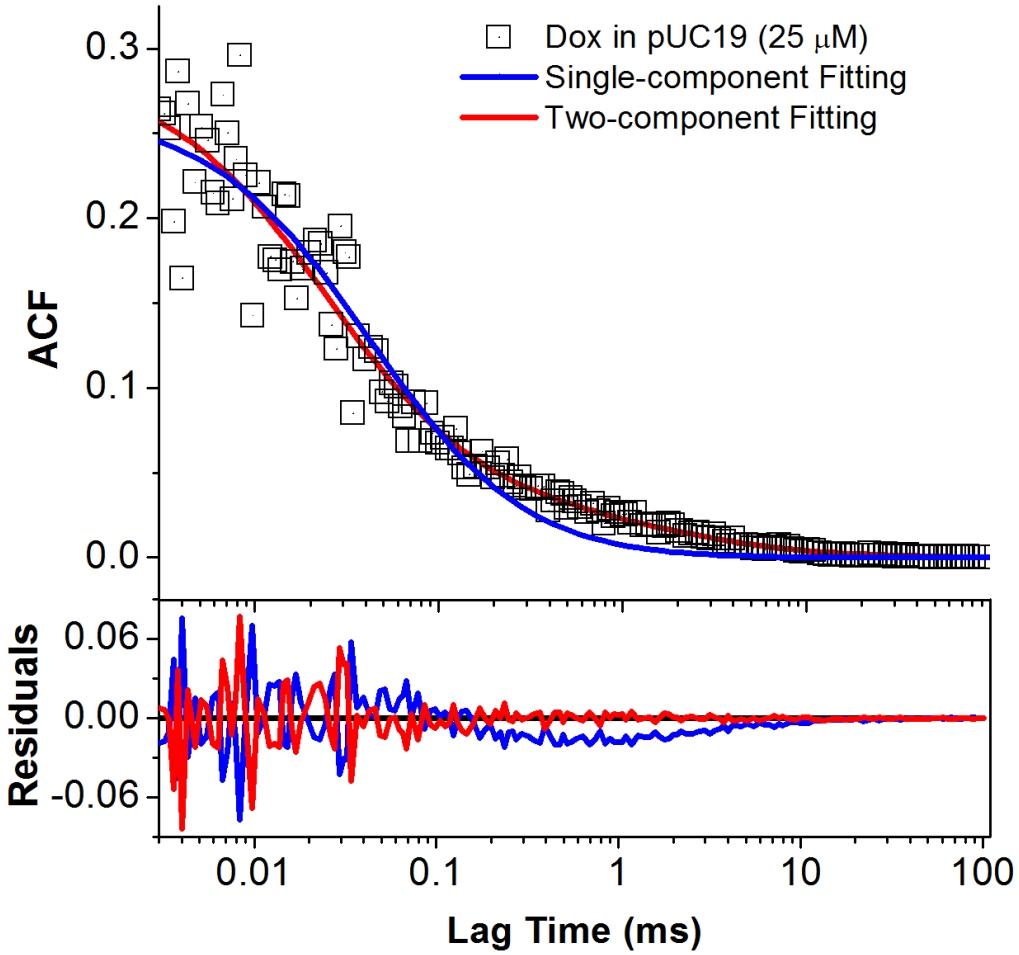

Figure 4.3: Example curves of DOX in pUC19 solution (base pair concentration: 25 μM). Two-component model gave good fit while the single-component model could not, as the residuals showed. We also observed the similar fitting profiles of the two models for other concentrations of DNA.

published value of 5.6×10^{-12} [113], since its concentration was too low for DLS to measure.

Equilibrium Constant of DOX-DNA Interaction

The two-component model allows us to determine the equilibrium constant of DOX-DNA interactions based on the relation between K and β (cf. Eq. 3.18). We fitted the experimental curves of DOX in the pUC19 and ctDNA solutions with the two-component model (Eq. 3.13) and then obtained the fractions of free DOX (1-β) and DOX-DNA complexes (β) in the solutions. As the DNA

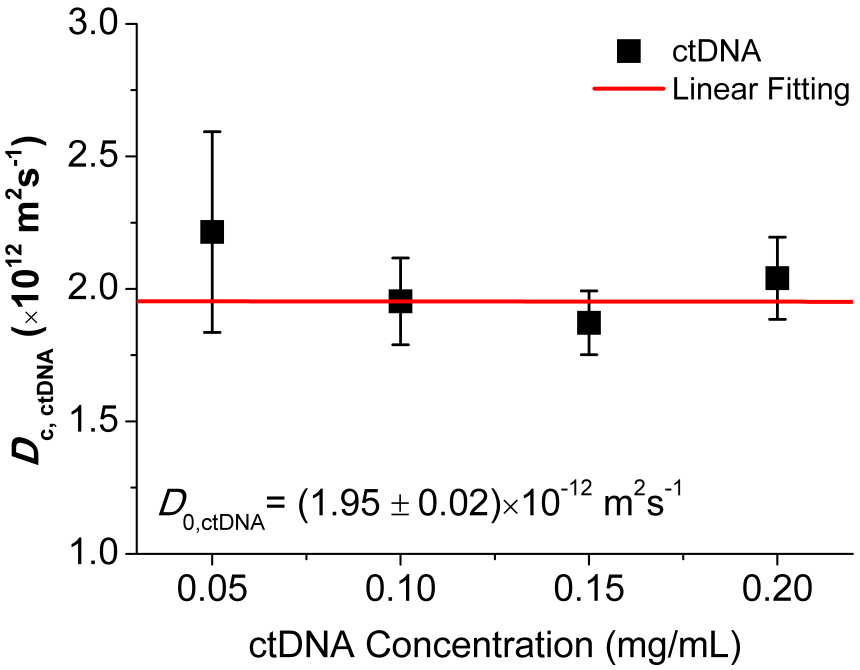

Figure 4.4: Linear fit of the collective diffusion coefficients of ctDNA in Tris-HCl buffer via Eq. 1.30. Extrapolation the concentration to infinite dilution gave the self-diffusion coefficient of ctDNA.

concentration increased, more and more DOX-DNA complexes were formed until the saturation of DNA was reached (see Fig. 4.5).

The equilibrium constant K of DOX-DNA interaction were determined from its dependence on the β as a function of molar concentration of base pair using Eq. 3.18. The fitted value of K was 3.3×10^3 M^{-1} for the DOX-pUC19 interaction and 1.5×10^3 M^{-1} for the DOX-ctDNA system at 25 ℃ respectively (see the inset of Fig. 4.5). These values were close to the reported equilibrium constants for the outside binding of DOX to the minor grooves of ctDNA ($\sim 3 \times 10^3$ M^{-1}) [106,110]. The outside binding was driven by the electrostatic attraction between the positively charged amino group in the sugar moiety of DOX and the negative charged phosphate groups of DNA. It was also confirmed by spectroscopic experiments and computer simulations [114–116].

The kinetic mechanism of DOX-DNA interaction was described by a 5-step

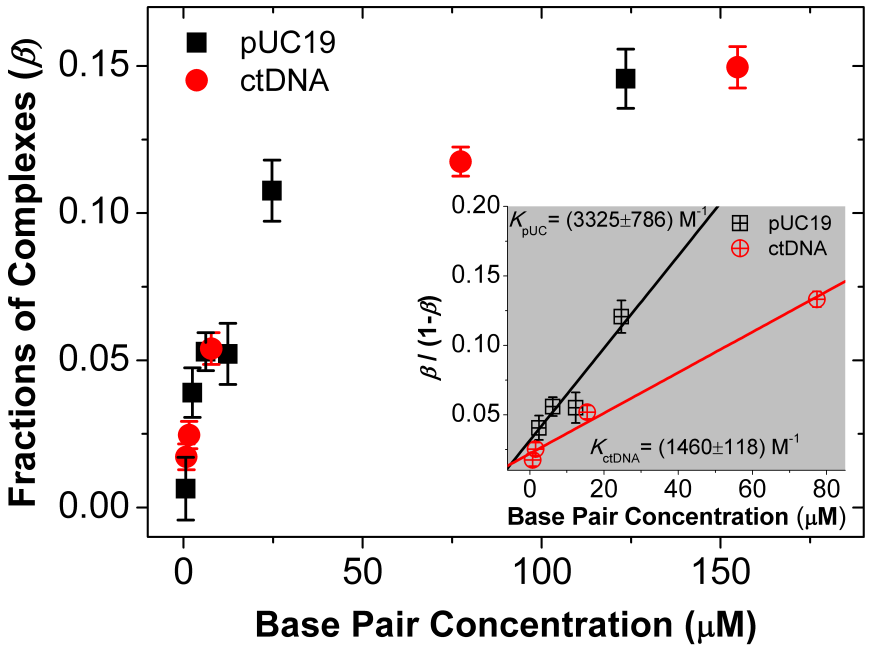

Figure 4.5: Fractions of DOX-DNA complexes determined by the two-component model for FCS in various concentrations of pUC19 and ctDNA solutions at 25 ℃. Insert: The equilibrium constants K of the interaction between DOX and the two DNA determined from the linear fits using Eq. 3.18.

reversible reactions [110, 115], in which the outside binding was assigned to the first one. The outside binding took place when the concentration ratio of DOX to DNA base pairs was very low (< 0.1) [106]. This condition was in line with our FCS experiments where the concentration of DOX was always much lower than those of base pairs. As a result, the equilibrium constant we obtained from FCS corresponded to the outside binding between DOX and DNA. Further increase of DOX concentration could cause the intercalation of the drug into the double strands of DNA, which was reported previously. However, this could not be fulfilled by FCS due to the requirement of nanomolar concentration of the probes in FCS experiments.

Next, we investigated the influence of temperature on the equilibrium constant for the outside binding of DOX to DNA in other two temperatures, i.e., 30 ℃ and 36 ℃ (Fig. 4.6). In both cases we found the outside binding were exothermic:

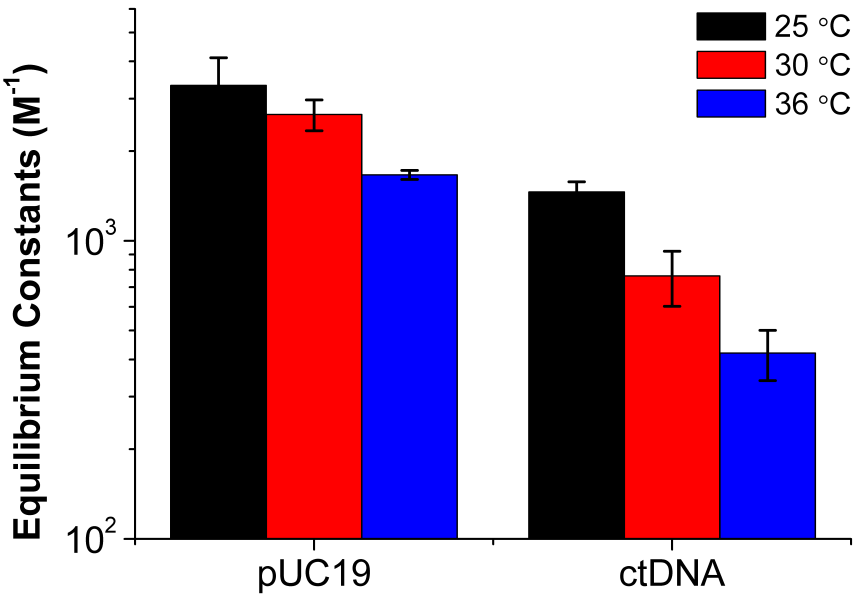

Figure 4.6: Determined equilibrium constants K of DOX-DNA interactions in the temperatures of 25, 30, 36 ℃. In both DNA cases the equilibrium constants decreased as the increase of temperature.

Higher temperature favoured the backward reaction and therefore reduced the stability of the complexes. This exothermic property of DOX-DNA interaction was also reported in other drug/DNA systems [117, 118].

Influence of Exogenous Formaldehyde

Formaldehyde, the simplest aldehyde usually known as an environment pollutant, possesses high reactivity toward cellular macromolecules such as DNA and proteins in human body by enzyme-catalysed reactions [119, 120]. Formaldehyde is produced from a range of carbon sources (e.g., lipids and spermine) by iron-mediated free radical reactions in cells [121, 122]. The interaction between DOX and DNA could be enhanced by the formation of covalent bond in the presence of formaldehyde: formaldehyde reacts with the amino group of the DOX to form a reactive Schiff base and then it links to one strand of DNA [123–125]. The

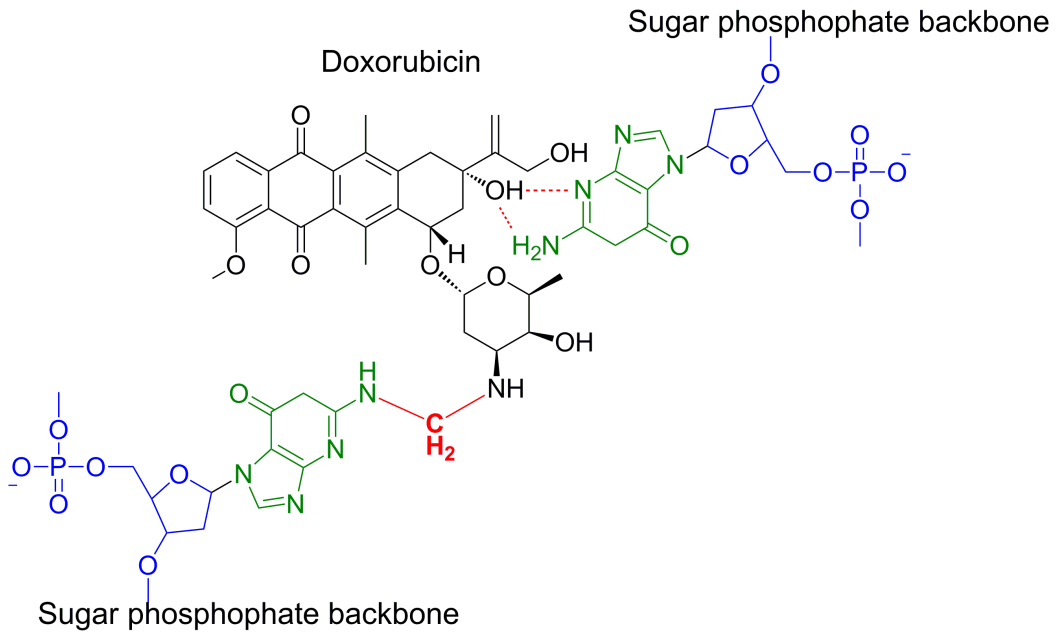

Figure 4.7: Exemplary structure of the DOX-DNA compounds in the presence of formaldehyde. The covalent bonds (shown in red) between DOX and one guanine moiety of one strand of DNA is mediated by formaldehyde. Additionally, the compounds is further stabilized by the extra hydrogen bonding between DOX and the other guanine moiety of the complementary strand of DNA.

compounds are further stabilized by the additional hydrogen bonding between DOX and the second strand of DNA (Fig. 4.7). Interestingly, higher amount of formaldehyde have been detected in the tumour cells than in the normal cells [126, 127]. Therefore, higher efficacy of drug in the tumour cells is observed with the help of formaldehyde.

To study the influence of formaldehyde on the formation of DOX-DNA compounds, we recorded the diffusion of DOX in the two DNA solutions in the presence of formaldehyde (2%, w/w). As expected, we started to see the second component appearing from the autocorrelation curves at the much lower concentrations of DNA (cf. Fig. 4.8) compared to the ones in the absence of formaldehyde. The presence of formaldehyde promoted the formation and stability of DOX-DNA compounds via covalent and hydrogen bonding [102, 104, 128].

Other possible side-products besides the DOX-DNA compounds may be produced during the reaction. For example, formaldehyde can cross-link two DOX

monomers to produce a dimer. However, this side-reaction does not affect our FCS curves. This is because on one hand the dimer can not further bind to the strands of DNA via the covalent bonding in the presence of formaldehyde since there is no more free amino group to react. One the other hand, the quantum yields of the DOX dimer is three orders of magnitude lower than that of the monomer (0.039) [129]. Therefore, the DOX dimer can be treated as non-fluorescent molecule.

Besides promoting the formation of DOX dimers, formaldehyde may cross-link the two strands of two DNA molecules via the aforementioned mechanism. However, this reaction takes from dozens of hours to days to reach the equilibrium, which is several orders of magnitude slower than the formation of DOX-DNA compounds [125, 130–132]. Therefore, in the presence of formaldehyde only the signals from DOX monomers and DOX-DNA compounds contribute to the ACFs of FCS. No signal originates from the side-products in the FCS experiments.

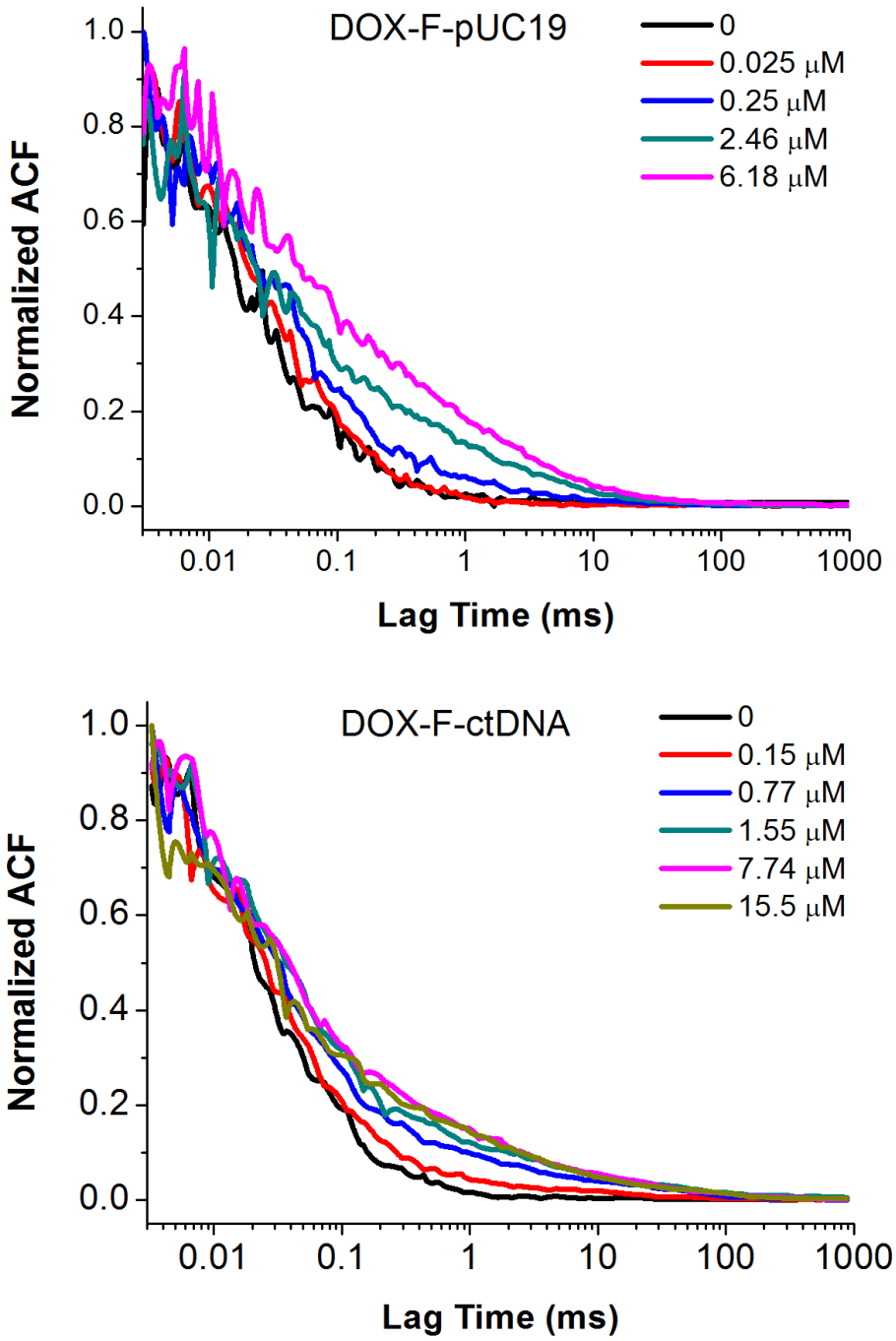

Figure 4.8: Normalized experimental autocorrelation curves of DOX diffusing in the solutions of pUC19 and ctDNA in the presence of formaldehyde. Higher fractions of DOX-DNA compounds were observed at much lower concentrations of DNA (to be compared with Fig. 4.2).

Chapter 5

Summary and Conclusions

Quantitative determination of intermolecular interactions is of great interest and crucial in the fields of chemistry, biology, and physics. [41, 133, 134]. The conventional ensemble experiments, e.g., titration or NMR, were only able to provide the averaged characteristics of intermolecular interaction, while the individual behaviours of each component in the processes of interaction were partially hidden. Within this thesis I quantitatively determine the intermolecular interactions from the motion of various probes in aqueous solutions at the single-molecule level. Fluorescence correlation spectroscopy (FCS), stimulated emission depletion-FCS (STED-FCS), and other auxiliary methods such as dynamic lighting scattering (DLS), Taylor dispersion analysis (TDA), etc., were employed as main tools. The summaries and conclusions of each chapter within the thesis are listed below.

- **Protein/Surfactant Interactions** We investigated the diffusional and structural properties of BSA in four surfactant solutions ($C_{12}E_5$, $C_{12}E_8$, CTAC and SDS) using FCS. We observed the structural transitions of BSA in the diluted ionic surfactant solutions of SDS and CTAC (far below their CMC). The calculated hydrodynamic radius of BSA increased from 3.9 to 6.2 and 6.5 nm in SDS and CTAC solutions respectively. In contrast, the globular BSA did not change its size in the nonionic surfactant solutions of $C_{12}E_5$ or $C_{12}E_8$ at all.

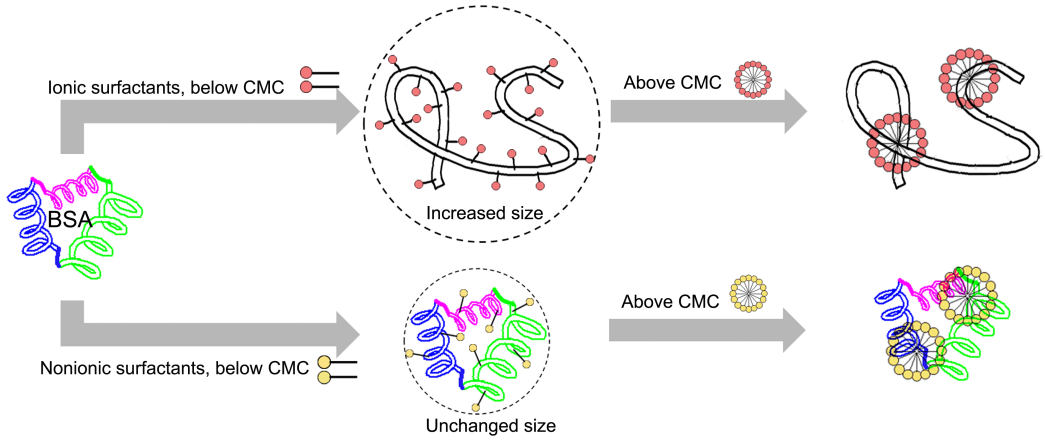

Figure 5.1: Suggested mechanism of the structural changes of BSA (unfolding) in ionic surfactant solutions at the concentration below and above CMC.

We confirmed the structural transition of BSA from the fluorescence lifetime analysis. The lifetime of ATTO-488 labelled to BSA increased suddenly from 2.36 ns (in water) to 3.02 ns (in SDS solutions) and to 2.84 ns (in CTAC solutions) due to the structural transition of BSA. However, no change in the fluorescence lifetime was observed in nonionic surfactant solutions. Additionally, the structural transition of BSA took place in the highly diluted ionic surfactant solutions (far below their CMC). Thus we inferred that the structural transition of BSA had been induced by surfactant monomers before the formation of micelles (see Fig. 5.1).

- **Dye/Micelle Interactions** We quantitatively determined the equilibrium and rate constants of complex-formation in dye-micelle systems using FCS and STED-FCS separately. In the FCS section, we categorized the dye-micelle interactions into three types: weak, intermediate and strong, according to the determined values of the equilibrium constant K. The values of K determined from FCS were consistent with those from the other independent experiments, i.e., TDA as well as those from literatures. To obtain the association/dissociation rate constants we fitted experimental data with the full model for the autocorrelation function of FCS ($G_a(t)$, see Eq. 3.7)

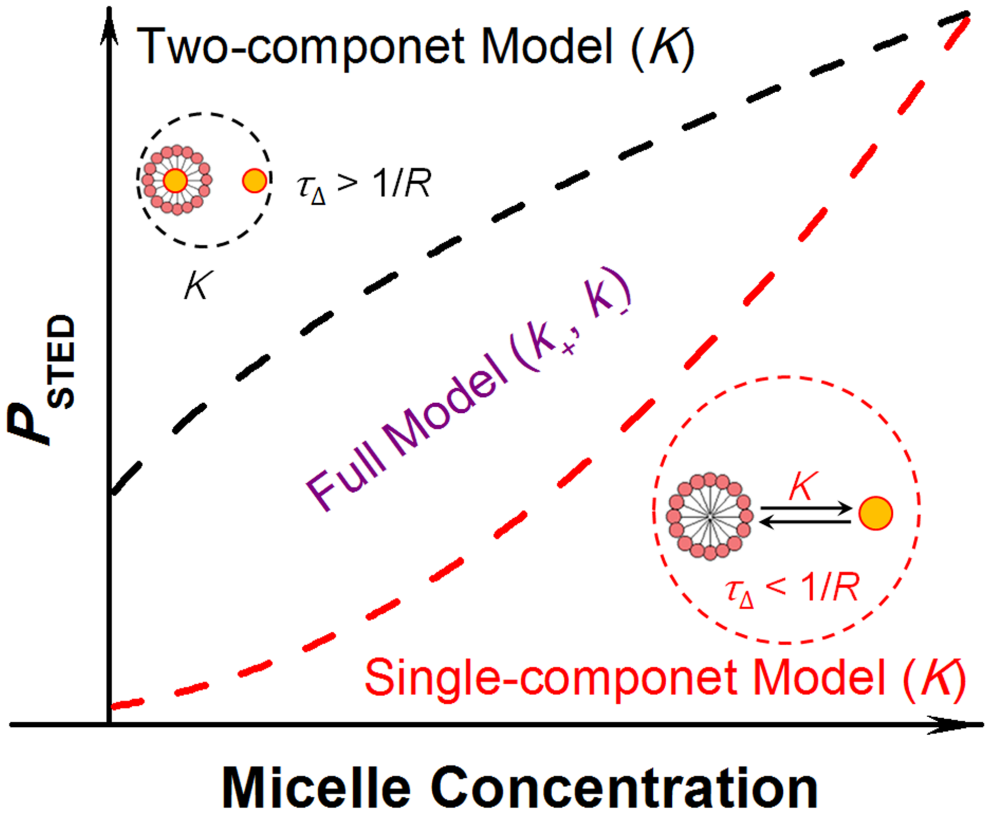

Figure 5.2: Illustration of the applicability of each model for the autocorrelation function in a diffusion-reaction system in STED-FCS. The single-component model (Eq. 3.12) is suitable for studies in the relatively concentrated solutions, while the two-component model (Eq. 3.13) is the limiting case, relevant to slow reaction and small observation volume. The equilibrium constant of the reaction can be determined in any of the cases. The full reaction-diffusion model (Eq. 3.7) can be applied to the systems falling between the two limiting cases (i.e. when $\tau_\Delta \approx 1/R$), allowing to retrieve information on the rate constants of complex formation.

derived on the basis of Magde's formula. Our results showed that the association rates of the dye-micelle interactions were much smaller than the diffusion-controlled rate. Therefore, a two-step reaction mechanism was used to explain the complex-formation between dyes and micelles.

In the STED-FCS section, we provided a full analytical model for the autocorrelation function of FCS in a reaction-diffusion system upon STED conditions. Altering the size of observation volume, we were able to observe both limiting cases of the model (cf. Fig.5.2): where a single, effective dif-

fusion time was observed (equilibrium establishes within the time-scale of observation), and where separated contributions from free and bound dyes were observed (reaction slower than the time-scale of diffusion). The values of equilibrium constant determined for the ATTO647N/$C_{12}E_8$ system in the two limiting cases were in reasonable agreement with each other. The association/dissociation rate constants were obtained from analysis of the experiments in the $\tau_\Delta \approx 1/R$ regime based on the full reaction-diffusion model of ACF Eq. 3.7. By demonstrating the applicability of STED to enhance the capabilities of FCS in the kinetic studies, we showed a promising perspective of STED-FCS towards the analysis of intermolecular interaction in simple solutions as well as biomimetic and biological complex systems.

- **DOX/DNA Interactions** Based on the former studies of dye-micelle interaction using FCS, we applied our method to a practical case of intermolecular interaction in the field of biochemistry: anticancer drug DOX and DNA. We quantitatively determined the equilibrium constants of DOX-DNA interaction by using the two-component model for FCS (Eq. 3.13). The determined K from our method were close to the published values corresponding to the outside binding of DOX to the minor grooves of DNA. Besides, the influence of temperature on the equilibrium constant of the DOX-DNA interaction *in vitro* was investigated. Our results showed that the outside binding was an exothermic process: the higher reaction temperatures, the lower values of equilibrium constants.

  Next we studied the influence of formaldehyde, which could cross-link the DOX and DNA molecules via covalent bonds, on the formation of DOX-DNA compounds. We observed DOX-DNA compounds were produced at much lower concentrations of DNA, compared to the concentration at which the noncovalent bounded DOX-DNA complexes formed in the absence of formaldehyde. This result supports the action mechanism of DOX in the

cancer cell where the concentration of formaldehyde is much higher than that of normal ones.

Bibliography

[1] Johannes Diderik Van der Waals. Over de continuiteit van den gas-en vloeistoftoestand. 1, 1873.

[2] Charalampos G Kalodimos, Nikolaos Biris, Alexandre MJJ Bonvin, Marc M Levandoski, Marc Guennuegues, Rolf Boelens, and Robert Kaptein. Structure and flexibility adaptation in nonspecific and specific protein-dna complexes. *Science*, 305(5682):386–389, 2004.

[3] Eric V Anslyn and Dennis A Dougherty. *Modern physical organic chemistry*. University Science Books, 2006.

[4] Harvey Lodish, Arnold Berk, S Lawrence Zipursky, Paul Matsudaira, David Baltimore, James Darnell, et al. *Molecular cell biology*, volume 3. Scientific American Books New York, 1995.

[5] Fritz London. The general theory of molecular forces. *Transactions of the Faraday Society*, 33:8b–26, 1937.

[6] Alan R Fersht, JP Shi, J Knill-Jones, DM Lowe, AJ Wilkinson, DM Blow, P Brick, P Carter, MMY Waye, and G Winter. Hydrogen bonding and biological specificity analysed by protein engineering. *Nature (London)*, 314:235–238, 1985.

[7] Ken A Dill. Dominant forces in protein folding. *Biochemistry*, 29(31):7133–7155, 1990.

[8] Xuzhu Zhang, Andrzej Poniewierski, Sen Hou, Krzysztof Sozański, Agnieszka Wisniewska, Stefan A Wieczorek, Tomasz Kalwarczyk, Lili Sun, and Robert Hołyst. Tracking structural transitions of bovine serum albumin in surfactant solutions by fluorescence correlation spectroscopy and fluorescence lifetime analysis. *Soft matter*, 11(12):2512–2518, 2015.

[9] AL Buchachenko, AM Wasserman, and AL Kovarskii. Kinetics of molecular motions in liquids and its correlation with kinetics of radical liquid–phase reactions. *International Journal of Chemical Kinetics*, 1(4):361–370, 1969.

[10] Robert Brown. A brief account of microscopical observations made in the months of june, july and august 1827, on the particles contained in the pollen of plants; and on the general existence of active molecules in organic and inorganic bodies. *Philosophical Magazine Series 2*, 4(21):161–173, 1828.

[11] Albert Einstein. On the motion of small particles suspended in liquids at rest required by the molecular-kinetic theory of heat. *Annals of Physics*, 17:549–560, 1905.

[12] Marian von Smoluchowski. On the average path of the gas molecules and its relationship with the theory of diffusion. *Bulletin international de*, pages 202–213, 1906.

[13] Thomas Graham. A short account of experimental researches on the diffusion of gases through each other, and their separation by mechanical means. *Quarterly Journal of Science, Literature and Art*, 27:74–83, 1829.

[14] Thomas Graham. On the law of the diffusion of gases. *Philosophical Magazine Series 3*, 2(9), 1833.

[15] Adolf Fick. On liquid diffusion. *Phil. Mag*, 1855.

[16] Marian von Smoluchowski. Zur kinetischen theorie der brownschen molekularbewegung und der suspensionen. *Annalen der Physik*, 326(14):756–780, 1906.

[17] William Sutherland. A dynamical theory of diffusion for non-electrolytes and the molecular mass of albumin. *Philosophical Magazine Series 6*, 9(54):781–785, 1905.

[18] Ken Dill and Sarina Bromberg. *Molecular Driving Forces: Statistical Thermodynamics in Chemistry and Biology*. Garland Science, 2003.

[19] John T Edward. Molecular volumes and the stokes-einstein equation. *J. chem. Educ*, 47(4):261, 1970.

[20] Theo Odijk. Depletion theory of protein transport in semi-dilute polymer solutions. *Biophysical journal*, 79(5):2314–2321, 2000.

[21] Joseph R. Lakowicz. *Principles of fluorescence spectroscopy*. Springer, New York, 2006.

[22] Aleksander Jabłoński. Über den mechanismus der photolumineszenz von farbstoffphosphoren. *Zeitschrift für Physik*, 94(1-2):38–46, 1935.

[23] Bernard Valeur and Mário Nuno Berberan-Santos. *Molecular fluorescence: principles and applications*. John Wiley & Sons, 2012.

[24] Mikhail Y Berezin and Samuel Achilefu. Fluorescence lifetime measurements and biological imaging. *Chemical reviews*, 110(5):2641–2684, 2010.

[25] Elliot L Elson and Douglas Magde. Fluorescence correlation spectroscopy. i. conceptual basis and theory. *Biopolymers*, 13(1):1–27, 1974.

[26] Douglas Magde, Elliot L Elson, and Watt W Webb. Fluorescence correlation spectroscopy. ii. an experimental realization. *Biopolymers*, 13(1):29–61, 1974.

[27] Douglas Magde, Elliot Elson, and Watt W Webb. Thermodynamic fluctuations in a reacting system-measurement by fluorescence correlation spectroscopy. *Physical Review Letters*, 29(11):705, 1972.

[28] R Rigler, Ülo Mets, J Widengren, and P Kask. Fluorescence correlation spectroscopy with high count rate and low background: analysis of translational diffusion. *European Biophysics Journal*, 22(3):169–175, 1993.

[29] Manfred Eigen and Rudolf Rigler. Sorting single molecules: application to diagnostics and evolutionary biotechnology. *Proceedings of the National Academy of Sciences*, 91(13):5740–5747, 1994.

[30] Hong Qian and Elliot L Elson. Analysis of confocal laser-microscope optics for 3-d fluorescence correlation spectroscopy. *Applied optics*, 30(10):1185–1195, 1991.

[31] Xuzhu Zhang, Andrzej Poniewierski, Aldona Jelinska, Anna Zagozdzon, Agnieszka Wisniewska, Sen Hou, and Robert Holyst. Determination of equilibrium and rate constants for complex formation by fluorescence correlation spectroscopy supplemented by dynamic light scattering and taylor dispersion analysis. *Soft Matter*, 12:8186–8194, 2016.

[32] Petra Schwille. Fluorescence correlation spectroscopy and its potential for intracellular applications. *Cell biochemistry and biophysics*, 34(3):383–408, 2001.

[33] Volker Westphal and Stefan W Hell. Nanoscale resolution in the focal plane of an optical microscope. *Physical review letters*, 94(14):143903, 2005.

[34] Stefan W Hell and Jan Wichmann. Breaking the diffraction resolution limit by stimulated emission: stimulated-emission-depletion fluorescence microscopy. *Optics letters*, 19(11):780–782, 1994.

[35] Thomas A Klar and Stefan W Hell. Subdiffraction resolution in far-field fluorescence microscopy. *Optics letters*, 24(14):954–956, 1999.

[36] Lars Kastrup, Hans Blom, Christian Eggeling, and Stefan W Hell. Fluorescence fluctuation spectroscopy in subdiffraction focal volumes. *Physical review letters*, 94(17):178104, 2005.

[37] Christian Eggeling, Christian Ringemann, Rebecca Medda, Günter Schwarzmann, Konrad Sandhoff, Svetlana Polyakova, Vladimir N Belov, Birka Hein, Claas von Middendorff, Andreas Schönle, and Stefan W Hell. Direct observation of the nanoscale dynamics of membrane lipids in a living cell. *Nature*, 457(7233):1159–1162, 2009.

[38] Veronika Mueller, Alf Honigmann, Christian Ringemann, Rebecca Medda, Günter Schwarzmann, and Christian Eggeling. Fcs in sted microscopy: studying the nanoscale of lipid membrane dynamics. *SY Tetin Fluorescence Fluctuation Spectroscopy*, 519:1–38, 2012.

[39] Giuseppe Vicidomini, Haisen Ta, Alf Honigmann, Veronika Mueller, Mathias P Clausen, Dominic Waithe, Silvia Galiani, Erdinc Sezgin, Alberto Diaspro, Stefan W Hell, and Christian Eggeling. Sted-flcs: an advanced tool to reveal spatiotemporal heterogeneity of molecular membrane dynamics. *Nano letters*, 15(9):5912, 2015.

[40] Christian Ringemann, Ben Harke, Claas Von Middendorff, Rebecca Medda, Alf Honigmann, Richard Wagner, Marcel Leutenegger, Andreas Schönle, Stefan W Hell, and Christian Eggeling. Exploring single-molecule dynamics with fluorescence nanoscopy. *New Journal of Physics*, 11(10):103054, 2009.

[41] Ariel Michelman-Ribeiro, Davide Mazza, Tilman Rosales, Timothy J Stasevich, Hacene Boukari, Vikas Rishi, Charles Vinson, Jay R Knutson, and James G McNally. Direct measurement of association and dissociation rates of dna binding in live cells by fluorescence correlation spectroscopy. *Biophysical journal*, 97(1):337–346, 2009.

[42] Luca Lanzanò, Lorenzo Scipioni, Melody Di Bona, Paolo Bianchini, Ranieri Bizzarri, Francesco Cardarelli, Alberto Diaspro, and Giuseppe Vicidomini. Measurement of nanoscale three-dimensional diffusion in the interior of living cells by sted-fcs. *Nature Communications*, 8:26417–26429.

[43] Krzysztof Sozanski, Evangelos Sisamakis, Xuzhu Zhang, and Robert Holyst. Quantitative fluorescence correlation spectroscopy in 3d systems under stimulated emission depletion conditions. *Optica*, 4(8):982–988, 2017.

[44] John T King, Changqian Yu, William L Wilson, and Steve Granick. Super-resolution study of polymer mobility fluctuations near c^*. *ACS nano*, 8(9):8802–8809, 2014.

[45] Tharwat Tadros. *Encyclopedia of Colloid and Interface Science.* Springer, 2013.

[46] Bruce J Berne and Robert Pecora. *Dynamic light scattering: with applications to chemistry, biology, and physics.* Courier Corporation, 2000.

[47] Wolfgang Schärtl. *Light scattering from polymer solutions and nanoparticle dispersions.* Springer Science & Business Media, 2007.

[48] Paul Heitjans and Jörg Kärger. *Diffusion in condensed matter: methods, materials, models.* Springer Science & Business Media, 2006.

[49] Geoffrey Taylor. Dispersion of soluble matter in solvent flowing slowly through a tube. In *Proceedings of the Royal Society of London A: Mathematical, Physical and Engineering Sciences*, volume 219, pages 186–203. The Royal Society, 1953.

[50] Anna Lewandrowska, Aldona Majcher, Anna Ochab-Marcinek, Marcin Tabaka, and Robert Hołyst. Taylor dispersion analysis in coiled capillaries at high flow rates. *Analytical chemistry*, 85(8):4051–4056, 2013.

[51] A Alizadeh, CA Nieto De Castro, and WA Wakeham. The theory of the taylor dispersion technique for liquid diffusivity measurements. *International Journal of thermophysics*, 1(3):243–284, 1980.

[52] Aldona Majcher, Anna Lewandrowska, Franciszek Herold, Jacek Stefanowicz, Tomasz Słowiński, Aleksander P Mazurek, Stefan A Wieczorek, and Robert Hołyst. A method for rapid screening of interactions of pharmacologically active compounds with albumin. *Analytica chimica acta*, 855:51–59, 2015.

[53] Anna Bielejewska, Andrzej Bylina, Kazimiera Duszczyk, Marcin Fiałkowski, and Robert Hołyst. Evaluation of ligand-selector interaction from effective diffusion coefficient. *Analytical chemistry*, 82(13):5463–5469, 2010.

[54] Haw Yang, Guobin Luo, Pallop Karnchanaphanurach, Tai-Man Louie, Ivan Rech, Sergio Cova, Luying Xun, and X Sunney Xie. Protein conformational dynamics probed by single-molecule electron transfer. *Science*, 302(5643):262–266, 2003.

[55] Gerd Olofsson. Microtitration calorimetric study of the micellization of three poly (oxyethylene) glycol dodecyl ethers. *The Journal of Physical Chemistry*, 89(8):1473–1477, 1985.

[56] Fernando Doñate, Antonio Artigues, ANA Iriarte, and Marino Martinez-Carrion. Opposite behavior of two isozymes when refolding in the presence of non-ionic detergents. *Protein science*, 7(8):1811–1820, 1998.

[57] Jedrzej Szymański, Adam Patkowski, Agnieszka Wilk, Piotr Garstecki, and Robert Holyst. Diffusion and viscosity in a crowded environment: from nano-to macroscale. *The Journal of Physical Chemistry B*, 110(51):25593–25597, 2006.

[58] E Dutkiewicz and A Jakubowska. Effect of electrolytes on the physicochemical behaviour of sodium dodecyl sulphate micelles. *Colloid & Polymer Science*, 280(11):1009–1014, 2002.

[59] J Turro Nicholas, Xue-Gong Lei, KP Ananthapadmanabhan, and M Aronson. Spectroscopic probe analysis of protein–surfactant interactions: the bsa/sds system. *Langmuir*, 11(2):525–2, 1995.

[60] Ank Valstar, Mats Almgren, Wyn Brown, and Marilena Vasilescu. The interaction of bovine serum albumin with surfactants studied by light scattering. *Langmuir*, 16(3):922–927, 2000.

[61] Laura T Okano, Frank H Quina, and Omar A El Seoud. Fluorescence and light-scattering studies of the aggregation of cationic surfactants in aqueous solution: effects of headgroup structure. *Langmuir*, 16(7):3119–3123, 2000.

[62] Marie Wahlgren, Jenny Kedström, and Thomas Arnebrant. The interactions in solution between nonionic surfactants and globular proteins: Effects on cloud point. *Journal of dispersion science and technology*, 18(4):449–458, 1997.

[63] Narendra B Bam, Jeffrey L Cleland, and Theodore W Randolph. Molten globule intermediate of recombinant human growth hormone: stabilization with surfactants. *Biotechnology progress*, 12(6):801–809, 1996.

[64] Gebrenegus Yohannes, Susanne K Wiedmer, Matti Elomaa, Matti Jussila, Vladimir Aseyev, and Marja-Liisa Riekkola. Thermal aggregation of bovine serum albumin studied by asymmetrical flow field-flow fractionation. *Analytica chimica acta*, 675(2):191–198, 2010.

[65] YE Chen and Ammasi Periasamy. Characterization of two-photon excitation fluorescence lifetime imaging microscopy for protein localization. *Microscopy research and technique*, 63(1):72–80, 2004.

[66] Ashok Pabbathi, Satyajit Patra, and Anunay Samanta. Structural transformation of bovine serum albumin induced by dimethyl sulfoxide and probed by fluorescence correlation spectroscopy and additional methods. *ChemPhysChem*, 14(11):2441–2449, 2013.

[67] Daniel Otzen. Protein–surfactant interactions: a tale of many states. *Biochimica et Biophysica Acta (BBA)-Proteins and Proteomics*, 1814(5):562–591, 2011.

[68] Peter Kapusta, Radek Macháň, Aleš Benda, and Martin Hof. Fluorescence lifetime correlation spectroscopy (flcs): concepts, applications and outlook. *International journal of molecular sciences*, 13(10):12890–12910, 2012.

[69] Vladimir N Uversky, Stefan Winter, and Günter Löber. Use of fluorescence decay times of 8-ans-protein complexes to study the conformational transitions in proteins which unfold through the molten globule state. *Biophysical chemistry*, 60(3):79–88, 1996.

[70] P-O Gendron, F Avaltroni, and KJ Wilkinson. Diffusion coefficients of several rhodamine derivatives as determined by pulsed field gradient–nuclear magnetic resonance and fluorescence correlation spectroscopy. *Journal of fluorescence*, 18(6):1093, 2008.

[71] Thomas Dertinger, Anastasia Loman, Benjamin Ewers, Claus B Müller, Benedikt Krämer, and Jörg Enderlein. The optics and performance of dual-focus fluorescence correlation spectroscopy. *Optics express*, 16(19):14353–14368, 2008.

[72] M Zulauf, K Weckstrom, JB Hayter, V Degiorgio, and M Corti. Neutron scattering study of micelle structure in isotropic aqueous solutions of poly (oxyethylene) amphiphiles. *Journal of physical chemistry*, 89(15):3411–3417, 1985.

[73] Mercedes Novo, Suren Felekyan, Claus AM Seidel, and Wajih Al-Soufi. Dye-exchange dynamics in micellar solutions studied by fluorescence correlation spectroscopy. *The Journal of Physical Chemistry B*, 111(14):3614–3624, 2007.

[74] Jorge Bordello, Mercedes Novo, and Wajih Al-Soufi. Exchange-dynamics of a neutral hydrophobic dye in micellar solutions studied by fluorescence correlation spectroscopy. *Journal of colloid and interface science*, 345(2):369–376, 2010.

[75] Heiko Zettl, Yariv Portnoy, Moshe Gottlieb, and Georg Krausch. Investigation of micelle formation by fluorescence correlation spectroscopy. *The Journal of Physical Chemistry B*, 109(27):13397–13401, 2005.

[76] Oleg Krichevsky and Grégoire Bonnet. Fluorescence correlation spectroscopy: the technique and its applications. *Reports on Progress in Physics*, 65(2):251, 2002.

[77] RB Dorshow, CA Bunton, and DF Nicoli. Comparative study of intermicellar interactions using dynamic light scattering. *The Journal of Physical Chemistry*, 87(8):1409–1416, 1983.

[78] Jacek Gapinski, Jedrzej Szymanski, Agnieszka Wilk, Joachim Kohlbrecher, Adam Patkowski, and Robert Hołyst. Size and shape of micelles studied by means of sans, pcs, and fcs. *Langmuir*, 26(12):9304–9314, 2010.

[79] Hong-Un Kim and Kyung-Hee Lim. Sizes and structures of micelles of cationic octadecyl trimethyl ammonium chloride and anionic ammonium dodecyl sulfate surfactants in aqueous solutions. *Bulletin of the Korean Chemical Society*, 25(3):382–388, 2004.

[80] Franziska Luschtinetz and Carsten Dosche. Determination of micelle diffusion coefficients with fluorescence correlation spectroscopy (fcs). *Journal of colloid and interface science*, 338(1):312–315, 2009.

[81] Subhadip Ghosh, Ujjwal Mandal, Aniruddha Adhikari, and Kankan Bhattacharyya. Study of diffusion of organic dyes in a triblock copolymer micelle and gel by fluorescence correlation spectroscopy. *Chemistry–An Asian Journal*, 4(6):948–954, 2009.

[82] Apostolos Vagias, Riccardo Raccis, Kaloian Koynov, Ulrich Jonas, Hans-Jürgen Butt, George Fytas, Peter Košovan, Olaf Lenz, and Christian Holm. Complex tracer diffusion dynamics in polymer solutions. *Physical review letters*, 111(8):088301, 2013.

[83] Vincent C Reinsborough and Josef F Holzwarth. Kinetics of the interactions between dyes and micelles. *Canadian journal of chemistry*, 64(5):955–959, 1986.

[84] A Johná Elliot et al. Estimation of rate constants for near-diffusion-controlled reactions in water at high temperatures. *Journal of the Chemical Society, Faraday Transactions*, 86(9):1539–1547, 1990.

[85] Hans Blom, Andriy Chmyrov, Kai Hassler, Lloyd M Davis, and Jerker Widengren. Triplet-state investigations of fluorescent dyes at dielectric interfaces using total internal reflection fluorescence correlation spectroscopy. *The Journal of Physical Chemistry A*, 113(19):5554–5566, 2009.

[86] Bo Huang, Hazen Babcock, and Xiaowei Zhuang. Breaking the diffraction barrier: super-resolution imaging of cells. *Cell*, 143(7):1047–1058, 2010.

[87] Tobias Müller, Christian Schumann, and Annette Kraegeloh. Sted microscopy and its applications: new insights into cellular processes on the nanoscale. *ChemPhysChem*, 13(8):1986–2000, 2012.

[88] Thomas Niehorster, Anna Loschberger, Ingo Gregor, Benedikt Kramer, Hans-Jurgen Rahn, Matthias Patting, Felix Koberling, Jorg Enderlein, and Markus Sauer. Multi-target spectrally resolved fluorescence lifetime imaging microscopy. *Nat. Methods*, 13:257–262, 2016.

[89] Daniel S Banks, Charmaine Tressler, Robert D Peters, Felix Hofling, and Cecile Fradin. Characterizing anomalous diffusion in crowded polymer solutions and gels over five decades in time with variable-lengthscale fluorescence correlation spectroscopy. *Soft Matter*, 12(18):4190–4203, 2016.

[90] Matthias Reuss, Johann Engelhardt, and Stefan W Hell. Birefringent device converts a standard scanning microscope into a sted microscope that also maps molecular orientation. *Optics express*, 18(2):1049–1058, 2010.

[91] Thomas Schönau, Torsten Siebert, Romano Härtel, Thomas Eckhardt, Dietmar Klemme, Kristian Lauritsen, and Rainer Erdmann. Pulsed picosecond 766 nm laser source operating between 1-80 mhz with automatic pump power management. In *SPIE LASE*, pages 860409–860409. International Society for Optics and Photonics, 2013.

[92] Mathias P Clausen, Erdinc Sezgin, Jorge Bernardino de la Serna, Dominic Waithe, B Christoffer Lagerholm, and Christian Eggeling. A straightforward approach for gated sted-fcs to investigate lipid membrane dynamics. *Methods*, 88:67–75, 2015.

[93] Giuseppe Vicidomini, Gael Moneron, Kyu Y Han, Volker Westphal, Haisen Ta, Matthias Reuss, Johann Engelhardt, Christian Eggeling, and Stefan W Hell. Sharper low-power sted nanoscopy by time gating. *Nature methods*, 8(7):571–573, 2011.

[94] Jeffrey R Moffitt, Christian Osseforth, and Jens Michaelis. Time-gating improves the spatial resolution of sted microscopy. *Optics express*, 19(5):4242–4254, 2011.

[95] P Török and PRT Munro. The use of gauss-laguerre vector beams in sted microscopy. *Optics express*, 12(15):3605–3617, 2004.

[96] Charmaine Tressler, Michael Stolle, and Cécile Fradin. Fluorescence correlation spectroscopy with a doughnut-shaped excitation profile as a characterization tool in sted microscopy. *Optics express*, 22(25):31154–31166, 2014.

[97] Marcel Leutenegger, Christian Eggeling, and Stefan W Hell. Analytical description of sted microscopy performance. *Optics express*, 18(25):26417–26429, 2010.

[98] Benjamin Harke, Jan Keller, Chaitanya K Ullal, Volker Westphal, Andreas Schönle, and Stefan W Hell. Resolution scaling in sted microscopy. *Optics express*, 16(6):4154–4162, 2008.

[99] Xuzhu Zhang, Evangelos Sisamakis, Krzysztof Sozanski, and Robert Holyst. Nanoscopic approach to quantification of equilibrium and rate constants of complex formation at single-molecule level. *Journal of physical chemistry letters*, 8:5785–5791, 2017.

[100] Tomasz Kalwarczyk, Natalia Ziebacz, Anna Bielejewska, Ewa Zaboklicka, Kaloian Koynov, Jedrzej Szymanski, Agnieszka Wilk, Adam Patkowski, Jacek Gapinski, Hans-JuĬĹrgen Butt, and Robert Hołyst. Comparative analysis of viscosity of complex liquids and cytoplasm of mammalian cells at the nanoscale. *Nano letters*, 11(5):2157–2163, 2011.

[101] Albert C Pan, David W Borhani, Ron O Dror, and David E Shaw. Molecular determinants of drug–receptor binding kinetics. *Drug discovery today*, 18(13):667–673, 2013.

[102] Giorgio Minotti, Pierantonio Menna, Emanuela Salvatorelli, Gaetano Cairo, and Luca Gianni. Anthracyclines: molecular advances and pharmacologic developments in antitumor activity and cardiotoxicity. *Pharmacological reviews*, 56(2):185–229, 2004.

[103] Christine A Frederick, Loren Dean Williams, Giovanni Ughetto, Gijs A Van der Marel, Jacques H Van Boom, Alexander Rich, and Andrew HJ Wang. Structural comparison of anticancer drug-dna complexes: adriamycin and daunomycin. *Biochemistry*, 29(10):2538–2549, 1990.

[104] Fan Yang, Sheila S Teves, Christopher J Kemp, and Steven Henikoff. Doxorubicin, dna torsion, and chromatin dynamics. *Biochimica et Biophysica Acta (BBA)-Reviews on Cancer*, 1845(1):84–89, 2014.

[105] Y-J Schneider, R Baurain, A Zenebergh, and A Trouet. Dna-binding parameters of daunorubicin and doxorubicin in the conditions used for studying the interaction of anthracycline-dna complexes with cells in vitro. *Cancer chemotherapy and pharmacology*, 2(1):7–10, 1979.

[106] Cristina Pérez-Arnaiz, Natalia Busto, José M Leal, and Begoña García. New insights into the mechanism of the dna/doxorubicin interaction. *The Journal of Physical Chemistry B*, 118(5):1288–1295, 2014.

[107] Marta Airoldi, Giampaolo Barone, Giuseppe Gennaro, Anna Maria Giuliani, and Mauro Giustini. Correction to interaction of doxorubicin with polynucleotides. a spectroscopic study. *Biochemistry*, 54(50):7423–7423, 2015.

[108] Fujun Yao, Jing Duan, Ying Wang, Yue Zhang, Yanli Guo, Huilin Guo, and Xiaofeng Kang. Nanopore single-molecule analysis of dna–doxorubicin interactions. *Analytical chemistry*, 87(1):338–342, 2014.

[109] Reza Hajian, Nafiseh Shams, and Majid Mohagheghian. Study on the interaction between doxorubicin and deoxyribonucleic acid with the use of methylene blue as a probe. *Journal of the Brazilian Chemical Society*, 20(8):1399–1405, 2009.

[110] Vincenzo Rizzo, Nereo Sacchi, and Milena Menozzi. Kinetic studies of anthracycline-dna interaction by fluorescence stopped flow confirm a complex association mechanism. *Biochemistry*, 28(1):274–282, 1989.

[111] Daniel Agudelo, Philippe Bourassa, Gervais Bérubé, and Heidar-Ali Tajmir-Riahi. Intercalation of antitumor drug doxorubicin and its analogue by dna duplex: structural features and biological implications. *International journal of biological macromolecules*, 66:144–150, 2014.

[112] KB Roy, T Antony, A Saxena, and HB Bohidar. Ethanol-induced condensation of calf thymus dna studied by laser light scattering. *The Journal of Physical Chemistry B*, 103(24):5117–5121, 1999.

[113] Dominic Störkle, Sabrina Duschner, Nils Heimann, Michael Maskos, and Manfred Schmidt. Complex formation of dna with oppositely charged polyelectrolytes of different chain topology: cylindrical brushes and dendrimers. *Macromolecules*, 40(22):7998–8006, 2007.

[114] Long B Liao, Hai Y Zhou, and Xian M Xiao. Spectroscopic and viscosity study of doxorubicin interaction with dna. *Journal of molecular structure*, 749(1):108–113, 2005.

[115] Hongxing Lei, Xiaofeng Wang, and Chun Wu. Early stage intercalation of doxorubicin to dna fragments observed in molecular dynamics binding simulations. *Journal of Molecular Graphics and Modelling*, 38:279–289, 2012.

[116] Arnab Mukherjee, Richard Lavery, Biman Bagchi, and James T Hynes. On the molecular mechanism of drug intercalation into dna: a simulation study of the intercalation pathway, free energy, and dna structural changes. *Journal of the American Chemical Society*, 130(30):9747–9755, 2008.

[117] Jie-Hua Shi, Jun Chen, Jing Wang, and Ying-Yao Zhu. Binding interaction between sorafenib and calf thymus dna: Spectroscopic methodology, viscosity measurement and molecular docking. *Spectrochimica Acta Part A: Molecular and Biomolecular Spectroscopy*, 136:443–450, 2015.

[118] Shuyun Bi, Tingting Zhao, Yu Wang, Huifeng Zhou, Bo Pang, and Tingting Gu. Binding studies of terbutaline sulfate to calf thymus dna using multispectroscopic and molecular docking techniques. *Spectrochimica Acta Part A: Molecular and Biomolecular Spectroscopy*, 150:921–927, 2015.

[119] Maria Ospina, Alina Costin, Adrienne K Barry, and Hubert W Vesper. Characterization of n-terminal formaldehyde adducts to hemoglobin. *Rapid Communications in Mass Spectrometry*, 25(8):1043–1050, 2011.

[120] Kun Lu, Wenjie Ye, Li Zhou, Leonard B Collins, Xian Chen, Avram Gold, Louise M Ball, and James A Swenberg. Structural characterization of formaldehyde-induced cross-links between amino acids and deoxynucleosides and their oligomers. *Journal of the American Chemical Society*, 132(10):3388–3399, 2010.

[121] Dylan J Taatjes, Giorgio Gaudiano, Katheryn Resing, and Tad H Koch. Alkylation of dna by the anthracycline, antitumor drugs adriamycin and daunomycin. *Journal of medicinal chemistry*, 39(21):4135–4138, 1996.

[122] Dylan J Taatjes, Giorgio Gaudiano, Katheryn Resing, and Tad H Koch. Redox pathway leading to the alkylation of dna by the anthracycline, antitumor drugs adriamycin and daunomycin. *Journal of medicinal chemistry*, 40(8):1276–1286, 1997.

[123] Steven M Zeman, Don R Phillips, and Donald M Crothers. Characterization of covalent adriamycin-dna adducts. *Proceedings of the National Academy of Sciences*, 95(20):11561–11565, 1998.

[124] Ryan A Luce, Snorri Th Sigurdsson, and Paul B Hopkins. Quantification of formaldehyde-mediated covalent adducts of adriamycin with dna. *Biochemistry*, 38(27):8682–8690, 1999.

[125] Fenfei Leng, Rajesh Savkur, Izabela Fokt, Teresa Przewloka, Waldemar Priebe, and Jonathan B Chaires. Base specific and regioselective chemical cross-linking of daunorubicin to dna. *Journal of the American Chemical Society*, 118(20):4731–4738, 1996.

[126] Shuji Kato, Patrick J Burke, David J Fenick, Dylan J Taatjes, Veronica M Bierbaum, and Tad H Koch. Mass spectrometric measurement of formaldehyde generated in breast cancer cells upon treatment with anthracycline antitumor drugs. *Chemical research in toxicology*, 13(6):509–516, 2000.

[127] Shuji Kato, Patrick J Burke, Tad H Koch, and Veronica M Bierbaum. Formaldehyde in human cancer cells: detection by preconcentration-chemical ionization mass spectrometry. *Analytical chemistry*, 73(13):2992–2997, 2001.

[128] Suzanne M Cutts, Abraham Nudelman, Ada Rephaeli, and Don R Phillips. The power and potential of doxorubicin-dna adducts. *IUBMB life*, 57(2):73–81, 2005.

[129] Pascale Changenet-Barret, Thomas Gustavsson, Dimitra Markovitsi, Ilse Manet, and Sandra Monti. Unravelling molecular mechanisms in the fluorescence spectra of doxorubicin in aqueous solution by femtosecond fluorescence spectroscopy. *Physical Chemistry Chemical Physics*, 15(8):2937–2944, 2013.

[130] Huifang Huang and Paul B Hopkins. Dna interstrand cross-linking by formaldehyde: nucleotide sequence preference and covalent structure of the predominant cross-link formed in synthetic oligonucleotides. *Journal of the American Chemical Society*, 115(21):9402–9408, 1993.

[131] Elizabeth A Hoffman, Brian L Frey, Lloyd M Smith, and David T Auble. Formaldehyde crosslinking: a tool for the study of chromatin complexes. *Journal of Biological Chemistry*, 290(44):26404–26411, 2015.

[132] Belinda S Parker, Carleen Cullinane, and Don R Phillips. Formation of dna adducts by formaldehyde-activated mitoxantrone. *Nucleic acids research*, 27(14):2918–2923, 1999.

[133] Richard N Day and Fred Schaufele. Imaging molecular interactions in living cells. *Molecular endocrinology*, 19(7):1675–1686, 2005.

[134] Christopher C Govern, Michelle K Paczosa, Arup K Chakraborty, and Eric S Huseby. Fast on-rates allow short dwell time ligands to activate t cells. *Proceedings of the National Academy of Sciences*, 107(19):8724–8729, 2010.